

Syracuse University

SURFACE at Syracuse University

Dissertations - ALL

SURFACE at Syracuse University

5-14-2023

AlGaAs Coating Studies for Present and Future Gravitational Wave Detectors

Nicholas Anthony Didio
Syracuse University

Follow this and additional works at: <https://surface.syr.edu/etd>

Recommended Citation

Didio, Nicholas Anthony, "AlGaAs Coating Studies for Present and Future Gravitational Wave Detectors" (2023). *Dissertations - ALL*. 1710.
<https://surface.syr.edu/etd/1710>

This Dissertation is brought to you for free and open access by the SURFACE at Syracuse University at SURFACE at Syracuse University. It has been accepted for inclusion in Dissertations - ALL by an authorized administrator of SURFACE at Syracuse University. For more information, please contact surface@syr.edu.

ABSTRACT

With the first observation of a binary black hole merger in GW150914 [1], LIGO heralded a new era in the field of observational astronomy. It was the first observation of any astronomical object by measuring its gravitational wave signature, opening a new window to the cosmos. A few years later, the first astronomical event to be observed by both electromagnetic waves and gravitational waves was made [2, 3]. Gravitational wave detectors are multi-kilometer long interferometers measure changes to their length imparted by passing gravitational waves that are smaller than an atomic nucleus. Such extreme precision requires extensive mitigation of many different noise sources, discussed in chapter 1. This work is primarily focused on thermal noise of the gravitational wave detector test mass coatings, detailed in chapter 2. Chapter 3 outlines the theory behind the cryogenic gentle nodal suspension [4], the experiment the author constructed at Syracuse to measure coating thermal noise of possible test mass coatings. Chapters 4 and 5 will delve into the data that the author measured in the cryogenic gentle nodal suspension. There is a special focus in this work on AlGaAs/GaAs multi-layers, referred to as just AlGaAs for simplicity, as a possible test mass coating. This crystalline coating has shown remarkably low levels of loss at room temperature [5, 6]. This work serves as a follow-up to the room temperature loss measurements, with the goals of understanding the loss mechanisms inside an AlGaAs coating through the shape of its loss curve over temperature [7] and applying the findings to possible cold temperature gravitational wave detectors [8–10]. The mechanical loss of the AlGaAs coating was found to be largely varied by mode, with the lowest mode displaying loss levels of $\phi_{\text{coating}} \lesssim 1 \times 10^{-6}$ and the highest mode showing loss of $\phi_{\text{coating}} \lesssim 1 \times 10^{-4}$. Investigations into the mechanisms contributing to excess loss in some of the modes are currently underway. The lowest loss modes are consistent with room temperature measurements.

ALGAAS COATING STUDIES FOR PRESENT AND FUTURE GRAVITATIONAL WAVE DETECTORS

By

Nicholas Didio

B.S. Colgate University, 2016

M.S. Syracuse University, 2020

DISSERTATION

SUBMITTED IN PARTIAL FULFILLMENT OF THE REQUIREMENTS

FOR THE DEGREE OF

DOCTOR OF PHILOSOPHY IN PHYSICS

Syracuse University

May 2023

Copyright © Nicholas Didio May 2023
All rights reserved.

ACKNOWLEDGEMENTS

I must first deeply thank my advisor, Stefan Ballmer, for his unwavering patience and confidence in my abilities as an experimentalist, even when I did not believe them myself. I am very lucky to have had the opportunity to work alongside such a remarkable physicist as a graduate researcher.

I am also forever indebted to Steve Penn. A deep thank you for guiding me through the field of coatings research. When we first met, I knew almost nothing about the field, and without your help I would never have published this thesis.

Satoshi, you are the postdoc that every graduate student dreams of having in their group. Not only have you patiently assisted me with nearly every problem I faced, you have also been someone to share my triumphs and frustrations with. I wish you the best in the coming years, at Syracuse and beyond.

It has been exciting to watch the Physics Department at Syracuse grow over the years, and this was mostly driven by the relentless determination of Jenny Ross. I must thank her for always striving to make the department a place where all are welcome and can achieve their best.

Whenever I was at my lowest, a conversation with Walter Freeman would always remind me of what I am capable of and that any obstacle could be conquered. My entire knowledge base of both teaching and coding came from you, and I could not have asked for a better mentor or friend. I genuinely wish I could TA computational physics with you again.

To the various physics faculty who have influenced me in small ways and big, I will always cherish the opportunity I had to learn from you. This includes but is not limited to Peter Saulson, Duncan Brown, Eric Coughlin, Denver Whittington, Mitch Soderberg, Simon Catterall, and Scott Watson (that cosmology independent study was not at all relevant to my research, but it was a lot of fun).

The Syracuse Physics Machine Shop professionals were always an incredible resource in construction of my experiment. Special thanks to Phil Arnold, who was simultaneously a machinist, a comedian, an engineer, a problem-solver, and a friend.

My colleagues in the LVK Collaboration were an invaluable resource, and I can even call some my friends. First and foremost, I must acknowledge the copious amount of research assistance received from Simon Tait. The collaboration will flourish with physicists like Simon in its ranks. Another special thank you to Ruinan Zhou, for helpful conversations about her thermoelastic loss model. Without her help, this thesis may not have been published until 2024.

To my friends outside the Syracuse community, thank you for often keeping me grounded in the “real” world (or not). To Tom, Denise, Flex, Luna, and Lindsay especially, you are all so special to me and I cannot imagine a life without you in it.

My graduate student peers at Syracuse were truly the rock upon which I most often leaned. Without you all, I would not be the physicist or person I am today.

To TVo, Fabian, Danny, Erik, Ari, Varun, Subham, Elenna, and Matt, you were all a joy to work with in Stefan’s group. I hope I gave back just a tenth of what you have all given me, as a physicist and as a friend.

I will always fondly remember solving problem sets with Rum and Quanta to pet when I got frustrated. Ohana, thank you for bringing me energy and life.

Maxx, I look fondly on the nights we spent eating too many wings while watching TV during the pandemic. Also, thank you for being the only physicist who owns a large cooler.

To Varun, you were both a friend and a model physicist to emulate. I look forward to your wedding and a friendship that lasts long after it.

To Kenny, you are a great friend in more ways than one, and I will always love listening to you ramble about obscure math.

My FIFA skills would be much worse were it not for Pinaki. I miss you, but am content knowing you and Kelly are happy together in Orlando.

Speaking of FIFA skills, I would be remiss to leave out Chaitanya. Skiing, hiking, FIFA, frisbee, we’ve done it all together. I hope we get to do more in the future.

To Vito, whether it was helping me fix up my experiment or my kitchen at 2 am, I was always very grateful to have you around. Thank you.

Whether it was Dungeons and Dragons, a party, or trivia night, it wasn't the same without Joe there. You were the impetus behind the trivia tradition, and a great friend for many reasons beside.

To Tianna and Louis, I don't know what your plans are for after graduation, but if you find yourselves in NYC you will always have a friend to go out with (to a bar or a wing eating challenge) that is just one text message away.

There's no one I'd rather have come over on a random Tuesday night than Julia. I have cherished our friendship, and always miss our nights rock climbing or playing Celeste together. Thank you for allowing Liz and I to "adopt" you in your first year.

Sarthak, I will never forget the evenings we spent cooking together during the pandemic. No one asks questions that cut directly to the heart of whatever is being discussed like you do; our conversations are always stimulating.

To Erin, Vinny, Josh, Brooke, Joe, Liz, Ben, Ben, and Grace, you all have been the most beautiful and fun bunch of nerds anyone could want to spend time with. There will always be a place for you in my life.

To my longtime roommate and friend, what can I say that I haven't already? Liz, I still remember the day we met at orientation, and how nervous I was that you would hate living with me when we moved in together less than a year later. My nerves could not have been more misplaced. No longer living with you has been one of the few negative aspects of graduating. When are we going halvesies on that mansion?

To my family, Mom, Dad, Cami, Tommy, Lauren, Olivia, Luca, Craig, Kim, and Chelsea, thank you for your resilient support throughout this entire long, long process. We missed so much together so that I could achieve this degree. That sacrifice is not lost on me, and I hope to make up every second that I missed. Especially when it comes to my niece and nephew, Olivia and Luca.

Last but not least, no one sacrificed more than my friend, my confidant, and my partner, Jaime. You did not blink when I said I was going to Syracuse for my degree nor did you ever complain throughout the five years we were apart. When I faltered, you picked me up. When I was triumphant, you shared my joy. All from 250 miles away. For all of this, I will forever love you more than can be put into words.

Contents

List of Tables	ix
List of Figures	xviii
Preface	xix
1 Introduction	1
1.1 Gravitational Waves	1
1.2 Birth and Evolution of Gravitational Wave Detectors	3
1.2.1 The First Attempts at Detecting Gravitational Waves	4
1.2.2 The Michelson-Morley Interferometer	4
1.2.3 Sidebands	11
1.2.4 The Fabry-Pérot Cavity	16
1.3 Noise Sources in Gravitational Wave Interferometers	18
1.3.1 Seismic, Newtonian, and Residual Gas Noise	19
1.3.2 Quantum Phenomena: Shot Noise and Radiation Pressure Noise	21
2 Coating Thermal Noise and the Test Masses	23
2.1 The Theory of Coating Thermal Noise	24
2.1.1 Fluctuation-Dissipation Theorem and Coating Thermal Noise	24
2.1.2 Loss Angle of a Test Mass Coating	30
2.1.3 Thermoelastic Dissipation	42
2.1.4 Thermo-Refractive Noise	60
2.1.5 Thermo-Optic Noise	61
2.2 Coating the Test Masses	62
2.2.1 Optical Demands on the Test Masses	62

2.2.2	Strain Sensitivities of Present Detectors and Coating Noise . .	63
2.2.3	Strain Sensitivities Required of Third Generation Detectors . .	68
2.2.4	Improving the Coatings	72
3	Multi-Modal Gentle Nodal Suspension	75
3.1	Measuring Thermal Noise	76
3.1.1	Vibrational Mode Ringdowns and Coating Thermal Noise . .	77
3.2	Gentle Nodal Suspension	79
3.3	Extracting Coating Mechanical Loss From Substrate-Coating System Loss	83
3.3.1	The Dilution Factor	83
3.4	Building the Cryogenic Gentle Nodal Suspension	84
3.4.1	Before Cryostat Delivery	85
3.4.2	Achieving Room Temperature Operation of the Cryo-GeNS . .	95
3.4.3	Achieving Cold Temperature Operation of the Cryo-GeNS . .	97
4	Cryogenic Multi-Modal GeNS: Data Replication	100
4.1	Room Temperature Replication: Fused Silica	101
4.2	Replication of Cold Temperature Data: Fused Silica and Silicon . . .	102
5	Cryogenic Multi-Modal GeNS: AlGaAs	106
5.1	GaAs-AlGaAs Multilayer Coating: A Brief History	107
5.2	AlGaAs Cold Temperature Mechanical Loss: Results	109
5.3	AlGaAs Cold Temperature Mechanical Loss: Thermal Noise in Gravi- tational Wave Detectors	116
5.3.1	Search for Bulk and Shear Loss Angles	116
5.3.2	AlGaAs and Gravitational Wave Detectors	119
6	Conclusion	122

List of Tables

1	A table detailing all the constants for crystalline silicon at a given temperature for the TE loss analysis. The value of Bulk Modulus K was held fixed at 100 GPa. See Liu [11] for the justification of fixing K .	45
2	A table detailing all the constants used for the AlGaAs-GaAs multi-layer coating at a given temperature for the TE loss analysis. The value of Young's Modulus E and Poisson ratio σ were held fixed at 83.6 GPa and 0.40 respectively [12]. For the heat capacity, additional data at 30 K and 40 K were included to increase the accuracy of the interpolation. The same was done at 150 K, 175 K, and 250 K for the thermal conductivity.	57
3	A table mapping the mode numbers onto frequencies and mode shapes, where the mode shapes are described as (m, n) . The mode shape number m denotes the amount of radial nodes or circles, while the number n denotes the amount of angular nodes or lines. The associated dilution factors, determined from FEA in COMSOL [13] are also listed. Note that mode number is just an easy way to keep track of which mode is being referenced, instead of stating a shape or frequency. The mode number is chosen by simply numbering all non-degenerate modes by increasing frequency.	115

List of Figures

1	A visual depiction of how a gravitational wave travelling through the plane of this thesis would alter the distances between point masses arranged in a circle. The two sets of figures labelled h_{\times} and h_{+} represent the two polarization states of a gravitational wave.	3
2	The most basic version of a Michelson Interferometer. As the light travels through the x or y arms, it accumulates phase. The difference in phase between x and y cause them to recombine constructively or destructively, changing the power observed at the photodiode. BS is short for beamsplitter, PD is short for photodiode, L_x and L_y are the lengths of the x and y arms respectively. Henceforth, the photodiode that measures the recombined light power will be referred to as the anti-symmetric port.	6
3	Accumulated phase shift in an ideal 4 km and 100 km interferometer assuming a gravitational wave strain $h_0 = 10^{-23}$ and laser wavelength $\lambda = 1064$ nm.	9
4	The two LIGO detectors at Hanford, Washington [14] and Livingston, Louisiana [15], respectively. The arms extending off the main building 90° from each other are the 4 km beam tubes of the interferometer. Light travels down each path and recombines, sometimes with their relative phase altered by a passing gravitational wave, in the main building.	10

5	A map showing the locations of all gravitational wave observatories, operational and planned. The current global gravitational wave detector network consists of the twin LIGO detectors in the United States, GEO600 and VIRGO observatories in Europe, and the KAGRA observatory in Japan. There is another planned detector to be built in India. This map does not include next generation detectors projected to be built in the 2030s and 2040s.	11
6	A Michelson Inteferometer with a heterodyne detection scheme. . . .	14
7	Pictured is an example of a Herriott Delay line (top) and a Fabry-Pérot cavity (bottom). All gravitational wave interferometers, in operation or in development, use the Fabry-Pérot cavity to build power in the arms. See equations 1.41, 1.42, and 1.43 for a quantitative description of the three noted electric fields.	16
8	A graph depicting the sensitivity of the LIGO Hanford Observatory in the most recent observing run, O3. The x-axis has units of frequency, while the y-axis is units of $m/\sqrt{\text{Hz}}$. Therefore, any gravitational wave that causes a length change at a given frequency that is smaller than the corresponding measured noise, the solid blue line, will be drowned in the noise and unable to be detected. Conversely, any stronger gravitational wave that falls above the blue line can be detected. Graphs such as these are often referred to as noise budgets [16]. The DARM of the y-axis stands for Differential ARM length. Often the y-axis will have units of $1/\sqrt{\text{Hz}}$ instead of $m/\sqrt{\text{Hz}}$. To convert from $m/\sqrt{\text{Hz}}$ to $1/\sqrt{\text{Hz}}$, one must simply divide by the arm length. For the LIGO Hanford observatory, that would be 4,000 meters.	18
9	Depicted above is a drawing of a multilayer coated test mass. The various fluctuations that contribute to coating noise are also pictured: $\delta z_s(\vec{x})$, $\delta l_j(\vec{x})$, $\delta A_j/A_j$ and $\delta n_j(\mathbf{x})$. Image credit to Hong [17].	33

10	A model of TE Dissipation in a bent beam. Darker areas are hotter, while lighter areas are colder. Notice how the locations where the material is being compressed heat up, while the opposite is true where the material is being stretched. In the center, this causes a local heat flow from the bottom of the bar to the top, shown by the arrow in the cut-out. Credit for this image to Candler [18].	43
11	Theoretical thermoelastic loss of 4 inch diameter bare silicon disk normal modes with disk thickness of 500 μm at various temperatures from 12 K to 300 K, plotted with the measured loss for those modes. Refer to Figure 12 to see the data at each mode individually. The data marked with an \times are modeled, while the solid circles were measured in the Cryogenic Gentle Nodal Suspension, see chapters 3 and 4. Any measured data without error bars is due to the error bars being too small to see. The measured loss is dominated by TED at 100 K, 200 K, and 300 K. The importance of the coefficient of thermal expansion is demonstrated by the large drop in TE loss at 122 K, where it is near a zero crossing point of the coefficient. Even though the temperature is higher, the measured loss at 122 K is equal to or lower than the measured loss at 50 K for all modes. The dip between the two modes just above 6 kHz is due to the fact that these modes are from different mode families, which alters the value of the geometric factor \mathcal{D} . Since the measured loss is a combination of all loss sources, the measured data (circles) sit above the TED model (\times) or agree with it. The important lesson to be learned from this graph is that the substrate loss is totally dominated by TED above 50 K except at 122 K. The continuous curves of Figure 12 allows even better understanding of when TED is responsible for the measured substrate loss. See Cagnoli [19] and equation 2.121 for more details about the model.	46

12	Modeled substrate loss due to thermoelastic dissipation (green curves) compared to measured substrate loss (purple points) for the first six modes. The green curves were calculated using equation 2.121. The purple points were measured in the Cryogenic Gentle Nodal Suspension by the author, see chapters 3 and 4 for details on the experiment and crystalline silicon substrate measurement process.	47
12	Modeled substrate loss due to thermoelastic dissipation (green curves) compared to measured substrate loss (purple points) for the last two modes. The green curves were calculated using equation 2.121. The purple points were measured in the Cryogenic Gentle Nodal Suspension by the author, see chapters 3 and 4 for details on the experiment and crystalline silicon substrate measurement process.	48
13	This plot shows the surface of TED. This view emphasizes the large variance experienced at a single frequency when temperature is varied. Note the z-axis is plotting $\log(\phi_{TE})$ due to limitations of the plotting software.	50
14	This plot shows the surface of TED. This view emphasizes the small variance experienced at a single temperature when frequency is varied. Note the z-axis is plotting $\log(\phi_{TE})$ due to limitations of the plotting software.	51
15	Modeled thermoelastic loss from 12 K to 300 K for the first four modes. Overlaid in red is experimentally determined data for the total loss of the AlGaAs-coated silicon resonators. The red points were measured in the Cryogenic Gentle Nodal Suspension by the author, see chapters 3, 4, and 5 for details on the experiment and coated sample measurement process. The green curve is the same curve from Figure 12. The yellow curve is the modeled TED of the coating due to the coating-substrate interface from Zhou [20] via the equations of 2.143. The blue curve is the total loss from the substrate (green curve) and coating (yellow curve). The grey curve is the total thermoelastic dissipation (blue curve) plus the lowest mechanical loss measured for that mode. Therefore, the grey curve can be considered a loose minimum.	58

15	Modeled thermoelastic loss from 12 K to 300 K for the last four modes. Overlaid in red is experimentally determined data for the total loss of the AlGaAs-coated silicon resonators. The red points were measured in the Cryogenic Gentle Nodal Suspension by the author, see chapters 3, 4, and 5 for details on the experiment and coated sample measurement process. The green curve is the same curve from Figure 12. The yellow curve is the modeled TED of the coating due to the coating-substrate interface from Zhou [20] via the equations of 2.143. The blue curve is the total loss from the substrate (green curve) and coating (yellow curve). The grey curve is the total thermoelastic dissipation (blue curve) plus the lowest mechanical loss measured for that mode. Therefore, the grey curve can be considered a loose minimum.	59
16	Strain sensitivities of present (GEO, VIRGO, aLIGO, LIGO A+, KAGRA) and next generation detectors (LIGO Voyager, Cosmic Explorer, Einstein Telescope). Note that all curves except GEO600, AdVirgo, and aLIGO are all theoretical desired goals of these detectors. Image credit to Robie [21].	64
17	Strain sensitivity evolution of GEO600 from 2009 to 2013. Notice the large improvement at frequencies above 500 Hz, where implementation of quantum squeezing of light has pushed down quantum shot noise. Plot credit to Dooley [22].	65
18	An aerial view of AdVirgo, located in Santo Stefano a Macerata, Italy. Image credit to the VIRGO collaboration [23].	67
19	A picture of the KAGRA detector situated beneath the mountains it sits 200 m beneath. Photo courtesy: KAGRA Observatory, ICRR, The University of Tokyo [24].	68
20	A+ LIGO strain sensitivity for O3 and design curves for O4 and O5 [25]. The O5 curve is the design sensitivity of A+ [26]. Notice the O5 curve is roughly three times as sensitive as the O3 curve at 100 Hz. Coating thermal noise is the dominate noise source in this frequency regime.	69

21	AdVirgo strain sensitivity for O3 and design curves for O4 and O5. [27]. Notice that the O5 high curve, the least amount of sensitivity acceptable to meet the design goal, is roughly twice as sensitive as the O3 curve at 100 Hz. Coating thermal noise is the dominate noise source in this frequency regime.	69
22	The noise budget for Cosmic Explorer. Although all noise sources are significantly reduced as compared to their current generation counterparts, notice the order of magnitude drop in coating thermal noise (red line) from the A+ total curve (dashed light blue line). Image credit to Evans <i>et al</i> [10].	71
23	The Syracuse University Cryo-GeNS nodal support. Pictured is a 3 inch fused silica test sample balanced on a 25mm diameter \times 30mm focal length silicon plano-convex lens, provided by Edmund Optics. The black glass is used to dump any light that transmits fully through the sample. For bare silicon and AlGaAs-coated silicon samples, essentially zero light is transmitted, so the black glass is only necessary when testing the fused silica samples.	80
24	A diagram depicting the sample excitement and observation using an optical lever. First, a comb exciter rings up the resonant modes of sample. Next, a laser is reflected off the surface of the resonating sample. Lastly, the laser is passed through an optical lever into a QPD, where the Fourier Transform of the laser position will show the mode amplitudes decaying over time.	81
25	Differences in measured Q for the first butterfly mode of their fused silica sample. Each bar respresents a different centering point of the sample on the nodal support. The x and y axes are in units of μm , while the z axis is the unitless Q . Image credit Cesarini <i>et al</i> [4]. . . .	82
26	A view of the Cryo-GeNS from the lab entrance. Central to the picture is the coldhead, where compressed helium is pumped in and cycled through the system. Other important equipment is also labeled. . . .	86

27	Ambient ground motion of the top of the optics table (a) and the wall mount (b). Although they differ little in magnitude, this is unsurprising since the table is designed to mitigate noise at lower frequencies. Additionally, when the seismic noise of the table was measured, the table was not configured for optimal mitigation. This error was fixed before loss data was recorded.	87
28	Comparison of seismic noise of the lab floor. The green line was taken by David Kelley in 2010, while the purple was recorded by the author in 2021. Discrepancies can be explained by the fact that these were taken in two separate labs a decade apart, though they do share a wall and are on the same floor (sub-basement) of the physics building. . .	88
29	QPD noise depicted as an equivalent power fluctuation on the diode. The voltage noise measurement discussed has been converted to an equivalent power change on the QPD using equations 3.167 and 3.167, hence the y-axis units of $W/\sqrt{\text{Hz}}$	90
30	The optical lever of the Cryo-GeNS. The telescope is composed of the two lenses on the table between the laser and the QPD, and is used to minimize beam width on the QPD.	91
31	The inside of the sample chamber. Various important components are labeled. The chain that is driven by the motor can be seen underneath the thermal straps and stage on the bottom and right side of the apparatus. The stage, sample holder insets, and thermal straps are all composed of 101 oxygen free copper. These pieces were also baked at 480°C in a vacuum furnace to increase their thermal conductivity. . .	94
32	Four of the sample holder insets along with other Cryo-GeNS equipment. Three insets were made for each sample target diameter of 3 inches and 4 inches, totaling six sample holder insets. One inset had a diameter 30 thousandths of an inch larger than the sample target diameter, another had 30 thousandths of an inch smaller, while the last was exactly the sample target diameter.	96

33	A comparison of a ringdown of mode 3 ($m = 0, n = 3$) measured in the room temperature GeNS (left) and the Cryo-GeNS (right). Surprisingly, the residuals (red lines) between the fit and recorded ringdown appear significantly lower in the Cryo-GeNS, suggesting this mode has a cleaner ringdown in the Cryo-GeNS. This is probably due to a higher amplitude of oscillation by the mode in the Cryo-GeNS.	101
34	Two measurements of the quality factor Q of fused silica from 110 K to 300 K for the first mode. The larger relative spread in the data at low Q , or high mechanical loss ϕ , reflects the greater uncertainty that comes with measuring short ringdowns.	103
35	Loss angle over temperature for eight different resonant modes of a bare, 4 inch diameter, 500 μm thick, crystalline silicon substrate. The shape of each mode is given in table 3.	104
36	One of the AlGaAs coated silicon samples. The white bar across the sample is an artifact of the picture, and is a reflection of the wall behind the coating. The slight bumps on the face of the sample are defects from impurities on the silicon substrate surface, and do not have a measurable impact on coating mechanical loss measurements [6].	110
37	Loss angle of the coated sample over the temperature range from 12 K to 295 K for all the modes. The presence of a loss peak around 80 K signals influence from substrate thermoelastic dissipation; the magnitude of the peak indicates the how severe this influence is. . . .	111
38	Mechanical loss of the AlGaAs coating over the temperature range from 12 K to 142 K for all the modes. The points where measured substrate loss approaches the measured loss of the coated system have been removed, as the coating loss cannot be reliably calculated when the coated sample loss is not at least twice as large as the substrate loss. Perhaps the most noticeable trait of this data is the large spread in loss between the modes, with about a factor of 50 difference between the lowest and highest loss modes.	113

39	A fit of bulk and shear loss angles of the AlGaAs coating loss at 21 K. Since it is given a negative value by the fit, shear loss is not pictured. The shape and inaccuracy of the fit is found across all temperatures and if bulk loss is allowed to vary linearly with frequency. The fit becomes intolerably inaccurate when shear loss is restricted to positive values. When the shear fit is forced to be positive, it is found to be a very low value $\phi_c^{\text{Shear}} < 1 \times 10^{-7}$	117
----	--	-----

Preface

The work presented in this thesis stems from my participation in the LIGO-VIRGO-KAGRA Scientific Collaboration (LVK) from the fall of 2018 to spring of 2023, and it is an account of the research carried out therein.

LIGO DCC Number: P2300084

Chapter 1

Introduction

In this chapter the reader will be familiarized with the theoretical physics that were the first insight into the existence of gravitational waves. The introduction will also bridge the theoretical and experimental, as it will explore how one would go about using a basic Michelson interferometer to detect passing gravitational waves. Lastly, some upgrades to the basic Michelson will be discussed along with the noise sources present in such a detector.

1.1 Gravitational Waves

Einstein's theory of general relativity, published in 1915, in its most simple form states that matter dictates how spacetime curves, and spacetime dictates how matter moves [28]. This revolutionary theory is still, over one hundred years later, the best description of gravity today. For clarity, the word matter can be used to refer to either mass or energy, as they are interchangeable through the mass-energy equivalence, [29, 30]

$$E = mc^2\gamma. \quad (1.1)$$

General Relativity has correctly predicted precession of Mercury's orbit [31], gravitational lensing of light [32], gravitational redshift of light [33], and the conversion of mass to energy carried off in the form of gravitational waves [34]. General relativity's fundamental relationship is the Einstein Field Equation,

$$G_{\mu\nu} = 8\pi T_{\mu\nu}. \quad (1.2)$$

This tensor equation fully characterizes the interaction between spacetime and matter. Analytically solving this many coupled equations is often impossible, except in certain situations which simplify them. The first solution to be found was the Schwarzschild solution, which assumed no angular momentum, no electric charge, and complete spherical symmetry of the mass [35]. Although this solution is the simplest, it set physicists down a road of inquiry that would ultimately lead Oppenheimer, Tolman, and Volkoff to conclude in 1939 that beyond a certain mass limit no laws of physics could stop a highly compact object from collapsing to a black hole [36]. Though many physicists at the time believed these objects were just mathematical tricks of Einstein's Field Equation, today the existence of black holes is a well established fact supported by observations and theories too numerous to list.

In spacetimes where the curvature is nearly flat, the weak field approximation makes the equations much more tractable. In this case, the metric is described as

$$g_{\mu\nu} \simeq \eta_{\mu\nu} + h_{\mu\nu} \quad (1.3)$$

where $\eta_{\mu\nu}$ is flat spacetime and $|h_{\mu\nu}| \ll 1$ is a small perturbation manifested from a gravitational field. Under this approximation the vacuum solution, ($T_{\mu\nu} = 0$), will yield a wave equation,

$$(\nabla^2 - \frac{1}{c^2} \frac{\partial^2}{\partial t^2}) \bar{h}_{\mu\nu} = 0. \quad (1.4)$$

Note that $\bar{h}_{\mu\nu} = h_{\mu\nu} - \frac{1}{2} \eta_{\mu\nu} h^\alpha_\alpha$, and only in the transverse-traceless gauge will $\bar{h}_{\mu\nu} = h_{\mu\nu}$. The gauge conditions for the transverse-traceless gauge are

$$A^{\mu\nu} k_\nu = 0 \quad (1.5)$$

$$A^\mu_\nu = 0 \quad (1.6)$$

$$A_{\mu\nu} U^\nu = 0 \quad (1.7)$$

where $A^{\mu\nu}$ and k_ν are the coefficient and the wave number respectively of the complex solution to equation 1.4. \vec{U} is simply any constant four-velocity vector one wishes to create [37].

The wave that results from equation 1.4 is a gravitational wave. Stronger gravitational waves will produce a higher magnitude of $|h_{\mu\nu}|$, corresponding to a higher

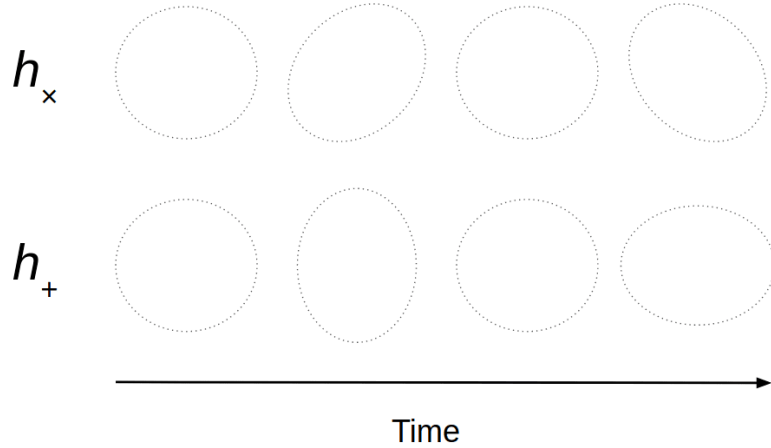


Figure 1 : A visual depiction of how a gravitational wave travelling through the plane of this thesis would alter the distances between point masses arranged in a circle. The two sets of figures labelled h_{\times} and h_{+} represent the two polarization states of a gravitational wave.

amplitude wave. The physical effect of a passing gravitational wave is a warping of spacetime, altering distances between fixed objects as shown in Figure 1. The relationship between length change δl and gravitational wave amplitude $h_{\mu\nu}$ is

$$\delta l = \int g_{\mu\nu} dx^{\mu} dx^{\nu} = \int_0^L g_{xx} dx \approx |g_{xx}(x=0)|^{\frac{1}{2}} \approx \left(1 + \frac{1}{2} h_{xx}(x=0)\right) L \quad (1.8)$$

where L is the initial separation. A greater initial separation will make a corresponding length change between the fixed objects, herein referred to as test masses, larger, and therefore easier to detect [37].

1.2 Birth and Evolution of Gravitational Wave Detectors

In 1957, many now famous physicists met at a conference sponsored by Joshua Goldberg [38] in Chapel Hill. Today we refer to this event as the Chapel Hill Conference, as it carries the significance of being the first recorded event where an experimental search for gravitational waves was seriously pursued in a collaborative setting. Commonly attributed to both Feynman and Pirani, the sticky bead argument was a thought experiment discussed to tackle the question of the physical existence of gravitational waves. Imagine two beads free to slide on a rigid rod, but currently at rest. As a gravitational wave passes through the rod, the beads would slide back and

forth and generate heat. This would prove that gravitational waves carry energy and are a physical effect [39, 40], giving motivation for experimentalists to hunt for these waves.

1.2.1 The First Attempts at Detecting Gravitational Waves

Joseph Weber would be the first to create an actual experiment with the goal of detecting gravitational waves. These detectors were cylinders of aluminum, referred to as Weber bars, that were thought to behave like antennae for gravitational waves. As a gravitational wave would pass through the bar, piezoelectric transducers covering the exterior of the bars would extract the energy at the resonant frequency; the bars would begin to resonate due to a passing gravitational wave. However, these Weber bars were only able to detect gravitational waves in an extremely limited frequency range and they were even further limited by thermal noise [41, 42].

When Weber announced that he had detected gravitational waves using these bars, the news was at first received with great excitement. However, over time the community began to find problems with Weber's detection events. Perhaps most worrying was a mismatch in time between the two labs where the bars were located, which were being correlated to reduce noise. One lab operated on Eastern Daylight Time while the other was on Greenwich Mean Time. Weber claimed to have found events in these data sets, even though they were four hours mismatched. Additionally, it was discovered that Weber's coincident events were statistically expected given the thermal noise of the bars [43]. It should be noted that these Weber Bars are a theoretically viable gravitational wave detector, however they lack the sensitivity required to observe gravitational waves.

1.2.2 The Michelson-Morley Interferometer

An alternative experiment to the Weber Bar method of detecting gravitational waves was first proposed on paper in 1972 by Rainer Weiss; his gravitational wave detector would be a highly sensitive Michelson Interferometer. Instead of measuring energy deposited, as solid bars do, an interferometer uses light to measure distance changes caused by a passing gravitational wave, effectively measuring the gravitational wave form [44].

As light travels through space, it acquires a change in phase depending on the distance it travels d and its wavelength λ . This can also be recast in terms of flight time t instead of flight distance,

$$\Delta\phi = 2\pi\frac{d}{\lambda} = 2\pi\frac{ct}{\lambda}. \quad (1.9)$$

When two light waves with the same wavelength combine, they will amplify, destroy, or have some combination of these two effects depending on the relative phase of the light waves,

$$I = I_1 + I_2 + 2\sqrt{I_1 I_2} \cos(\phi_1 - \phi_2). \quad (1.10)$$

Notice that if the phase difference between the light waves is $2\pi n$, then they will constructively interfere and the total intensity will quadruple. If their relative phase is $(2n + 1)\pi$, then they will destructively interfere and the total intensity will be 0. For clarity, n is any integer valued number.

A Michelson Interferometer uses the interference property of light to measure the phase change picked up by two lasers on orthogonal paths. First, laser light is directed towards a beamsplitter which sends half the light down each path. The light is then bounced back to the beamsplitter to recombine. After the light has recombined, it is then directed to a photodetector which reads out the intensity. See Figure 2 for a pictorial representation of a Michelson Interferometer. By measuring intensity after recombination, one is effectively measuring the phase difference between the two paths. This phase difference can be converted directly to a change in length, provided the length change does not exceed the wavelength of the light.

If a gravitational wave is propagating orthogonal to the plane created by the interferometer of Figure 2, then the gravitational wave amplitude is strictly a function of time. As stated above, gravitational waves warp spacetime, effectively altering lengths between fixed points. The null geodesic equation, or the path of a photon, in the frame where the interferometer is at rest is

$$ds^2 = -dt^2 + [1 + h(t)]dx^2 + [1 - h(t)]dy^2 + dz^2 = 0. \quad (1.11)$$

Here $h(t)$ is the gravitational wave strength. Notice that when spacetime is stretched in the x direction, it is compressed in the y direction. As a wave propagates normally

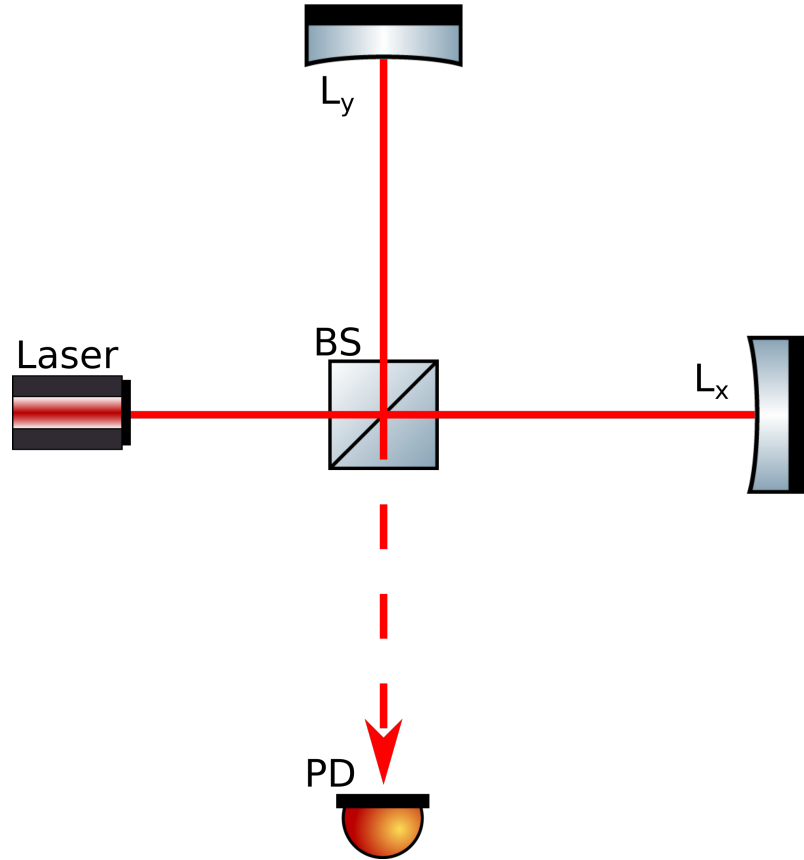


Figure 2 : The most basic version of a Michelson Interferometer. As the light travels through the x or y arms, it accumulates phase. The difference in phase between x and y cause them to recombine constructively or destructively, changing the power observed at the photodiode. BS is short for beamsplitter, PD is short for photodiode, L_x and L_y are the lengths of the x and y arms respectively. Henceforth, the photodiode that measures the recombined light power will be referred to as the anti-symmetric port.

through the plane of the interferometer whenever one arm is stretched, the other is compressed [42].

A photon travelling along the x and y arms have the following metric equations

$$\frac{dt}{dx} = \sqrt{1 + h(t)} \approx 1 + \frac{1}{2}h(t) \quad (1.12)$$

$$\frac{dt}{dy} = \sqrt{1 - h(t)} \approx 1 - \frac{1}{2}h(t). \quad (1.13)$$

We can then calculate the amount of time τ that photons in each arm take to reach their respective end mirrors,

$$\tau_{1,x} = \int_0^{L_x/c} [1 + \frac{1}{2}h(t)]dt \quad (1.14)$$

$$\tau_{1,y} = \int_0^{L_y/c} [1 - \frac{1}{2}h(t)]dt. \quad (1.15)$$

L_x and L_y are the lengths between beamsplitter and end mirrors for the x and y arms. Additionally, the limits of integration reflect a unit conversion between time and distance; for light travelling solely in the x direction $dt = dx/c$. The same holds true for light travelling in the y direction. The total flight time must also incorporate the trip back from end mirror to return to the beamsplitter,

$$\tau_x = 2\frac{L_x}{c} + \frac{1}{2} \int_0^{L_x/c} [h(t) + h(t + \frac{L_x}{c})]dt \quad (1.16)$$

$$\tau_y = 2\frac{L_y}{c} - \frac{1}{2} \int_0^{L_y/c} [h(t) + h(t + \frac{L_y}{c})]dt. \quad (1.17)$$

Since the period of the gravitational wave will be much longer than the time of flight for the photons in the arms, we can simplify the above by saying $h(t) = h$ where h is a constant. This also means $h(t + \frac{L_i}{c}) \approx h$. If we set $L_x = L_y$ along with the constant h simplification, the difference in flight time becomes

$$\Delta\tau = \tau_x - \tau_y = 2\frac{L}{c}h. \quad (1.18)$$

Making use of equation 1.9, we can recast the above in terms of the phase difference

between the two beams,

$$\Delta\phi = \frac{4\pi hL}{\lambda}. \quad (1.19)$$

The simplification of declaring h a constant allows us to accelerate the math, however it also allows the unphysical ability to make the arm length arbitrarily long. In reality, h is a function of time and the arm length will affect the sensitivity depending on gravitational wave frequency. This problem is fixed by giving the wave the much more physical mathematical form of $h(t) = h_0 e^{i2\pi f_{\text{GW}} t}$. Repeating the steps between equations 1.14 and 1.19, we then arrive at the following expression for the phase difference between the two arms,

$$\Delta\phi(t) = h(t)\tau_{\text{RT}} \frac{2\pi c}{\lambda} \text{sinc}(\pi f_{\text{GW}}\tau_{\text{RT}}) e^{i\pi f_{\text{GW}}\tau_{\text{RT}}}. \quad (1.20)$$

Note that $\tau_{\text{RT}} = 2L/c$. Additionally, there exists a recurring zero point in the equation whenever $f_{\text{GW}}\tau_{\text{RT}} = n$ where n is any integer equal to or greater than 1.

How does one explain this zero point? Let's unpack f_{GW} a little bit to tease out the answer. f_{GW} is the frequency of the gravitational wave, but that can also be expressed as c/λ_{GW} where λ_{GW} is the wavelength of the gravitational wave. Let's say that λ_{GW} equals the unchanged arm length, $2L$. This leaves us with a sinc function that equals zero, and explains the physics of the zero point. A gravitational wave that passes one wavelength through the detector in the amount of time $2L/c$, which is the same as the light travel time through the unchanged arms, will equivalently expand and then contract the light travel distance. In other words, whatever time is lost by the arm length expanding, will then be immediately undone by time being gained with the arm length contracting.

This can be seen visually by graphing equation 1.20. The zero points are evident in Figure 3, where the accumulated phase drops to 0 in regular intervals starting at a minimum gravitational wave frequency. Notice that this minimum frequency is much higher for a 4 km arm length than for a 100 km arm length. This is expected behavior based on the form of equation 1.20 and its physical interpretation above. The choice of 4 km as a comparison is chosen because that is the length of the current generation of gravitational wave detectors, pictured in Figure 4. A map of all current generation gravitational wave detectors is shown in Figure 5.

The next logical question to ask is how well a single interferometer as described

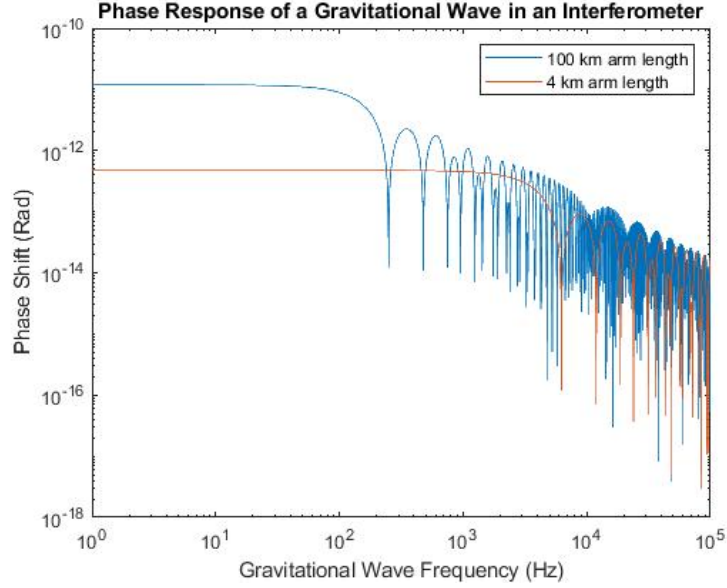


Figure 3 : Accumulated phase shift in an ideal 4 km and 100 km interferometer assuming a gravitational wave strain $h_0 = 10^{-23}$ and laser wavelength $\lambda = 1064$ nm.

above would be able to detect gravitational waves from astrophysical objects or events, as that is the goal of the LIGO detectors [45]. The distance at which the detector can observe an event with a given signal-to-noise Ratio (SNR) is called the horizon distance, and is given by

$$\rho = \sqrt{4 \int_{f_{\text{low}}}^{f_{\text{high}}} \frac{|\tilde{h}(f)|^2}{S_n(f)} df} \quad (1.21)$$

where ρ is the desired signal-to-noise ratio, \tilde{h} is the Fourier Transform of the expected waveform, and $S_n(f)$ is the one-sided average power spectral density of the detector noise [46]. The lower limit frequency, f_{low} , is determined by low frequency noise limitations, and for aLIGO is around 20 Hz [47]. The upper frequency limit, f_{high} , is given by the innermost stable circular orbit (ISCO) frequency

$$f_{\text{high}} = f_{\text{ISCO}} = \frac{c^3}{6\sqrt{6}\pi GM} \quad (1.22)$$

where M is the mass of the binary system. For a binary neutron star system with constituent masses of $1.4M_{\odot}$, $f_{\text{ISCO}} = 1570$ Hz [46].

\tilde{h} is difficult to define in general terms, but we can do it for a specific astrophysical event of our choosing. Imagine two compact objects, such as neutron stars, in a

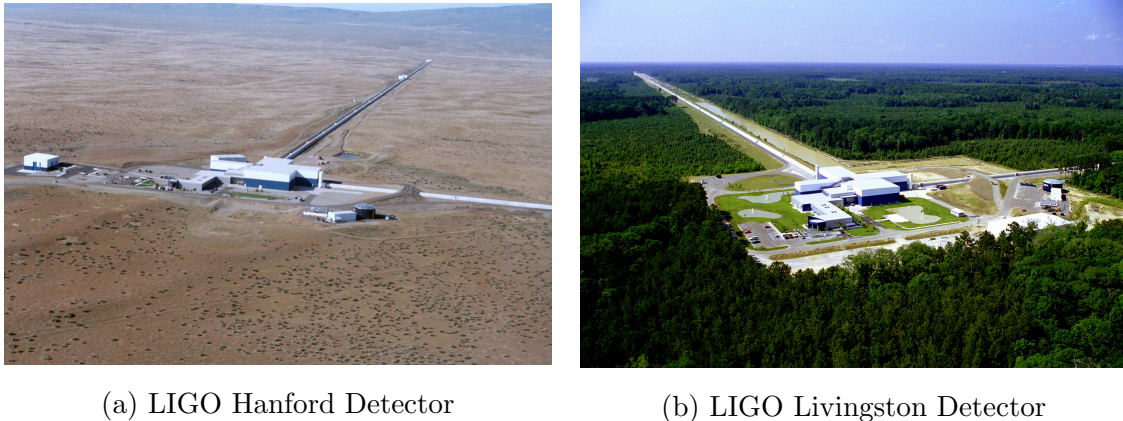


Figure 4 : The two LIGO detectors at Hanford, Washington [14] and Livingston, Louisiana [15], respectively. The arms extending off the main building 90° from each other are the 4 km beam tubes of the interferometer. Light travels down each path and recombines, sometimes with their relative phase altered by a passing gravitational wave, in the main building.

circular orbit with one another. In order to maximize signal from the source, we assume the objects are localized in the sky directly overhead the detector and the plane of their orbit is in the same plane as our detector arms. The signal which reaches our detector is given by [48]

$$\tilde{h}(f) = \frac{1}{d_H} \left(\frac{5\pi}{24c^3} \right)^{1/2} (G\mathcal{M})^{5/6} (\pi f)^{-7/6} e^{i\Psi(f;M)} \quad (1.23)$$

using the notation of Brown [49]. \mathcal{M} is defined as the chirp mass and is given by

$$\mathcal{M} = \frac{(m_1 m_2)^{3/5}}{(m_1 + m_2)^{1/5}} \quad (1.24)$$

where m_1 and m_2 are the individual masses of the two compact objects. d_H is the horizon distance, and $\Psi(f; M)$ is a real function of frequency parametrized by the total mass [47]. Setting the signal to noise ratio to $\rho = 8$ and by substituting equation 1.23 into equation 1.21 we can solve for horizon distance d_H ,

$$d_H = \frac{1}{8} \left(\frac{5\pi}{24c^3} \right)^{1/2} (G\mathcal{M})^{5/6} \pi^{-7/6} \sqrt{4 \int_{f_{\text{low}}}^{f_{\text{high}}} \frac{f^{-7/3}}{S_n(f)} df}. \quad (1.25)$$

Our assumption of an optimally aligned and sky located binary can be undone by a very simple division of 2.26, accounting for averaging over all possible sky locations

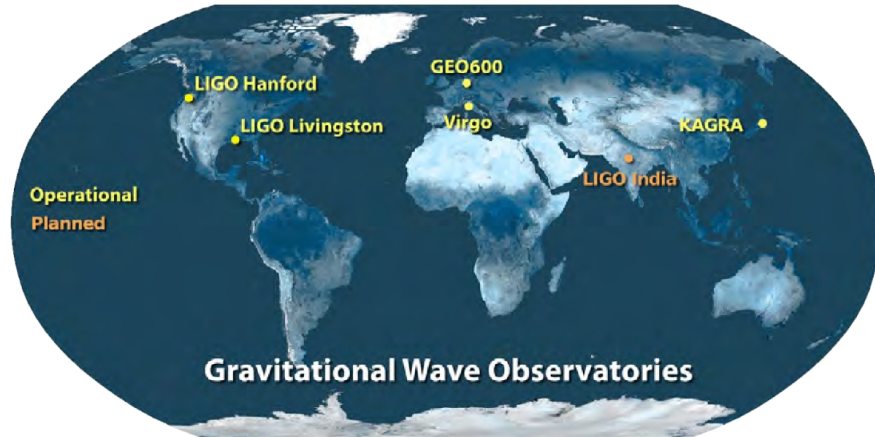


Figure 5 : A map showing the locations of all gravitational wave observatories, operational and planned. The current global gravitational wave detector network consists of the twin LIGO detectors in the United States, GEO600 and VIRGO observatories in Europe, and the KAGRA observatory in Japan. There is another planned detector to be built in India. This map does not include next generation detectors projected to be built in the 2030s and 2040s.

and orientations [48]. This gives a quantity known as the sensemon range, and is more commonly used to describe detector sensitivity. At the time of LIGO's first detection, this range was 1.3 Gpc for a coalescing black hole binary with constituent masses of $30M_{\odot}$ and 70-80 Mpc for a binary neutron star system (BNS) [50]. With subsequent upgrades to the detector since the first observation in 2015, the fourth observing run, O4, is expected to have a range of 160-190 Mpc for binary neutron star mergers. This will lead to a detection rate of $7.7^{+11.9}_{-5.7}$ BNS events per year [51].

1.2.3 Sidebands

The influence a gravitational wave has on the light in the arms was demonstrated through equation 1.20. Although not explicitly stated, it was implied that this phase difference was enough for us to observe the effect of a gravitational wave passing through our detector. However, the photodiode depicted in Figure 2 measures incident power, not the phase difference of the light in the two arms. It may seem like an arbitrary difference given the relationship between power and phase difference, but the relationship has subtleties that must be understood if one is going to operate an interferometer to its maximum level of precision.

Operating the detector such that the light recombines entirely in phase when it

returns to the beamsplitter in the presence of no gravitational waves is the most obvious starting point. Any passing wave would make the power drop, which intuitively leads one to believe it is the best method to run the interferometer; this is called operating on a bright fringe [42]. Assuming the input field at the beamsplitter is E_0 , then $iE_0/\sqrt{2}$ is transmitted down the x-arm while $E_0/\sqrt{2}$ is reflected up the y-arm. By the time they return to the beamsplitter and recombine, each of the fields has accrued phase ϕ_x and ϕ_y respectively. After arriving at the beamsplitter again, the fields

$$E_x = \frac{iE_0}{2}e^{2i\phi_x} \quad (1.26)$$

$$E_y = \frac{iE_0}{2}e^{2i\phi_y} \quad (1.27)$$

are transmitted directly to the anti-symmetric port. Since the fields combine linearly, a simple addition $E_{out} = E_x + E_y$ gives us the total field at the anti-symmetric port. The relationship between field and power at the anti-symmetric port, P_{AS} , is given by

$$P_{AS} = \int_{\text{Area}} |E_x^2 + E_y^2| dA = \cos^2(\Delta\phi) \int_{\text{Area}} |E_0^2| dA \quad (1.28)$$

where $\Delta\phi = \phi_x - \phi_y$. It is also worth noting that $\int_{\text{Area}} |E_0^2| dA$ is simply the power entering the Michelson before the beamsplitter, which is denoted P_{in} .

Since $\Delta\phi$ is so small in magnitude, see the y-axis of Figure 3, the small angle approximation can be used to rewrite equation 1.28,

$$P_{AS} \approx P_{in}(1 - 2\Delta\phi). \quad (1.29)$$

The gravitational wave signal resides entirely in $\Delta\phi$, but that is being hidden behind a huge DC term of P_{in} . Operating on a bright fringe makes it nearly impossible to distinguish between small changes caused by a passing gravitational wave or noise. Additionally, in section 1.3.2, it will be explained how increasing power in the arms increases detector sensitivity. With this operating method, any benefit of increasing power would be lost. This benefit is explicitly defined later, by equation 1.53.

The next logical conclusion would be to operate at the opposite of a bright fringe, when the interferometer transmits no power when a gravitational wave signal is not present; this is called a dark fringe or a null-point operation. Functionally, this adds

an additional phase of $\pi/2$ to $\Delta\phi$ in equation 1.28. The power on the anti-symmetric port then takes on a different form,

$$P_{\text{AS}} = P_{\text{in}}(\Delta\phi)^2. \quad (1.30)$$

Now there is a second order dependence on gravitational wave signal that is known to be very small; see equation 1.20 and Figure 3. For reference, the peak gravitational wave strain $h(t)$ that was observed in the first binary black hole (BBH) merger event, GW150914, was just 1.0×10^{-21} [1]. This mode of operation is therefore far from optimal.

A much better way of operating a gravitational wave interferometer is to modulate the input laser frequency, referred to as heterodyne detection. Such modulation results in the following field at the input

$$E_{\text{in}} = E_0 e^{i(\omega t + \beta \cos(\Omega t))} \quad (1.31)$$

where Ω is the modulation frequency. Expanding to first order using the Bessel functions yields

$$\begin{aligned} E_{\text{in}} &\approx E_0 e^{i\omega t} [J_0(\beta) + J_1(\beta) e^{i\Omega t} + J_1(\beta) e^{-i\Omega t}] \\ &= E_{\text{C,in}} + E_{\text{SB+,in}} + E_{\text{SB-,in}} \end{aligned} \quad (1.32)$$

where β is the modulation depth. The first term is the carrier field, while the second and third terms are the upper and lower sidebands respectively. This mode of interferometer operation is depicted in Figure 6.

Since there are now three fields to keep track of, it is useful to define an optical transfer function t that connects the fields at the input to their respective outputs,

$$E_{\text{out}} = E_{\text{C,out}} + E_{\text{SB+,out}} + E_{\text{SB-,out}} = \begin{bmatrix} t_{\text{C}} \\ t_{\text{SB+}} \\ t_{\text{SB-}} \end{bmatrix} (E_{\text{C,in}} + E_{\text{SB+,in}} + E_{\text{SB-,in}}). \quad (1.33)$$

For a null-point operation, t_{C} is given by equation 1.30. The sideband transfer functions are given by

$$t_{\text{SB}\pm} = r_{x,\pm} e^{i\phi_{x,\pm}} - r_{y,\pm} e^{i\phi_{y,\pm}} \quad (1.34)$$

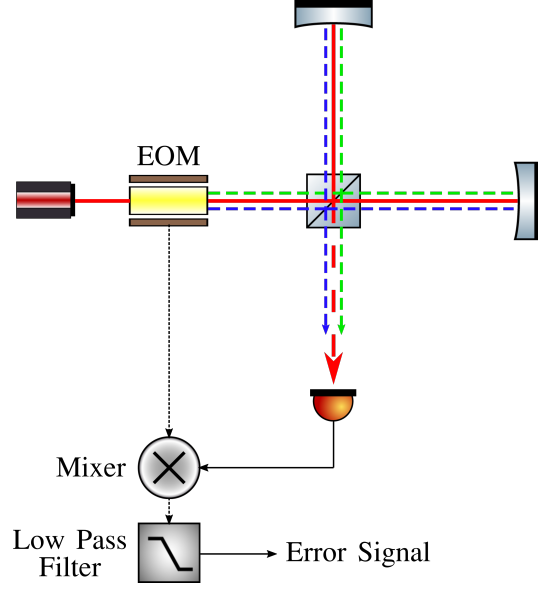


Figure 6 : A Michelson Inteferometer with a heterodyne detection scheme.

$$\phi_{i,\pm} = (k \pm k_{\Omega})l_i = \left(\frac{\omega + \Omega}{c}\right)l_i \quad (1.35)$$

where k and k_{Ω} are the carrier wave number and sideband wave number respectively [47]. Substituting the above transfer functions into equation 1.33 yields the electric field at the anti-symmetric port,

$$E_{\text{out}} = ie^{i\omega t} [J_0(\beta)kl_+h_+ + J_1(\beta)\sin(k\Delta l + k_{\Omega}\Delta l)(e^{i\Omega t} + e^{-i\Omega t})]. \quad (1.36)$$

In the above, $l_+ = \frac{l_x + l_y}{2}$ is the average arm length and $\Delta l = \frac{l_x - l_y}{2}$ is the average differential arm length. Arranging the carrier as a null point operation now, where $k\Delta l = \pi/2$, does not place the sidebands also exactly at a dark fringe, since they accrue phase slightly differently than the carrier. This leaking of the sidebands onto the anti-symmetric port is known as the Schnupp Asymmetry [52]. With this in mind, equation 1.36 becomes

$$E_{\text{out}} = ie^{i\omega t} [J_0(\beta)kl_+h_+ + J_1(\beta)\sin(k_{\Omega}\Delta l)(e^{i\Omega t} + e^{-i\Omega t})] \quad (1.37)$$

The intensity at the output, $I_{\text{out}} = |E_{\text{out}}|^2$, can be unpacked to make it easier to

tease out the gravitational wave signal,

$$I_{\text{out}} = |E_C|^2 + |E_{\text{SB}+}|^2 + |E_{\text{SB}-}|^2 + 2\text{Re}\{E_{\text{SB}+}E_{\text{SB}-}^*e^{2i\Omega t}\} + 2\text{Re}\{(E_C E_{\text{SB}-} + E_C^* E_{\text{SB}+})e^{i\Omega t}\}. \quad (1.38)$$

The last term is known as the beat note between the carrier and the sidebands. One can use a mixer to extract this term at the modulation frequency. A mixer simply outputs the product of two electric signals. If the same oscillator that was used to modulate the signal, $\cos(\Omega t)$, is used as the other mixer input, the resulting mixer output is the demodulated signal,

$$I_{\text{demod}} \propto \left[4\pi J_0(\beta)J_1(\beta)\frac{l_+}{\lambda}\sin(k_\Omega\Delta l)h_+\right] [\cos(\Omega t)\sin(\Omega t + \phi_{\text{demod}})] \\ \propto \left[4\pi J_0(\beta)J_1(\beta)\frac{l_+}{\lambda}\sin(k_\Omega\Delta l)h_+\right] [\sin(\phi_{\text{demod}}) + \sin(2\Omega t + \phi_{\text{demod}})]. \quad (1.39)$$

ϕ_{demod} is set by the researcher to offset additional phase shifts, such as those caused by long cables.

The output of the mixer will have signals at DC, Ωt , $2\Omega t$, etc. but the DC signal is most interesting due to its relationship to the gravitational wave strain,

$$S = 4\pi J_0(\beta)J_1(\beta)\frac{l_+}{\lambda}\sin(k_\Omega\Delta l)\sin(\phi_{\text{demod}})h_+. \quad (1.40)$$

It now becomes evident why heterodyne detection is a superior way to operate an interferometer to detect gravitational waves; the signal scales linearly with gravitational wave strain, h , and there is no large DC term that washes out the signal. When the carrier is operated on a dark fringe $\Delta l = \frac{k_\Omega}{k} \frac{\pi}{2}$ and the researcher is able to optimize the Schnupp asymmetry length for a given modulation frequency. The benefit of this method, where the sidebands are created by an Electro-Optic Modulator (EOM) introduced before the beamsplitter, is dependent on the stability of the local oscillator. It was proven to be feasible and was implemented in Enhanced LIGO [53].

Advanced LIGO employs a homodyne detection method called DC-Readout. It is very similar to heterodyne detection, but instead the carrier is operated just off the dark fringe so that a small amount of the carrier reaches the anti-symmetric port when no gravitational wave is present. A passing gravitational wave will produce sidebands on the carrier, and the resulting beat note will have a linear relationship

with gravitational wave strain; similar to the heterodyne method. However the DC-Readout has the benefits of being naturally co-aligned and mode matched with the signal field. The differences between heterodyne and homodyne lie in the technical noises such as laser intensity fluctuations and quantum effects [54]. Noise sources will be further explored in section 1.3.

1.2.4 The Fabry-Pérot Cavity

As shown in Figure 3, a 4 km detector is a theoretically good choice for exploring gravitational wave signals at frequencies below roughly 5 kHz. However, in reality we lose performance at important frequencies, such as 100 Hz. Recall from the set up for Equation 1.18 the unit conversion between time and distance $t = L/c$. There was an implicit assumption here; that the light would take one round trip through the arms before recombining. This allowed us to simply use the arm length for L .

However, we could gain more signal if the light took multiple trips back and forth in the arm cavities, increasing the optical path the light takes and effectively increasing the arm length. One method to achieve this is a Herriott delay line, where the light bounces around multiple different spots on the test masses. Another method for building power in the arms is to create a Fabry-Pérot cavity (or resonator). Both are shown in Figure 7.

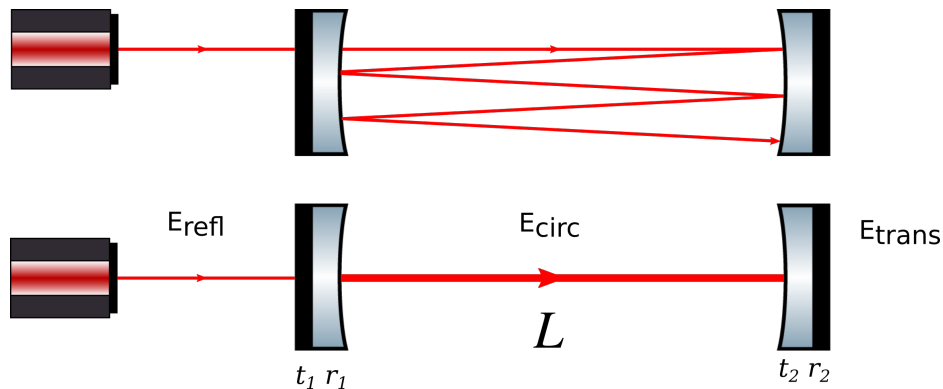


Figure 7 : Pictured is an example of a Herriott Delay line (top) and a Fabry-Pérot cavity (bottom). All gravitational wave interferometers, in operation or in development, use the Fabry-Pérot cavity to build power in the arms. See equations 1.41, 1.42, and 1.43 for a quantitative description of the three noted electric fields.

A Fabry-Pérot cavity is created by finely tuning the length between two partially

transmitting mirrors. When one spaces the mirrors such that a round trip in the cavity by a beam of light results in no phase change of the light, that is to say the electric field at beginning and end are exactly the same phase, the light will constructively interfere. Due to the small wavelength of light, 1064 nm in the LIGO-VIRGO-KAGRA (LVK) detectors, holding the mirrors at the correct distance is very difficult, but not impossible.

Consider the Fabry-Pérot cavity system pictured in Figure 7. The cavity is held at length L and the two mirrors have transmission and reflection coefficients given by t_1 , t_2 , r_1 , and r_2 . A plane wave entering the input mirror with amplitude E_0 will enter the cavity and propagate back and forth between the two mirrors. There are three fields to think about: transmitted, reflected, and circulating. In Figure 7, these fields would be located after the cavity, before the cavity, and in the cavity respectively. These three fields are all given by different geometric series which reduce to the following,

$$E_{\text{trans}} = t_{\text{FP}} E_0 = \left(\frac{t_1 t_2 e^{-ikL}}{1 - r_1 r_2 e^{-i2kL}} \right) E_0 \quad (1.41)$$

$$E_{\text{refl}} = r_{\text{FP}} E_0 = \left(-r_1 + \frac{t_1^2 r_2 e^{-2ikL}}{1 - r_1 r_2 e^{-i2kL}} \right) E_0 \quad (1.42)$$

$$E_{\text{circ}} = c_{\text{FP}} E_0 = \left(\frac{t_1}{1 - r_1 r_2 e^{-i2kL}} \right) E_0. \quad (1.43)$$

These fields are very sensitive to the phase accumulated in the round trip; the cavity becomes resonant when $L = n\lambda/2$. Resonance is when the circulating coefficient is maximized, which in turn means that the field circulating in the arms is maximized [42]. The value of this coefficient is codified in the gain, and is given by

$$\text{Gain} = c_{\text{FP}}^2|_{L=n\lambda/2} = \left(\frac{t_1}{1 - r_1 r_2} \right)^2 \quad (1.44)$$

In the first observing run where gravitational waves were observed, the circulating power was just under 100 kW [55]. The target circulating power for the current detectors is 750 kW, which would give a design sensitivity of 200 Mpc binary neutron star detection range [56].

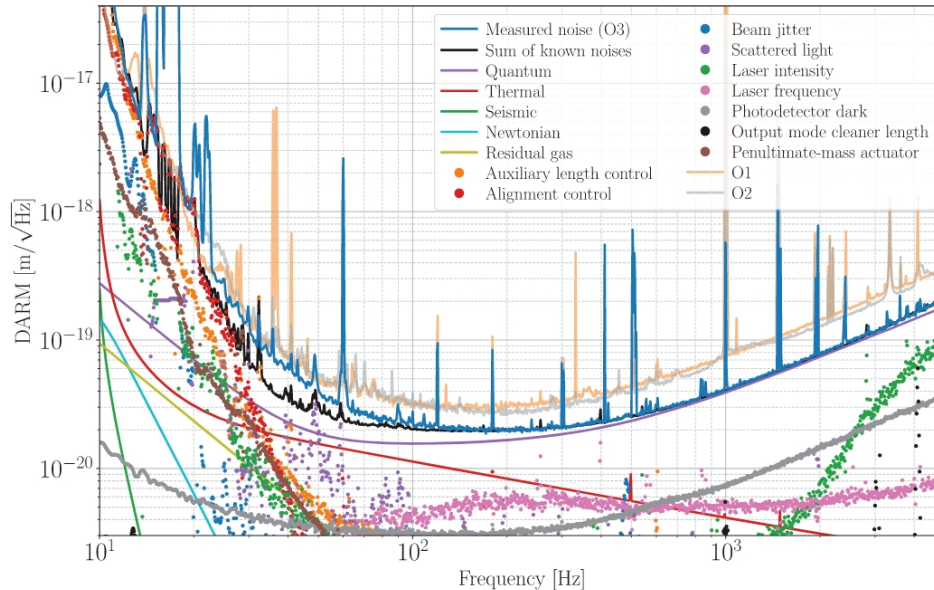


Figure 8 : A graph depicting the sensitivity of the LIGO Hanford Observatory in the most recent observing run, O3. The x-axis has units of frequency, while the y-axis is units of $\text{m}/\sqrt{\text{Hz}}$. Therefore, any gravitational wave that causes a length change at a given frequency that is smaller than the corresponding measured noise, the solid blue line, will be drowned in the noise and unable to be detected. Conversely, any stronger gravitational wave that falls above the blue line can be detected. Graphs such as these are often referred to as noise budgets [16]. The DARM of the y-axis stands for Differential ARM length. Often the y-axis will have units of $1/\sqrt{\text{Hz}}$ instead of $\text{m}/\sqrt{\text{Hz}}$. To convert from $\text{m}/\sqrt{\text{Hz}}$ to $1/\sqrt{\text{Hz}}$, one must simply divide by the arm length. For the LIGO Hanford observatory, that would be 4,000 meters.

1.3 Noise Sources in Gravitational Wave Interferometers

In previous sections, the theory behind how a gravitational wave interferometer operates was discussed. There are myriad sources of noise that serve to effectively lower the sensitivity of the detector [42]. All of the notable sources of noise are shown in Figure 8. In the coming sections a few of the major sources of noise will be discussed. The rest of the thesis will explore the causes and possible mitigation of thermal noise, the red line in Figure 8.

The units of $\text{m}/\sqrt{\text{Hz}}$ in Figure 8 are explained by the nature of how the curves are derived. Each curve on the plot is an amplitude spectral density (ASD). An ASD is simply the square root of a power spectral density (PSD). A PSD is defined as the

Fourier transform of the autocorrelation function of a time series,

$$P_s(f) = \frac{1}{\sqrt{2\pi}} \int_{-\infty}^{\infty} s \star s(\tau) e^{-i2\pi f\tau} d\tau. \quad (1.45)$$

Note that $s \star s(\tau)$ is defined as the autocorrelation function,

$$s \star s(\tau) \equiv \int_{-\infty}^{\infty} s(t)s(t+\tau)dt. \quad (1.46)$$

In the above equations, f is frequency, t is the time of the time-series data being analyzed, τ is the interval of time away from t over which the signal is being auto-correlated. A PSD of a time series with units of meters (the interferometers measure arm length over time) will have units of m^2/Hz . Therefore, the ASD shown in Figure 8 has units of $\text{m}/\sqrt{\text{Hz}}$. Ultimately, the $\sqrt{\text{Hz}}$ reminds the reader that independent frequency bands in a noisy time series add in quadrature, not linearly, in amplitude. It is only in power, or energy, that they add linearly [42].

1.3.1 Seismic, Newtonian, and Residual Gas Noise

The LVK detectors are all ground-based interferometers, and as such one must consider the motion of the ground on which the detectors are built. The ambient noise introduced by seismic activity at 100 Hz is of the order of $10^{-11} \text{ m}/\sqrt{\text{Hz}}$, but a detector must be sensitive to $10^{-20} \text{ m}/\sqrt{\text{Hz}}$ [57].

In order to damp the seismic noise, the test masses are suspended on a quadruple pendulum incorporating four stages of steel blade springs for enhanced vertical isolation. The effect of such a system is to low pass filter any seismic noise below the resonant frequency. Thus any seismic noise above 20 Hz is sufficiently damped, as shown by the green line in Figure 8 [58, 59].

Active isolation is necessary to supplement the passive isolation described above. Specifically, active isolation is needed for actuation of active feedback control loops [60]. The noise introduced by these systems can be seen in the red and orange dots of Figure 8 which drive the noise at the low frequency limits of the detector. By using multiple stages of actively controlled platforms, the noise contribution above 1 Hz can be suppressed [60–62].

Newtonian noise is closely linked to the seismic noise. Movement of the Earth's

crust causes local high or low density regions to spontaneously move about beneath the detector. This changes the local gravitational field felt by the test masses enough to influence the detector output. Given the cause of the changing gravitational field is also seismic in nature, it is unsurprising to learn that this phenomenon is most significant at low frequencies. Although it is impossible to shield the test masses from fluctuating gravitational fields, this noise source can be mitigated via subtraction using environmental sensors and seismometers [63, 64].

In addition to the shifting ground beneath the test masses, air molecules colliding with a test mass imparts a force onto it. The magnitude of this force can be quantitatively derived. A rectangular test mass with crosssectional area A at rest in a bath of gas molecules will have the following rate of collisions with those molecules [42],

$$\mathcal{N} = \frac{1}{4}n\bar{v}A = nA\sqrt{\frac{k_BT}{2\pi\mu}}, \quad (1.47)$$

where μ is the mass of a gas molecule and n is the number density of the gas molecules. Assuming elastic collisions, this collision rate corresponds to a mean force on one face of the test mass of

$$F_+ = nk_BT A. \quad (1.48)$$

Since the force applied involves impacts by discrete molecules, it will follow Poisson statistics. In an integration time τ , there will be a fluctuation in the total number $N\tau$ of molecules hitting one face of the plate, given by the following,

$$\frac{\sigma_{N\tau}}{N\tau} = \frac{1}{\sqrt{N\tau}}. \quad (1.49)$$

This yields a force noise of order

$$\sigma_F^2 \sim (k_BT)^2 \frac{nA}{\bar{v}\tau}. \quad (1.50)$$

Finally, this can be converted into a net force power spectrum given by

$$F^2(f) \sim (k_BT)^2 \frac{nA}{\bar{v}}. \quad (1.51)$$

For test masses that must have an accuracy smaller than the width of an atomic

nucleus, the force of the air molecules is much too large to be acceptable. Furthermore, any air through which the beam propagates will scatter the light, causing phase noise. These are both rectified by holding the relevant portions of the interferometer at high vacuum of 10^{-8} torr or less [65].

1.3.2 Quantum Phenomena: Shot Noise and Radiation Pressure Noise

As was discussed in section 1.2.2, measuring a gravitational wave in an interferometer is carried out by measuring a change in power due to a phase shift caused by the passing wave. Very literally, how well one can observe a gravitational wave is equivalent to how well one can count discrete photons hitting the anti-symmetric port. However, the photons do not arrive continuously nor regularly. This effect is known as shot noise.

In other words, one must count a discrete number of independent events described by a mean number of events per counting interval, \bar{N} . The set of outcomes for such a system is described by Poisson statistics, yielding the following probability distribution $p(N)$,

$$p(N) = \frac{\bar{N}^N e^{-\bar{N}}}{N!}. \quad (1.52)$$

After applying Poisson statistics to calculate the fractional fluctuations in photon arrival, one can extrapolate the brightness fluctuations and in turn the equivalent gravitational wave noise [42],

$$h_{\text{shot}} = \frac{1}{nL} \sqrt{\frac{\hbar c \lambda}{2\pi P_{\text{in}}}}. \quad (1.53)$$

In the above equation n is the number of round trips the light takes inside the Fabry-Pérot cavity, L is the length of the cavity, λ is the wavelength of light, and P_{in} is the input power. With an input power P_{in} of 20 W and a circulating power of 100 kW, the power in the arms when the first detection was made, $n = 5000$ [56]. The arm length L is 4 km and wavelength λ is 1064 nm. With these numbers, one obtains a white amplitude spectral density $h_{\text{shot}} = 8.16 \times 10^{-25} \text{ Hz}^{-1/2}$.

The rising quantum noise at high frequencies in Figure 8 is caused by the Fabry-Pérot cavities reshaping the shot noise behavior [47]. This is due to the fact that the interferometer response to a passing gravitational wave will decrease once the

gravitational wavelength drops below $4L$. This is shown in Figure 3 and explored in section 1.2.2. More information on the shot noise and other quantum noises of more complicated interferometer designs are given by Buonanno, Chen, and Kimble [66–68].

In addition to shot noise, there is another quantum effect that influences the detector, radiation pressure. This arises from the pressure the test masses feel from the photon flux imparted onto their surface in the cavity. With the cavities circulating hundreds of kilowatts of power, this effect is substantial. In order to derive an expression for this effect, one should start by considering the force exerted by an electromagnetic wave reflecting normally off a surface. By contemplating the shot noise fluctuation in this force, one arrives at the following expression [42]

$$h_{\text{rp}}(f) = \frac{n}{mf^2L} \sqrt{\frac{\hbar P_{\text{in}}}{2\pi^3 c \lambda}} \quad (1.54)$$

where m is the mass of the test mass. Using the numbers from the first detection chosen for equation 1.53 and a mass of 40 kg for the test mass [56], the magnitude of this noise can be quantified; $h_{\text{rp}}(f = 100 \text{ Hz}) = 1.018 \times 10^{-24} \text{ Hz}^{-1/2}$.

In a physical interferometer, shot noise and radiation pressure noise will add in quadrature. Unfortunately, minimizing one noise source often raises the other. Increasing power lowers shot noise due to the benefits of large number statistics, but increases radiation pressure noise due to more radiation being present in the cavity. Increasing the number of round trips the light takes in the cavity behaves the same way while increasing wavelength does the opposite, lowering radiation pressure at the expense of increased shot noise. Raising the mass of the test masses does reduce radiation pressure with no influence on shot noise, however there are technological and engineering limitations to how large a test mass can get. Only by increasing the length of the arms can one simultaneously lower both sources of noise, which is the primary motivation behind the increased size of planned next generation detectors [9, 10].

Chapter 2

Coating Thermal Noise and the Test Masses

The astute reader will notice that a major noise source was omitted from summary in the previous chapter, thermal noise. As was alluded to in the introduction of section 1.3, mitigating thermal noise is the driving motivation behind this thesis experiment. This chapter will serve to familiarize the reader with every aspect of thermal noise as it pertains to gravitational wave interferometers. The most relevant form of thermal noise is mechanical or Brownian noise. Discussion will focus on this form, but there will also be a detailed examination of thermoelastic dissipation. There will first be a discussion on the physical nature of thermal noise, or rather noises. This will be followed by a section detailing how one would go about modeling and predicting thermal noise for different materials.

Once the theoretical discourse is exhausted, the focus will shift to the physical detectors. The reader will be familiarized with the optical demands of the test masses, which will explain why all gravitational wave detectors are required to coat their test masses in material that is relatively high in thermal noise as compared to the bulk of the test mass. The thermal noise levels of past, present, and future detectors will also be explored.

2.1 The Theory of Coating Thermal Noise

In section 1.3.2, the quantum nature of light was discussed as a limiting noise source. However, the quantum nature of the test masses was completely ignored. The test masses are made of molecules which are constantly vibrating back and forth, and as such there is a limit to how precisely its position can be determined. Einstein first characterized such a phenomenon, called Brownian Motion [69]. Nyquist found similar behavior two decades later in the fluctuating voltage across resistors [70]. Although the systems examined by Einstein and Nyquist were radically different, they both are the result of a more general theory applied to their experiments. This theory is called the Fluctuation-Dissipation Theorem (FDT).

The other source of thermal noise alluded to in the introduction is thermoelastic loss. There exists a coupling between the elastic and temperature fields in solid structures; when objects are deformed away from their equilibrium shape, this creates local temperature differentials. This temperature gradient dissipates energy as the heat flows from warm areas to cooler ones, which manifests as a displacement noise. This noise source will be explored in detail in section 2.1.3. See section 2.2 for information on the levels of thermal noise in current and next-generation detectors, and motivation as to why the community wishes to study means of lowering it.

2.1.1 Fluctuation-Dissipation Theorem and Coating Thermal Noise

The FDT was first formalized by Callen *et al.* in the early 1950s [71–74]. Imagine a linear system that is in thermodynamic equilibrium. Such a system can have its equation of motion in the frequency domain written in terms of the amplitude of an external force $F_{\text{ext}}(f)$ which causes the system to move with a sinusoidal velocity of amplitude $v(f)$ in the following simple way,

$$F_{\text{ext}} = Z(f)v. \quad (2.55)$$

Equivalently, one can rearrange the above

$$v = Y(f)F_{\text{ext}}. \quad (2.56)$$

$Z(f)$ is the system's impedance, while $Y(f) = Z^{-1}$ is the system's admittance. The FDT states that the power spectrum $F_{\text{therm}}^2(f)$ of the minimal fluctuating force on a system is [71–74]

$$F_{\text{therm}}^2 = 4k_B T \mathcal{R}(Z(f)) \quad (2.57)$$

where $\mathcal{R}(Z)$ is the real or dissipative part of the impedance [42]. The power spectrum of such a system is then easy to derive,

$$S_x(f) = \frac{k_B T}{\pi^2 f^2} \mathcal{R}(Y(f)). \quad (2.58)$$

Thus for the first time, one was not required to create a detailed microscopic model of any dissipative phenomenon in order to characterize the fluctuation caused by it. The only requirement is a macroscopic mechanical model describing the impedance as a function of frequency. It should be noted that, while empirically descriptive, the FDT did not describe the underlying fundamental physics of the systems it was applied to. However, the FDT did formalize a known commonality amongst all systems that dissipate; noise away from resonances is reduced by reducing dissipation. In the test masses, this means that materials with reduced internal friction will have lower thermal noise [75].

Although the formulation of the FDT was a major milestone in thermodynamics and statistical mechanics, for this discussion it is more relevant to directly apply it to the problem of internal friction inside the test masses. The derivation herein follows the work of Levin [76]. Consider a Gaussian laser incident on the face of a test mass. As was discussed in Chapter 1, the phase shift of the reflected light contains information about the displacement of the face of the test mass. The power read out from this process can be generalized as

$$x(t) = \int f(\vec{r}) y(\vec{r}, t) d^2 r. \quad (2.59)$$

In the above, \vec{r} is a location on the test mass surface, and so is constrained to two dimensions. Conversely, $y(\vec{r}, t)$ is the deviation of the boundary along the direction of the laser beam at point \vec{r} and time t on the test mass surface. Lastly, $f(\vec{r})$ is the form factor and depends on the laser beam profile incident on the test mass. It is proportional to the light intensity at point \vec{r} and it is normalized such that

$\int f(\vec{r})d^2r = 1$. $f(\vec{r})$ is not a force, and one should be careful to not confuse it as one. [77].

The thermal noise of such a system is defined by the fluctuations in $x(t)$, and the goal is to define the spectral density $S_x(f)$ of these fluctuations. It is assumed that the system is in thermal equilibrium at temperature T . Via the FDT, the form of $S_x(f)$ is explicitly given by equation 2.58. In order to evaluate the equation in any quantitative way, the complex admittance $Y(f)$ must be calculated. One can introduce a special set of generalized coordinates for the test mass degrees of freedom, of which $x(t)$ is one. A generalized force that drives the momenta conjugate to x , but none of the other momenta, shows up in the Hamiltonian as the following interaction term

$$H_{int} = -F(t)x(t). \quad (2.60)$$

The time evolution of $x(t)$ will be determined by this driving force, the test mass internal elastic forces, and internal dissipation. If the Fourier transforms of the generalized force and coordinates are denoted $F(f)$ and $x(f)$ respectively, then the admittance of equation 2.58 is

$$Y(f) = 2\pi i f \frac{x(f)}{F(f)}. \quad (2.61)$$

The driving force $F(t)$ can be calculated by substituting the definition of the observable $x(t)$ of equation 2.59 into the interaction Hamiltonian of equation 2.60,

$$H_{int} = - \int P(\vec{r}, t) y(\vec{r}, t) d^2r. \quad (2.62)$$

In the above, $P(\vec{r}, t) = F(t)f(\vec{r})$. From equation 2.62 it is made clear that the generalized force $F(t)$ is the result of a pressure on the test mass surface. Conveniently, one can impose the constraint that the pressure is spatially distributed the same way as the beam intensity profile incident on the test mass surface.

As shown in equation 2.58, the real part of the admittance $Y(f)$ encodes the coupling of the test mass dissipation to the observable $x(t)$. Applying an oscillatory pressure $P(\vec{r}, t) = F_0 \cos(2\pi f t) f(\vec{r})$ to the test mass face demonstrates this coupling through the admittance. From equation 2.61 it can be inferred that the power W_{diss}

that the oscillatory pressure imparts into the test mass is given by

$$\text{Re}[Y(f)] = \pi f \frac{4W_{\text{diss}}}{F_0^2}. \quad (2.63)$$

This can be placed directly into equation 2.58 to yield

$$S_x(f) = \frac{4k_B T}{\pi^2 f^2} \frac{W_{\text{diss}}}{F_0^2}. \quad (2.64)$$

Although this is a powerful result unto itself, one cannot help but feel as if the ambiguous quantity of $\mathcal{R}(Y)$ has simply been swept under the rug of W_{diss} . However, as the initial equation of 2.58 evolved into equation 2.64 under specialization, the same can be done again to find a quantitative expression for W_{diss} .

In the scenario of homogeneously distributed damping, as one would expect from a structurally homogeneous test mass, the friction can be characterized by an imaginary part of the material's Young's modulus,

$$E = E_0[1 + i\phi(f)]. \quad (2.65)$$

$\phi(f)$ is the loss angle of a material, and it will be a critically important quantity in the coming sections and chapters of this thesis. Before going further, it is important to explore the concept of a loss angle, a unitless quantity that details how much a process or phenomenon will dissipate energy.

Any elastic body under an external stress, ϵ , will experience a restoring force opposing the external stress. These two forces, the external and the restoring, are related by Hooke's Law [78]. The strain on the elastic body is then given by the Young's Modulus, E , and the magnitude of the external stress,

$$\varepsilon = \frac{\epsilon}{E}. \quad (2.66)$$

A perfectly elastic body will respond instantly to the applied force, but real world materials have a delayed response. The magnitude of this delay determines how

anelastic a material is, with more anelastic bodies having a greater delay [79]. Assuming the external stress is periodic, it can be written in the following way

$$\epsilon = \epsilon_0 e^{i\omega t} \quad (2.67)$$

where the periodicity is defined by the angular frequency ω . The strain takes on a very similar periodic form, but with an added phase term due to the anelasticity of the material,

$$\varepsilon = \varepsilon_0 e^{i\omega t - i\phi}. \quad (2.68)$$

This phase lag between the external force and the strain is the mechanical loss angle, $\phi(\omega)_{\text{mech}}$. This internal friction is directly related to the magnitude of thermal noise present in a material. Any changes to or imperfections in the internal structure of a material can change the internal friction, and the loss. Grain boundaries, dangling bonds, and imperfections in glass structure all lead to higher loss [80, 81], while temperature change, heat treatment, and doping can raise or lower internal friction [59, 82–84].

One can use the loss angle to quantify W_{diss} as

$$W_{\text{diss}} = 2\pi f U_{\text{max}} \phi(f) \quad (2.69)$$

where U_{max} is the energy of elastic deformation at the moment where the test mass is maximally extended or contracted under the oscillatory pressure of equation 2.62.

The detection frequencies of the current generation gravitational wave detectors, characterized by the “bucket” of lower noise in Figure 8 centered on 200 Hz, are much lower than the normal modes of the detector test masses, the lowest of which is about 6 kHz. Therefore, when evaluating U_{max} one can assume a constant and non-oscillating pressure $P(\vec{r}) = F_0 f(\vec{r})$. Constraining the beam profile to be a Gaussian centered on the midpoint of the transverse coordinates yields the following,

$$f(\vec{r}) = \frac{1}{\pi r_0^2} e^{-r^2/r_0^2}. \quad (2.70)$$

Note that r_0 is the radius of the laser beam. If the laser beam spot is much smaller than the test mass face, the test mass can be approximated as an infinite elastic

half-space. In this approximation, the result can be assumed to be accurate up to a fractional accuracy of $O(r_0/R)$.

Given that $y(\vec{r})$ is the normal displacement of the surface at location \vec{r} caused by the pressure $P(\vec{r})$, in the linear approximation of small strains $y(\vec{r})$ is given by

$$y(\vec{r}) = \int G(\vec{r}, \vec{r}') P(\vec{r}') d^2 r' \quad (2.71)$$

where $G(\vec{r}, \vec{r}')$ is a Green's function. Quantifying G is a standard but nontrivial exercise in elasticity theory, and so it is expedient to take its solution from Landau [85],

$$G(\vec{r}, \vec{r}') = \frac{1 - \sigma^2}{\pi E_0} \frac{1}{|\vec{r} - \vec{r}'|}. \quad (2.72)$$

In the above expression, σ and E_0 are the Poisson ratio and the Young's modulus of the material. The elastic energy stored in the material when maximally compressed or extended is given by

$$\begin{aligned} U_{\max} &= \frac{1}{2} \int P(\vec{r}) y(\vec{r}) d^2 r = \frac{1}{2} \frac{1 - \sigma^2}{\pi E_0} \int \frac{P(\vec{r}) P(\vec{r}')}{|\vec{r} - \vec{r}'|} d^2 r d^2 r' \\ &= \frac{1}{2} \frac{1 - \sigma^2}{\pi^3 E_0 r_0^4} F_0^2 \int \frac{e^{-(r^2 + r'^2)/r_0^2}}{\sqrt{r^2 + r'^2 - 2rr' \cos(\theta)}} d^2 r d^2 r' \end{aligned} \quad (2.73)$$

where θ is the angle between \vec{r} and \vec{r}' . The final integral of equation 2.73 can be evaluated by introducing polar coordinates R and ϕ where $r = R \cos \phi$ and $r' = R \sin \phi$. The radial part of the integrand can be integrated out, and remaining angular part can be expanded in a power series with respect to $\cos(\theta)$. Integration of this power series yields a quantitative equation for U_{\max} up to a fractional error of $O(r_0/R)$,

$$U_{\max} = \frac{F_0^2}{\pi^2 E_0 r_0} (1 - \sigma^2) I \quad (2.74)$$

$$I = \frac{\pi^{3/2}}{4} \left[1 + \sum_{n=1}^{\infty} \frac{(4n-1)!!}{(2n)! 4^n (2n+1)} \right] \simeq 1.87322. \quad (2.75)$$

Substituting equation 2.74 into equation 2.69 and then that expression into equation 2.64 finally yields a tractable expression for thermal noise,

$$S_x(f) = \frac{4k_B T}{f} \frac{1 - \sigma^2}{\pi^3 E_0 r_0} I \phi. \quad (2.76)$$

Equation 2.76 is perhaps the most important equation of this work, as it fully characterizes the impact thermal noise has on the detector. Once one knows the Young's Modulus E_0 , Poisson ratio σ , and the loss angle ϕ of a material, it is possible to rigorously predict the thermal noise present in test masses made of such a material using equation 2.76 [76].

2.1.2 Loss Angle of a Test Mass Coating

Although equation 2.76 is useful for assessing the loss due to the bulk of the test masses, it is insufficient to describe the loss associated with a coated test mass. The ϕ of equation 2.76 is composed of the constituent loss sources in a material; for a coated test mass this can be broken down into the loss from the coating and the loss from the bulk substrate. Since the test masses must act as a mirror in the interferometer, they require mirror coatings. Unfortunately, these mirror coatings typically have higher mechanical loss and thus higher thermal noise [86, 87]. The reasons that the test mass must be coated with another material that is, generally, of higher loss as compared to the bulk will be explored in detail in section 2.2.1.

An Early Derivation of Coating Loss Angle

When one considers the thermal loss due to a bulk material with a thin layer of high loss material coated on the exterior, it becomes impossible to describe the full system with one number. One needs to know the individual losses of all materials involved and, importantly, the relative distribution of energy in each material. Therefore, in order to map the loss of materials in an experiment to how it will effect the noise in a gravitational wave detector, it is necessary to disentangle the loss due to the substrate and the loss due to the coating. It would be ideal to simply manufacture coated test masses and get a direct measurement of the loss, but that would waste too much time, money, and material to be feasible. The experimental techniques used to measure material loss will be explored in Chapter 3.

The following derivation will follow the work of Harry *et al.* [88]. Instead of defining the loss of the system as simply ϕ , it can be helpful to define it as a loss that is readout by the experiment $\phi \equiv \phi_{\text{readout}}$. This readout loss can be written as a weighted sum of the substrate loss and the coating loss. Assuming the loss of the coating is isotropic and homogeneous, an assumption that will be dropped later, one can write the weighted sum quite simply,

$$\phi_{\text{readout}} = \frac{1}{U} (U_{\text{substrate}} \phi_{\text{substrate}} + U_{\text{coating}} \phi_{\text{coating}}). \quad (2.77)$$

U is the maximum elastic energy stored in the system as a result of the Gaussian pressure distribution, $U_{\text{substrate}}$ is the energy in the substrate, U_{coating} is the energy in the coating, $\phi_{\text{substrate}}$ is the loss of the substrate, and ϕ_{coating} is the loss of the coating.

Since the coating is very thin compared to the size of the pressure distribution and the substrate, the coating energy can be approximated as

$$U_{\text{coating}} = \delta U d \quad (2.78)$$

where δU is the energy density stored at the surface and d is the coating thickness. Another ramification of the small coating thickness is that $U_{\text{substrate}}$ can be approximated as holding all the energy U , and therefore

$$\phi_{\text{readout}} = \phi_{\text{substrate}} + \frac{\delta U d}{U} \phi_{\text{coating}} \quad (2.79)$$

To account for possible anisotropy, it is necessary to ascribe a loss angle to each energy density term of a cyclically deformed material. The following two orthogonal energy density components can encapsulate the entirety of the loss:

$$\begin{aligned} \rho'_{U\parallel} &= \frac{1}{2} (\epsilon'_{rr} \sigma'_{rr} + \epsilon'_{\theta\theta} \sigma'_{\theta\theta} + \epsilon'_{r\theta} \sigma'_{r\theta}) \\ \rho'_{U\perp} &= \frac{1}{2} \epsilon'_{zz} \sigma'_{zz} \end{aligned} \quad (2.80)$$

where ϵ'_{ij} and σ'_{ij} are the strains and stresses in the coating, respectively. The loss angles associated with the two energy density components, $\rho'_{U\parallel}$ and $\rho'_{U\perp}$, are ϕ_{\parallel} and ϕ_{\perp} .

Bulk and Shear Decomposition: Deformation of the Test Mass Surface

Although the style of decomposing the elastic energy into parallel and perpendicular components was popular in the field for the next decade, in 2013 Hong *et al* [17] found it was more useful to disentangle them into bulk and shear components. In a high reflectivity (HR) stack, there will be many layers of alternating high index and low index of refraction coatings. Assuming the coating layers are isotropic, they are completely characterized by their complex bulk and shear moduli, which can be written as

$$\begin{aligned}\tilde{K} &= K(1 + i\phi_B) \\ \tilde{\mu} &= \mu(1 + i\phi_S)\end{aligned}\tag{2.81}$$

where K and μ are the much larger real parts of the bulk and shear moduli, respectively.

Brownian thermal fluctuations of a coating can be divided into three phenomena: thickness fluctuation of the coatings, fluctuation at the coating-substrate interface, and coating refractive index fluctuations associated with longitudinal/thickness and transverse/area elastic deformations. Note that this ignores thermoelastic and thermo-refractive loss mechanisms; the focus is on mechanical loss. Consider a laser field normally incident along the negative z direction onto a coated test mass. It has a complex amplitude field of $u_{\text{in}}(x, y)$ at a fixed reference plane and intensity profile $I(x, y) = |u_{\text{in}}(x, y)|^2$. Note that, for the remainder of this derivation, \vec{x} will be used to represent the two-dimensional vector (x, y) in the transverse plane and boldface letters \boldsymbol{x} will be used to represent three dimensional vectors. Although this notation can be confusing, it is used by Hong *et al* [17] and is acceptable due to the extremely limited usefulness of \boldsymbol{x} .

Since the beamspot is much larger than the coating thickness, the reflected field at \vec{x} will have an amplitude given by

$$u_{\text{out}}(\vec{x}) = \rho_{\text{tot}}(\vec{x})u_{\text{in}}(\vec{x}).\tag{2.82}$$

This only depends on complex reflectivity $\rho_{\text{tot}}(\vec{x})$ and the incident field. One can

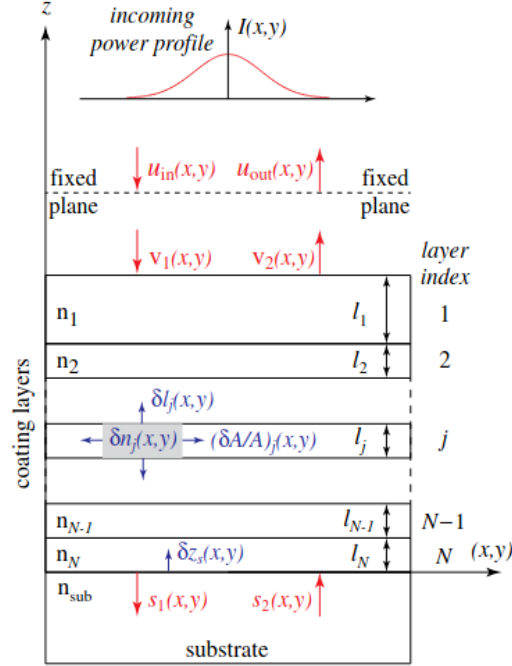


Figure 9 : Depicted above is a drawing of a multilayer coated test mass. The various fluctuations that contribute to coating noise are also pictured: $\delta z_s(\vec{x})$, $\delta l_j(\vec{x})$, $\delta A_j/A_j$ and $\delta n_j(\vec{x})$. Image credit to Hong [17].

further divide $\rho_{tot}(\vec{x})$ into three factors,

$$\rho_{tot}(\vec{x}) = \frac{u_{out}(\vec{x})}{u_{in}(\vec{x})} = \left[\frac{u_{out}(\vec{x})}{\nu_2(\vec{x})} \right] \left[\frac{\nu_1(\vec{x})}{u_{in}(\vec{x})} \right] \left[\frac{\nu_2(\vec{x})}{\nu_1(\vec{x})} \right]. \quad (2.83)$$

$\nu_1(\vec{x})$ and $\nu_2(\vec{x})$ are the incident and reflected complex amplitude at the coating-air interface, respectively.

The first two factors on the right side of equation 2.83 are caused by the light traveling from the reference plane to the coating-air interface. Up to a constant phase factor, these two terms can be rewritten as

$$\left[\frac{u_{out}(\vec{x})}{\nu_2(\vec{x})} \right] \left[\frac{\nu_1(\vec{x})}{u_{in}(\vec{x})} \right] = e^{-2ik_0[\delta z_s(\vec{x}) + \sum_{j=1}^N \delta l_j(\vec{x})]} \quad (2.84)$$

where $k_0 = \omega_0/c$ is the wave number of the laser in vacuum, $\delta z_s(\vec{x})$ is the vertical displacement of the coating-substrate interface from its zero point, and $\delta l_j(\vec{x})$ is the thickness fluctuation of the j th coating layer. Note that $\delta z_s(\vec{x})$ and $\delta l_j(\vec{x})$ are functions

of the transverse location \vec{x} .

The last term of equation 2.83 is a function of the phase shift experienced by the field in each layer and the reflectivity at each interface. Therefore, ν_2/ν_1 can be rewritten,

$$\frac{\nu_2(\vec{x})}{\nu_1(\vec{x})} = \rho[\tau_1(\vec{x}), \dots, \tau_N(\vec{x}); r_1(\vec{x}), \dots, r_{N+1}(\vec{x})]. \quad (2.85)$$

It is important to note that τ_j represents the optical thickness of the j th coating, and is not a characteristic time. Additionally, ρ represents the complex reflectivity of the entire multilayer stack at the coating-air interface (not to be confused with ρ_{tot} which is the complex reflectivity of the incident field) while r_j represents the reflectivity of the j th interface, where r_{N+1} is the substrate-air interface on the opposite side of the test mass.

Once the above equations 2.83, 2.84, and 2.85 are combined, the result is as follows:

$$\rho_{tot}(\vec{x}) = e^{-2ik_0[\delta z_s(\vec{x}) + \sum_{j=1}^N \delta l_j(\vec{x})]} \rho[\{\tau_j(\vec{x})\}; \{r_p(\vec{x})\}] \quad (2.86)$$

Brownian thermal forces induce fluctuations in both the real and imaginary parts of the complex reflectivity. Sensing noise is created by phase modulation of the outgoing field, as seen in the argument of the complex reflectivity. Furthermore, a ponderomotive force noise is created by amplitude modulation of the outgoing field, caused by fluctuations in the magnitude.

The amplitude and phase fluctuations of the reflected light at position \vec{x} on the test mass surface can be encoded in the real and imaginary parts of the derivative of the log of the complex reflectivity,

$$\delta \log \rho_{tot}(\vec{x}) = \frac{\delta \rho_{tot}(\vec{x})}{\rho_{tot}(\vec{x})}. \quad (2.87)$$

Amplitude fluctuation can equivalently be thought of as intensity fluctuation and quantified that way,

$$\frac{\delta I(\vec{x})}{I(\vec{x})} = 2 \frac{\delta |\rho_{tot}(\vec{x})|}{|\rho_{tot}(\vec{x})|} = 2 \text{Re}[\delta \log \rho_{tot}(\vec{x})]. \quad (2.88)$$

Phase fluctuation is given by

$$\delta\phi(\vec{x}) = \delta\arg[\rho_{\text{tot}}(\vec{x})] = \text{Im}[\delta\log\rho_{\text{tot}}(\vec{x})] \quad (2.89)$$

Therefore, it is possible to create our own functions of \vec{x} , ξ and ζ , that encapsulate phase and amplitude noise, respectively,

$$\xi(\vec{x}) - i\zeta(\vec{x}) = \frac{-i}{2k_0}\delta[\log\rho_{\text{tot}}]. \quad (2.90)$$

Note that ξ and ζ both have dimensionality of length. Using equation 2.89, the form of ξ can be quantified,

$$2k_0\xi(\vec{x}) = \delta\phi(\vec{x}). \quad (2.91)$$

Note that $\phi(\vec{x})$ is a phase, and not the coating loss angle in the above equation. As was discussed in chapter 1, the test mass position is measured via the phase shift of the reflected light through the relation $\Delta\phi = 2k_0\Delta z$. It then becomes obvious that ξ represents the displacement noise due to phase fluctuations in the reflected light caused by the coating. A similar process can be followed for ζ ,

$$2k_0\zeta(\vec{x}) = \text{Re}[\delta\log\rho_{\text{tot}}] = \frac{\delta I(\vec{x})}{2I(\vec{x})}. \quad (2.92)$$

This will cause a fluctuating force on the mirror, but the effect will be much smaller than that caused by ξ for gravitational wave detectors.

Now that the authenticity of ξ and ζ as representative of phase and amplitude noise has been proven, one can substitute equation 2.86 into the initial definition of ξ and ζ equation 2.90,

$$\begin{aligned} \xi(\vec{x}) - i\zeta(\vec{x}) = & -\delta z_s(\vec{x}) - \sum_{l=1}^N \delta l_j(\vec{x}) - \sum_{j=1}^N \frac{i}{2k_0} \left[\frac{\delta\log\rho}{\delta\tau_j} \delta\tau_j(\vec{x}) \right] \\ & - \sum_{p=1}^{N+1} \frac{i}{2k_0} \left[\frac{\delta\log\rho}{\delta r_p} \delta r_p(\vec{x}) \right]. \end{aligned} \quad (2.93)$$

The first term is due to the longitudinal motion of the coating-air interface at \vec{x} , while the second term represents thickness fluctuations of the coating layers. The third term is the sum of phase gained by the field as it propagates through the coating layers,

which is fluctuating layer to layer. The last term is the reflectivity of the p th interface, summed over all interfaces.

The origin of these fluctuations, $\delta\tau_j$ and δr_p , is not obvious. As light propagates inside the coating layers, it is subjected to the photoelastic effect. The material the light is passing through is subject to Brownian stresses, which cause an isothermal fluctuation in $\delta n_j(\mathbf{x})$,

$$\delta n_j(\mathbf{x}) = \beta_j^L S_{zz}(\mathbf{x}) + \beta_j^T [S_{xx}(\mathbf{x}) + S_{yy}(\mathbf{x})] \quad (2.94)$$

where

$$\beta_j^L \equiv \left(\frac{\partial n_j}{\partial \log l} \right)_{A_j} \quad \beta_j^T \equiv \left(\frac{\partial n_j}{\partial \log A} \right)_{l_j}. \quad (2.95)$$

In the above, L is short for longitudinal, while T is short for transverse. The subscripts A_j and l_j represent a fixing of transverse area and longitudinal length, respectively. S_{ij} is the expected definition of strain given by

$$S_{ij} \equiv \frac{1}{2} \left[\frac{\partial u_i}{\partial x_j} + \frac{\partial u_j}{\partial x_i} \right] \quad (2.96)$$

where $u_i(\mathbf{x})$, $i = 1, 2, 3$ are components of the displacement vector of the mass element at position \mathbf{x} .

Notice that in equation 2.94, $S_{xx} + S_{yy}$ represents the fractional increase in transverse area. When the beam spot size is much larger compared to the coating thickness, this term can safely be ignored. After dropping that term, β_j^L can be rewritten as simply β_j .

The remaining term of equation 2.94 causes both an additional phase shift and back scattering of the field penetrating the coating layers. These effects can be quantified by altering the phase shift of each layer $\delta\phi_j$ and the reflectivity δr_j ,

$$\delta\phi_j = k_0 \left[(n_j + \beta_j) \delta l_j - \frac{1 - r_j^2}{2r_j} \beta_j \delta l_j^c + \frac{1 + r_{j-1}^2}{2r_{j-1}} \beta_{j-1} \delta l_{j-1}^c \right] \quad (2.97)$$

$$\delta r_j = k_0 t_j^2 \beta_j \delta l_j^s. \quad (2.98)$$

It is important to note that the $\delta\phi_j$ in equation 2.97 does not represent loss angle in any way, but instead symbolizes a small phase change caused by a similarly tiny

fluctuation in optical thickness $\delta\tau_j$. To make the above equations more compact, the following expressions are contained within δl_j^c and δl_j^s ,

$$\begin{aligned}\delta l_j^c &\equiv - \int_0^{l_j} S_{zz}(z_{j+1} + z) \cos(2k_0 n_j z) dz \\ \delta l_j^s &\equiv - \int_0^{l_j} S_{zz}(z_{j+1} + z) \sin(2k_0 n_j z) dz.\end{aligned}\tag{2.99}$$

Note that when $j = 0$, then $\delta l_j^c = \delta l_j^s = 0$. Additionally, z_j represents the z coordinate of the j th layer and can be defined as

$$z_j \equiv \sum_{n=j}^N l_n.\tag{2.100}$$

After substituting equations 2.97 and 2.98 into equation 2.93, one will obtain

$$\xi(\vec{x}) - i\zeta(\vec{x}) = -z_s(\vec{x}) - \sum_{j=1}^N \int_{z_{j+1}}^{z_j} \left[1 + \frac{i\epsilon_j(z)}{2} \right] u_{zz}(\vec{x}, z) dz.\tag{2.101}$$

The new term $\epsilon_j(z)$ captures all effects associated with light penetration into the coating,

$$\begin{aligned}\epsilon_j(z) &= (n_j + \beta_j) \frac{\partial \log \rho}{\partial \phi_j} - \beta_j \left[\frac{1 - r_j^2}{2r_j} \frac{\partial \log \rho}{\partial \phi_j} - \frac{1 + r_j^2}{2r_j} \frac{\partial \log \rho}{\partial \phi_{j+1}} \right] \\ &\quad \times \cos[2k_0 n_j (z - z_j)] - t_j^2 \beta_j \frac{\partial \log \rho}{\partial r_j} \sin[2k_0 n_j (z - z_{j+1})].\end{aligned}\tag{2.102}$$

It is important to notice that the last term of the sum in equation 2.101 has a unique impact on $\epsilon_j(z)$. Since ϕ_{N+1} does not exist, the second half of the second term is zero for this last term alone.

Once again, it is possible to decompose the real and imaginary parts of the right-hand side of equation 2.101 to find individual expressions for ξ and ζ ,

$$\xi(\vec{x}) = -z_s(\vec{x}) - \sum_{j=1}^N [\mathcal{T}_j^\xi \delta l_j(\vec{x}) + \mathcal{T}_j^{\xi c} \delta l_j^c(\vec{x}) + \mathcal{T}_j^{\xi s} \delta l_j^s(\vec{x})]\tag{2.103}$$

$$\zeta(\vec{x}) = \sum_{j=1}^N [\mathcal{T}_j^\zeta \delta l_j(\vec{x}) + \mathcal{T}_j^{\zeta c} \delta l_j^c(\vec{x}) + \mathcal{T}_j^{\zeta s} \delta l_j^s(\vec{x})].\tag{2.104}$$

Note that the various \mathcal{T}_j^{ik} are transfer functions from the δ_j^i to a displacement equivalent thermal noise. See Hong [17] for the specific form of each transfer function.

In theory, the magnitude of ξ and ζ are comparable in a stack with an arbitrary number of layers. However, for the highly reflective stacks of the LVK test masses, the real part of $\partial \log \rho / \partial \phi_j$ and $\partial \log \rho / \partial r_j$ are much smaller than the imaginary part. Therefore, in practice, $\xi \gg \zeta$ which implies that amplitude fluctuations are much smaller than phase fluctuations.

Bulk and Shear Decomposition: Conversion to Sensed Displacement Noise

Up until this point, the fluctuations at each point on the test mass surface have been derived. However, the detector can only sense one displacement noise. Recall that the Fabry-Pérot cavity only resonates one optical mode; this mode has complex amplitude $u_0(\vec{x})$ incident on the test mass surface. The reflected field will take the form $u_{\text{out}}(\vec{x}) = \rho_{\text{tot}}(\vec{x})u_0(\vec{x})$, which contains other modes alongside the incident mode. These other modes will not resonate in the cavity. Picking out the part of the reflected field that resonates in the cavity yields the following expression for complex reflectivity:

$$\bar{\rho} = \frac{\int u_0^*(\vec{x})u_{\text{out}}(\vec{x})d^2\vec{x}}{\int u_0^*u_{\text{out}}d^2\vec{x}} = \frac{\int \rho_{\text{tot}}(\vec{x})I(\vec{x})d^2\vec{x}}{\int I(\vec{x})d^2\vec{x}}. \quad (2.105)$$

In the above, $I(\vec{x}) \equiv |u_0(\vec{x})|^2$ and $\bar{\rho}$ is averaged over the phase front. Using equations 2.90 and 2.105, one finds that

$$\frac{\delta \bar{\rho}}{\bar{\rho}} = 2ik_0(\bar{\xi} - i\bar{\zeta}) \quad (2.106)$$

$$\bar{\xi} \equiv \frac{\int \xi(\vec{x})I(\vec{x})d^2\vec{x}}{\int I(\vec{x})d^2\vec{x}} \quad \bar{\zeta} \equiv \frac{\int \zeta(\vec{x})I(\vec{x})d^2\vec{x}}{\int I(\vec{x})d^2\vec{x}}. \quad (2.107)$$

The phase change accumulated by the returning light is given by $2ik_0\bar{\xi}$. This effect is the same amount of phase change created by the mirror being displaced a distance of $\bar{\xi}$, and so mirror deformation translates directly to a displacement noise via $\bar{\xi}$. The amplitude noise $\bar{\zeta}$ is much smaller, and therefore not a significant source of noise.

Recall in section 2.1.1 the derivation of thermal noise through the Fluctuation-Dissipation Theorem yielded equation 2.64, but this can be rewritten as

$$S_x(f) = \frac{4k_B T}{\pi^2 f^2} \frac{W_{\text{diss}}}{F_0^2} = \frac{4k_B T}{\pi^2 f^2} \frac{U}{F_0^2} \phi \quad (2.108)$$

where ϕ is the loss angle defined by

$$\phi = \frac{\text{Re}[Z(f)]}{\text{Im}[Z(f)]}. \quad (2.109)$$

Note that $Z(f)$ is the mechanical impedance from equation 2.55 at the beginning of this chapter.

The thermal noise due to the fluctuation of the coating-air interface position can be obtained by using equation 2.108, but it can also be found by applying a pressure profile proportional to $I(\vec{x})$ to the mirror surface. Here we can separate elastic energy into bulk and shear components via [85]

$$U_{\text{coating}} = U_B + U_S = \int_{\text{coating}} \left(\frac{K}{2} \Theta^2 + \mu \Sigma_{ij} \Sigma_{ij} \right) dV \quad (2.110)$$

where Θ is the expansion, and Σ_{ij} is the shear tensor. The imaginary parts of the bulk and shear moduli from equation 2.81 allow us to write the dissipated energy in the coating as

$$W_{\text{diss}} = \phi_B U_B + \phi_S U_S. \quad (2.111)$$

Due to the much lower loss in the substrate, equation 2.111 serves as an accurate expression for dissipated energy in the entire system, not just the coating.

However, in order to be totally accurate, the interface between coating and substrate must also be properly accounted for. In the derivation, Hong formalizes the effect the bulk and shear deformations have on the substrate and coating. Bulk deformations of the coating layer alter the thickness of the coating, altering the position of the coating-air interface. Shear deformations of the coating layer do not alter thickness, but are a shape change that causes the coating to contract with respect to the coating-substrate interface. Starting from a pressure profile described by the following

$$f(\vec{x}) = F_0 w(\vec{x}) \quad (2.112)$$

where $w(\vec{x})$ represents the normalized intensity profile of the beam, the form of the normalized energy for the bulk and shear parts is shown to be

$$\frac{U_B}{F_0^2} = \frac{(1-2\sigma_c)l}{3} \left[\frac{Y_c}{Y_s^2} \frac{(1-2\sigma_s)^2(1+\sigma_s)^2}{(1-\sigma_c)^2} + \frac{1}{Y_s} \frac{2(1-2\sigma_s)(1+\sigma_s)(1+\sigma_c)}{(1-\sigma_c)^2} \right. \\ \left. + \frac{1}{Y_c} \frac{(1+\sigma_c)^2}{(1-\sigma_c)^2} \right] \int w^2(\vec{x}) d^2\vec{x} \quad (2.113)$$

$$\frac{U_S}{F_0^2} = \frac{2l}{3} \left[\frac{Y_c}{Y_s^2} \frac{(1-\sigma_c+\sigma_c^2)(1+\sigma_s)^2(1-2\sigma_s)^2}{(1-\sigma_c)^2(1+\sigma_c)} - \frac{1}{Y_s} \frac{(1+\sigma_c)(1-2\sigma_c)(1-2\sigma_s)(1+\sigma_s)}{(1-\sigma_c)^2} \right. \\ \left. + \frac{1}{Y_c} \frac{(1-2\sigma_c)^2(1+\sigma_c)}{(1-\sigma_c)^2} \right] \int w^2(\vec{x}) d^2\vec{x} \quad (2.114)$$

where l is the coating thickness, and the subscripts s and c stand for the substrate and coating respectively. Note that

$$\int w^2(\vec{x}) d^2\vec{x} \equiv \frac{1}{\mathcal{A}_{\text{eff}}} \quad (2.115)$$

where \mathcal{A}_{eff} is the effective beam area.

The importance of the above equations become clear when we seek the form of the thermal noise that accounts for different bulk and shear losses. By substituting the form of dissipated energy from equation 2.111 into equation 2.108, the following noise spectrum emerges,

$$S_{\xi} = \frac{4k_b T}{\pi f} \left[\phi_B \frac{U_B}{F_0^2} + \phi_S \frac{U_S}{F_0^2} \right]. \quad (2.116)$$

Although this derivation does not account for light penetration into the coating, neither had previous derivations. Furthermore, compared to the previous work done by Harry *et al* [88] and others, Hong's work demonstrated that coating thermal noise was being underestimated.

However, an accurate analysis of the coating thermal noise for a detector test mass is a little more complex than this. The reasons for this will be explored in detail in section 2.2.1, but for now it is sufficient to know that the test mass has strict requirements on optical properties such as index of refraction, scatter, reflectivity, and absorption. No single layer coating is going to meet the requirements imposed on

the detector, but an alternating highly reflective (HR) stack of alternating layers of coatings does. The most current aLIGO test masses use a stack of alternating titania doped tantala ($\text{Ti:Ta}_2\text{O}_5$) and silica.

Hong [17], who we have followed for the derivation of bulk and shear contributions to the thermal noise power spectral density in equation 2.108, goes on to account for light penetration in a multi-layer stack. Although this work is lauded in the coatings community, in order for it to be useful one must know the bulk and shear loss contributions independently, not their collective total loss. Quantifying these loss angles separately from ringdown measurements has not yet been rigorously formalized, but it has been accomplished to a satisfactory degree [19, 89, 90] by fitting the loss of multiple modes. This is explored more in section 5.3.1.

Yam *et al* [89] simplified this calculation by assuming that, roughly, $\phi_{shear} \equiv \phi_{bulk}$. Although this defeats the purpose of the bulk and shear decomposition, it does simplify the calculation of the thermal noise power spectrum. In this regime, the expression for thermal noise is given by

$$S_z^{Br} = \frac{4k_B T}{\pi r_G^2 \omega} \frac{1 - \sigma_s - 2\sigma_s^2}{Y_s} \sum_j b_j d_j \phi_{Mj} \quad (2.117)$$

where k_B is the Boltzmann constant, T is the temperature of the mirror, $r_G \approx 6$ cm is the Gaussian beam radius, ω is the angular frequency, σ_s is the Poisson ratio of the substrate, Y_s is the Young's Modulus of the substrate, b_j is a unitless weighting factor, d_j is the coating thickness of the j th layer, ϕ_{Mj} is the mechanical loss of the j th layer. The weighting factor, b_j , is

$$b_j = \frac{1}{1 - \sigma_j} \left[\left(1 - n_j \frac{\partial \phi_c}{\partial \phi_j} \right)^2 \frac{Y_s}{Y_j} + \frac{(1 - \sigma_s - 2\sigma_s^2)^2}{(1 + \sigma_j)^2 (1 - 2\sigma_j)} \frac{Y_j}{Y_s} \right] \quad (2.118)$$

where n_j in the above equation denotes the index of refraction for the j th layer.

The weighting factor of equation 2.118 accounts for two phenomena in the coating stack that are sources of phase noise. As was discussed earlier in this chapter, the test mass coating layers will expand and contract, altering the position of the coating-air interface that the carrier beam will reflect off of. This is accounted for by scaling the noise via the ratio of the substrate's and coating's Young's Moduli for each coating layer. There is also an additional effect from the interplay of the coating-substrate

interface. This is accounted for by the second term involving the Poisson ratios of the substrate and the layers, scaled by the reverse ratio of the Young's moduli. This weighting factor is then further influenced in equation 2.117 by the thickness d_j and the mechanical loss ϕ_j of the j th layer.

2.1.3 Thermoelastic Dissipation

Thermoelastic Dissipation, also referred to as TED or thermoelastic loss, is a loss source intrinsic to all materials. As an object is deformed, there will be locations in the material where it is being either stretched or compressed. These local contortions cause that small portion of the object to heat up or cool down, depending on the nature of the local stress and the material properties. All of these local temperature gradients caused by the macroscopic deformation of the object cause irreversible heat flows, the direction of which are highly dependent on the geometry of the object and the deformation. Figure 10 is an example of this phenomenon in a bent beam. The first person to craft a theory for this phenomenon was Zener in 1937 [91].

Since TED results from the creation of a heat flow due to elastic stresses and strains, the level of TED present in a material is determined by the coupling between the temperature and strain gradients via the coefficient of thermal expansion,

$$\rho \frac{\partial^2 u}{\partial t^2} = Y \frac{\partial^2 u}{\partial x^2} + \frac{\alpha Y}{1 - 2\sigma} \frac{\partial T}{\partial x} \quad (2.119)$$

$$c\rho \frac{\partial T}{\partial t} = \kappa \frac{\partial^2 T}{\partial x^2} - \frac{\alpha Y T_0}{1 - 2\sigma} \frac{\partial}{\partial x} \frac{\partial u}{\partial t}. \quad (2.120)$$

Note that u is the displacement, Y is the Young's Modulus, σ is the Poisson ratio, c is the heat capacity, T is the temperature at a given point x , T_0 is the average temperature, κ is the thermal conductivity, ρ is the density, and α is the coefficient of thermal expansion, often referred to as CTE. The importance of the CTE to this phenomenon is demonstrated by the second term on the right side of both equations 2.119 and 2.120; if CTE vanishes, so too does the coupling and TED completely disappears.

Applying the above equations 2.119 and 2.120 to the beam depicted in Figure 10, one can determine that the CTE in the beam is positive. In this case, compressive strain will lead to a temperature increase, while tensile strain will lead to a

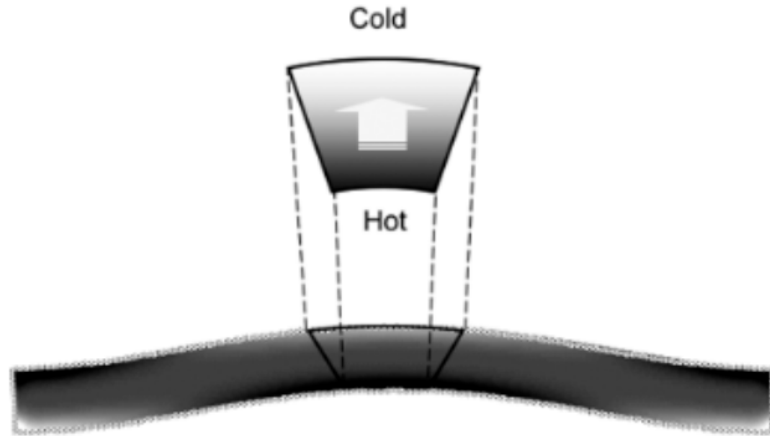


Figure 10 : A model of TE Dissipation in a bent beam. Darker areas are hotter, while lighter areas are colder. Notice how the locations where the material is being compressed heat up, while the opposite is true where the material is being stretched. In the center, this causes a local heat flow from the bottom of the bar to the top, shown by the arrow in the cut-out. Credit for this image to Candler [18].

temperature decrease. For a material with a negative CTE but the same geometry, the opposite temperature gradient would be created under the same applied strain. Energy dissipation results from the strain gradients inducing temperature gradients, driving irreversible heat flows. Therefore, any object that is subject to a large strain gradient will have prominent TED, except in the exceptionally rare case when the CTE is negligible or zero [92].

Thermoelastic Dissipation in a Thin Disk

To quantify the TED in an object, one must solve the coupled equations 2.119 and 2.120. The geometry of the object heavily dictates the form of the solution, so an expression for TED that works for a beam would not work for a butterfly resonator nor would it be adequate for a disk resonator. This work will quantify the TED of a silicon thin disk resonator, then further complicate the problem by finding the TED of the same resonator coated in a different material a few micrometers thick. The reason for this is made clear in chapter 3, but for now it will be justified simply by stating that these are the types of resonators used in this work to measure thermal noise of possible future test mass coatings.

Following the work of Cagnoli [19] with a correction by Tait [59], for a thin disk

the loss due to TED is given by

$$\phi_{\text{TED}} = \mathcal{D} \frac{(3\alpha)^2 K T_0}{\rho c_V} \frac{\omega \omega_{\text{peak}}}{\omega^2 + \omega_{\text{peak}}^2} \quad (2.121)$$

where K is the bulk modulus, c_V is the heat capacity at constant volume, $\omega = 2\pi f$ is the angular frequency, ρ is the density, \mathcal{D} is a geometric factor, and ω_{peak} , the angular frequency of the Debye peak, is given by

$$\omega_{\text{peak}} = \frac{\kappa}{\rho c_V} \left(\frac{\pi}{L} \right)^2. \quad (2.122)$$

Note that ϕ_{TED} is maximized when, holding all else equal, $\omega = \omega_{\text{peak}}$. In the above expression, κ is the thermal conductivity and L is the thickness of the disk, which is 500 μm for this work. The importance of ω_{peak} can be physically justified by considering heat flows in an object resonating with angular frequency ω . If the heat flows too quickly, $\omega \ll \omega_{\text{peak}}$, whatever temperature gradient is generated by the deformation will equilibrate long before the object can drive further heat flows. If the heat flows too slowly, $\omega \gg \omega_{\text{peak}}$, the temperature gradient induced by the object's oscillation will not change before the strain field flips. This causes the old temperature field to be canceled by that of the opposite strain field; heat cannot significantly flow.

The geometric factor is a ratio between the pure dilatation energy and the total elastic energy. It tells the user the proportion of the total elastic energy that is present in a certain mode or deformation shape, and as such holds all the geometric information of a certain applied strain. Following a derivation of Li [93], the geometric factor \mathcal{D} for a thin cylinder is given by

$$\mathcal{D} = \frac{(1 + \sigma)(1 - 2\sigma)}{3(1 - \sigma)} \frac{\int \int (W_{xx} + W_{yy})^2 dx dy}{\int \int [(W_{xx} + W_{yy})^2 - 2(1 - \sigma)(W_{xx}W_{yy} - W_{xy}^2)] dx dy}, \quad (2.123)$$

where σ is the Poisson ratio of the material and the $W_{ii}(x, y)$ are the deformed shape of the membrane. This geometric factor is often referred to as a dilution factor, however the name is altered here since the term is used copiously later in relation to energies present in the coating.

The nature of the geometric factor and its relationship to the different resonant modes in thin disk resonators will be explored in section 3.3.1. For now, it is sufficient

to follow Cagnoli [19], who uses finite element analysis (FEA) to determine the value of \mathcal{D} for crystalline silicon thin disk resonators, the same substrate material that was used in the experiment that is the focus of this thesis. For more context on the motivation of crystalline silicon as a substrate, see section 4.1.

The astute reader will notice the severe dependence equation 2.121 has on temperature. Not only is there the linear scaling of T_0 , but α , c_V , and κ all change with temperature as well. Technically, the bulk modulus K also has a dependence on temperature. However, the work of Liu [11] shows that the change is so small in the temperature range relevant to the experiment that one can ignore it and still get an accurate calculation of TED. The value for K used to calculate the TED in the silicon resonators is given in the caption of Table 1, which contains the values of the rest of the temperature dependent constants used in this analysis.

Table 1 : A table detailing all the constants for crystalline silicon at a given temperature for the TE loss analysis. The value of Bulk Modulus K was held fixed at 100 GPa. See Liu [11] for the justification of fixing K .

Thermal Constant	Temperature						
	12 K	20 K	50 K	100 K	122 K	200 K	300 K
$\alpha[\text{K}^{-1}]$ [94]	1.3e-9	-2.7e-9	-3.0e-7	-3.3e-7	-5.0e-8	1.4e-6	2.6e-6
$\kappa[\text{W/m/K}]$ [95]	1800	3000	2600	950	580	266	156
$c_V[\text{J/kg/K}]$ [96]	0.20	1.0	3.0	8.5	10.	17	22.5

Figure 11 shows the TED loss angle and the measured loss angle at specific temperatures of two 4 inch diameter thin disk silicon resonators for all the measured normal modes of the disk. It is important to note that the measured loss angle is the sum of all dissipative mechanisms in the system, as explored in section 2.1.1, of which TED is just one dissipative phenomenon. From Rodriguez [92],

$$\phi_{total} = \frac{1}{2\pi} \frac{\text{Energy dissipated per cycle}}{\text{Energy stored in the system}} \quad (2.124)$$

$$\phi_{total} = \sum_i \phi_i = \phi_{\text{mech}} + \phi_{\text{TE}} + \phi_{\text{gas}} + \phi_{\text{support}} + \phi_{\text{other}} \quad (2.125)$$

one can see some of the different loss phenomena present in the system. Chapter 3 and the results presented in chapter 4 will provide evidence that the substrate loss sources besides ϕ_{mech} and ϕ_{TE} are generally negligible, and go into detail about the

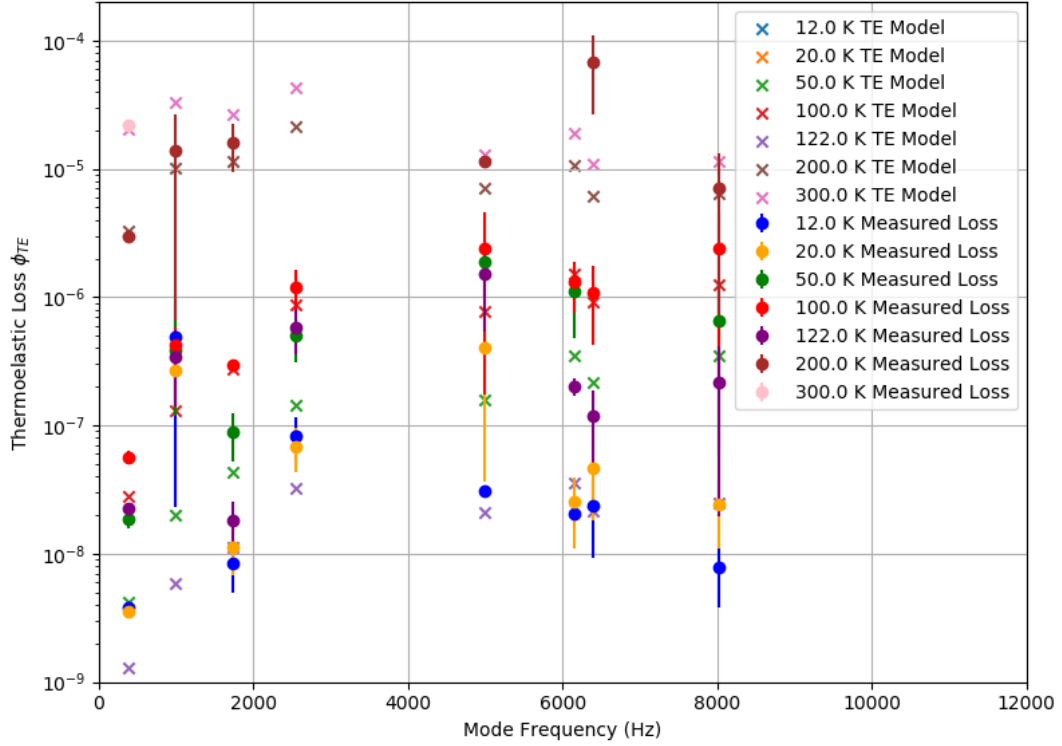


Figure 11 : Theoretical thermoelastic loss of 4 inch diameter bare silicon disk normal modes with disk thickness of $500\ \mu\text{m}$ at various temperatures from 12 K to 300 K, plotted with the measured loss for those modes. Refer to Figure 12 to see the data at each mode individually. The data marked with an \times are modeled, while the solid circles were measured in the Cryogenic Gentle Nodal Suspension, see chapters 3 and 4. Any measured data without error bars is due to the error bars being too small to see. The measured loss is dominated by TED at 100 K, 200 K, and 300 K. The importance of the coefficient of thermal expansion is demonstrated by the large drop in TE loss at 122 K, where it is near a zero crossing point of the coefficient. Even though the temperature is higher, the measured loss at 122 K is equal to or lower than the measured loss at 50 K for all modes. The dip between the two modes just above 6 kHz is due to the fact that these modes are from different mode families, which alters the value of the geometric factor \mathcal{D} . Since the measured loss is a combination of all loss sources, the measured data (circles) sit above the TED model (\times) or agree with it. The important lesson to be learned from this graph is that the substrate loss is totally dominated by TED above 50 K except at 122 K. The continuous curves of Figure 12 allows even better understanding of when TED is responsible for the measured substrate loss. See Cagnoli [19] and equation 2.121 for more details about the model.

experiment used to measure loss. For now, it is sufficient to know that the loss of the disk is measured by observing the ringdowns of the disk's normal modes of vibration.

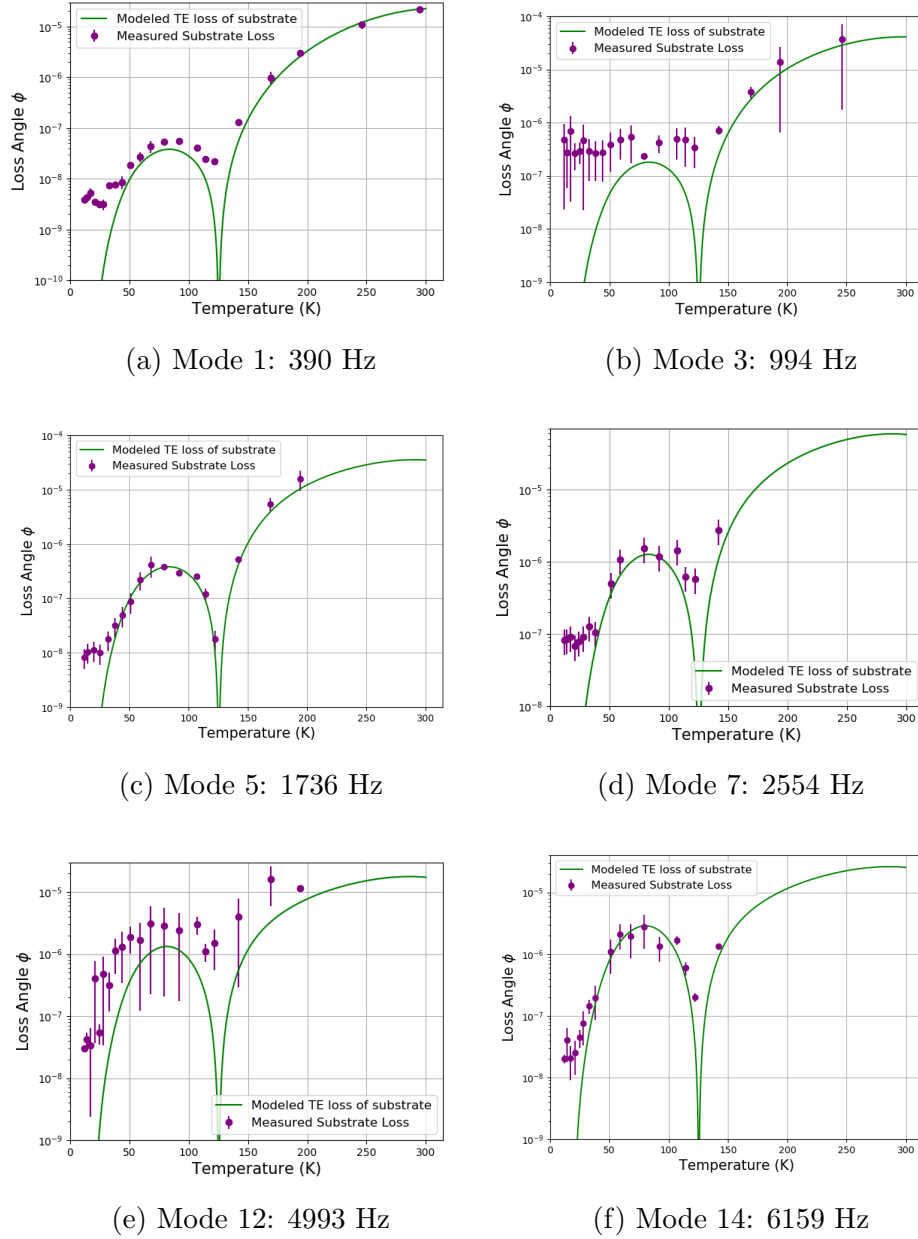


Figure 12 : Modeled substrate loss due to thermoelastic dissipation (green curves) compared to measured substrate loss (purple points) for the first six modes. The green curves were calculated using equation 2.121. The purple points were measured in the Cryogenic Gentle Nodal Suspension by the author, see chapters 3 and 4 for details on the experiment and crystalline silicon substrate measurement process.

Looking at Figure 11 while operating under the assumption that ϕ_{mech} and ϕ_{TE} are the only two dominant sources of dissipation, one can understand for a thin silicon

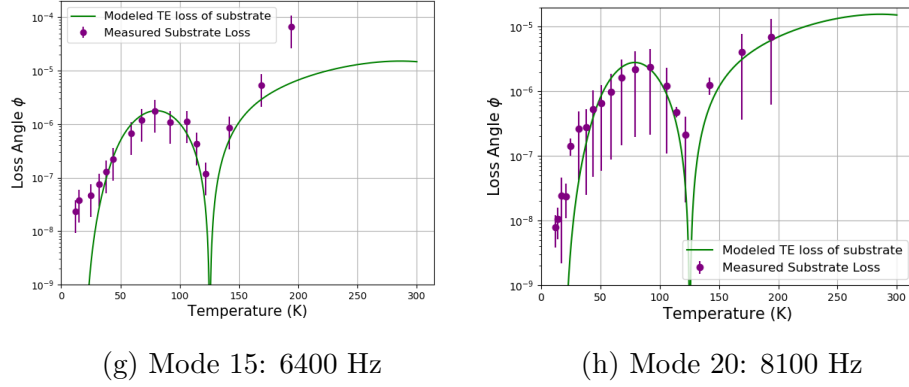


Figure 12 : Modeled substrate loss due to thermoelastic dissipation (green curves) compared to measured substrate loss (purple points) for the last two modes. The green curves were calculated using equation 2.121. The purple points were measured in the Cryogenic Gentle Nodal Suspension by the author, see chapters 3 and 4 for details on the experiment and crystalline silicon substrate measurement process.

disk at what temperatures the loss is dominated by TED, and at what temperatures the loss is due to internal friction. Due to experimental time constraints, the measured loss of the substrate does not have many ringdowns associated with each point. However, as will be shown in chapter 4, these measurements agree within a factor of two with previous work done by Granata *et al* [82]. Therefore, the experimental data can be trusted with few measurements taken.

It is clear at 300 K that the TED is so strong and the loss so large that the ringdown can hardly be measured. A similar effect is observed at 200 K, where TED is pushing the limits of our observational technique. This is reflected by the fact that many of the modes are missing data points at these temperatures; the ringdowns are too short to be measured.

The jump down in ϕ_{TE} at 122 K is startling given the lack of difference in ϕ_{TE} between 200 K and 300 K, but table 1 illuminates this behavior. At 122 K, the coefficient of thermal expansion α is very close to a zero crossing point, and is nearly two orders of magnitude smaller than at 200 K. Equations 2.119 and 2.120 demonstrate that the coupling between the strain and temperature gradients is lost when $\alpha = 0$, and so at 122 K the measured loss is dominated by surface losses [97–99] of the substrate. The surface loss conclusion is made because the loss sits well above the modeled TED and reflects behavior observed before [98, 99].

At 100 K, the ϕ_{TE} jumps back up and establishes dominance again, as is shown by the measured loss mirroring the modeled loss of TED. 50 K is where we begin to see ϕ_{TE} disappear in importance, as the thermoelastic loss drops precipitously to meet the surface loss somewhere between 25 and 50 K for each of the modes of Figure 12. For the last two temperatures, at 12 K and 20 K, the loss due to TED is so low that it is hardly worth considering at all. These are the best temperatures at which to measure the internal friction of a coated thin silicon disk, as the substrate loss will be negligible compared to the additional loss imparted from the coating. Chapter 3 describes in detail how coating mechanical loss is extracted from the measured losses of the coated sample and bare substrate.

Figures 11 and 12 show the effect of mode frequency and temperature on the TED. There is a surface of thermoelastic loss that one can explore by changing both independent variables of frequency or temperature, and the previous figures have just been slices of this surface. The full surface is shown in Figures 13 and 14. The heavy dependence on temperature is further demonstrated by the shape of the surface, where moving in frequency does not change the amount of TED significantly. Across the temperature range, however, a change in the loss by a factor of almost 10^{20} can be observed. The dips at roughly 18 K and 122 K are due to interpolated zero crossing points of the coefficient of thermal expansion, and matches work done by Lyon [94].

This surface was created by interpolating between the many physical parameters that we only have discrete values for. Specifically, these are the quantities in Table 1 and the geometric factors taken from Cagnoli *et al* [19]. The geometric factors show a smooth behavior so long as you stay within the same mode family, so this excluded the modes at 6159 Hz and 8021 Hz, which do not belong to the same family as the rest of the modes. The mode family interpolated between the six other points is the $m = 0$ family, where there are no nodal circles. This is explained more in Chapter 3.

Thermoelastic Dissipation in a Disk with a Thin Film Coating

Due to optical requirements on the test masses of gravitational wave detectors, it is practically, though not theoretically, impossible to build a test mass from a single material. These optical requirements are explored further in section 2.2.1, however for now it is sufficient to know that the test masses are coated in alternating high and low index of refraction materials to meet scattering and absorption performance

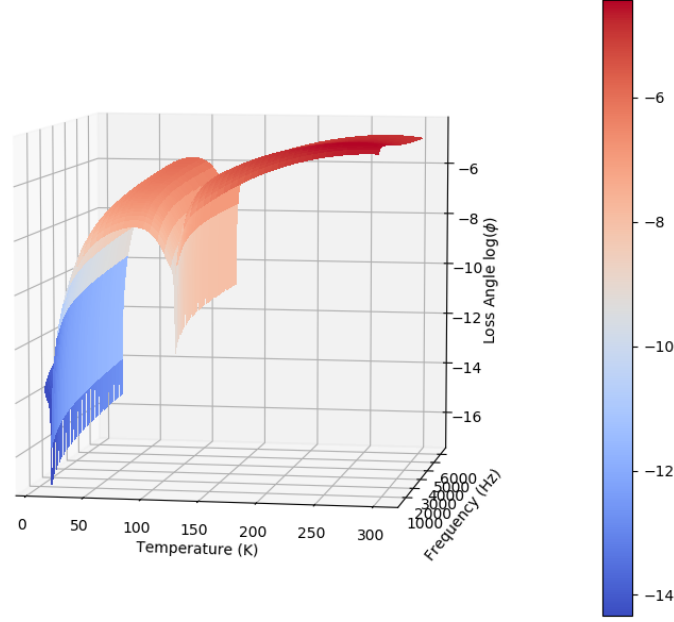


Figure 13 : This plot shows the surface of TED. This view emphasizes the large variance experienced at a single frequency when temperature is varied. Note the z-axis is plotting $\log(\phi_{TE})$ due to limitations of the plotting software.

demands.

The following derivation will follow the work of Zhou *et al* [20]. Start with a simple thin disk resonator with a coating that has thickness l . The substrate that it sits on has thickness of $h - l$. All other dimensions of the coating match the substrate, so one can visualize it as an extremely thin film on top of a disk. This thin film is subject to the strain gradient on the top of the substrate it is bonded to, meaning that the strain it experiences will be driven by the bond to the substrate.

The surface normal of the system is defined to be the z -direction, and the surface itself is located at $z = 0$. Therefore, the film will extend to $z = l$, where the substrate-coating interface is located. The substrate extends downward from the interface until $z = h$, where $h \gg l$. The model assumes the film and substrate are uniform. Under these conditions, the thermoelastic effect and subsequent heat propagation normal to the surfaces are studied.

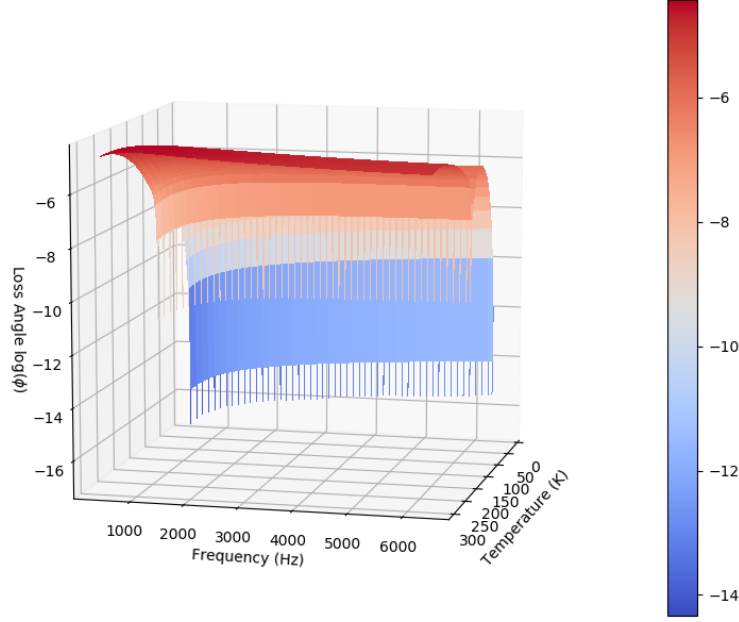


Figure 14 : This plot shows the surface of TED. This view emphasizes the small variance experienced at a single temperature when frequency is varied. Note the z-axis is plotting $\log(\phi_{TE})$ due to limitations of the plotting software.

Since TED is a measure of energy dissipated caused by the coupling of deformation and thermal fields, the relationship between the elastic field and the temperature field it produces are found first. The thermal strain and associated power dissipation can be found after defining the boundary conditions and solving the equilibrium equations. By defining an input stress, elasticity theory can be used to determine the total energy in the system. Using the definition of loss, an expression for the loss due to the coating-substrate interface can be found.

Using the linear heat equation along the z -direction, one can find the temperature distribution coupled to the input elastic field [85],

$$\frac{\partial \theta_j}{\partial t} - \kappa_j \frac{\partial^2 \theta_j}{\partial z^2} = -\frac{E_j \alpha_j T}{(1 - 2\nu_j) c_j} \frac{\partial}{\partial t} \sum \epsilon_{0,j}. \quad (2.126)$$

In the above equation, $\theta_j(t, z)$ is the time and position varying temperature, κ_j is the

thermal diffusivity, E_j is the Young's modulus, α_j is the coefficient of linear thermal expansion, T is the background temperature, ν_j is the Poisson's ratio, and c_j is the specific heat capacity for constant volume. The subscript $j = f, s$ denotes whether the quantity is evaluated in the film or substrate, respectively.

Assuming an exponential form of $\theta_j(t, z) = \theta_j(z)\exp(i\omega t)$ for the temperature field and $\epsilon_0(t) = \epsilon_0\exp(i\omega t)$, equation 2.126 becomes

$$i\omega\theta_j - \kappa_j \frac{\partial^2 \theta_j}{\partial z^2} = -i\omega\beta_j \quad (2.127)$$

where β_j is given by

$$\beta_j = \frac{E_j \alpha_j T}{(1 - \nu_j) c_j} \sum \epsilon_{0,j}. \quad (2.128)$$

The boundary conditions for the heat flux are defined as

$$\begin{aligned} \frac{\partial \theta_f}{\partial z} \Big|_{z=0} &= 0 \\ k_f \frac{\partial \theta_f}{\partial z} \Big|_{z=l} &= k_s \frac{\partial \theta_s}{\partial z} \Big|_{z=l} \\ \frac{\partial \theta_s}{\partial z} \Big|_{z=h} &= 0 \end{aligned} \quad (2.129)$$

where k_j is the thermal conductivity. As previously shown by Fejer *et al* [100], the solution to the heat equation has a particular solution $\theta_{p,j}(z)$ that couples to the strain and a specific solution $\theta_{s,j}(z)$ that meets the boundary conditions. Combining these solutions gives the thermal fields for the film (coating) and substrate,

$$\begin{aligned} \theta_f &= -\beta_f + \frac{\Delta\beta \times \cosh(\gamma_f z)}{\cosh(\gamma_f l) + R \sinh(\gamma_f l) \coth(q)} \\ \theta_s &= -\beta_s - \frac{\Delta\beta R \times \cosh(\gamma_s(h-z))}{\coth(\gamma_f l) \sinh(q) + R \cosh(q)}. \end{aligned} \quad (2.130)$$

Note in the above equation that $q = \gamma_s(h-l)$, $\Delta\beta = \beta_f - \beta_s$, $\gamma_j = (1+i)\sqrt{\pi f c_j / k_j}$, and $R = (k_f \gamma_f) / (k_s \gamma_s) = \sqrt{(k_f c_f) / (k_s c_s)}$.

The stress and strain states, decomposed into in-plane stress and normal stress to the surface, need to be found in order to determine the oscillatory thermal field from an applied stress at a given frequency ω . The elastic fields in the film, denoted by subscript 0, can be found using the elastic boundary conditions.

For stress parallel to the surface, assuming symmetry on the surface, the boundary conditions are given by $\sigma_{0,xx} = \sigma_{0,yy} = \sigma_{0,\parallel}$ and $\sigma_{0,zz} = 0$. Through Hooke's Law, the following relation between stress and strain is found,

$$\begin{aligned}\epsilon_{0,xx,j} &= \epsilon_{0,yy,j} = \frac{1 - \nu_j}{E_j} \sigma_{0,\parallel} \\ \epsilon_{0,zz,j} &= \frac{-2\nu_j}{E_j} \sigma_{0,\parallel}.\end{aligned}\tag{2.131}$$

In matrix form, this can be expressed as

$$\begin{aligned}\epsilon_{0,ii,\parallel,j} &= a_{0,ii,j} \sigma_{0,\parallel} \\ \sigma_{0,ii,\parallel,j} &= b_{0,ii,j} \sigma_{0,\parallel}\end{aligned}\tag{2.132}$$

where

$$\begin{aligned}a_{0,j} &= \begin{pmatrix} \frac{1-\nu_j}{E_j} & 0 & 0 \\ 0 & \frac{1-\nu_j}{E_j} & 0 \\ 0 & 0 & \frac{-2\nu_j}{E_j} \end{pmatrix} \\ b_{0,j} &= \begin{pmatrix} 1 & 0 & 0 \\ 0 & 1 & 0 \\ 0 & 0 & 0 \end{pmatrix}.\end{aligned}\tag{2.133}$$

Thus, the elastic energy stored per unit area is given by

$$\begin{aligned}E_{\text{stored},\parallel,j} &= \frac{1}{2} \sigma \epsilon \times l \\ &= \frac{1}{2} \sigma_{0,\parallel,j}^2 l \sum b_{0,j} a_{0,j} \\ &= \frac{1}{2} \sigma_{0,\parallel,j}^2 l \times \frac{2(1 - \nu_j)}{E_j}.\end{aligned}\tag{2.134}$$

A similar exercise can be done for stress perpendicular to the coated surface. Here the boundary conditions are $\sigma_{0,zz} = \sigma_{0,\perp}$; $\sigma_{0,xx}, \sigma_{0,yy} \neq 0$; $\epsilon_{0,zz} \neq 0$; $\epsilon_{0,xx} = \epsilon_{0,yy} = 0$. Again using Hooke's Law, the following expressions are obtained,

$$\begin{aligned}\sigma_{0,xx,j} &= \sigma_{0,yy,j} = \frac{\nu_j}{1 - \nu_j} \sigma_{0,\perp} \\ \epsilon_{0,zz,j} &= \frac{\sigma_{0,j}}{E_j} \frac{(1 - 2\nu_j)(1 + \nu_j)}{1 - \nu_j}.\end{aligned}\tag{2.135}$$

Once more, one can represent this in a matrix,

$$\begin{aligned}\epsilon_{0,ii,\perp,j} &= d_{0,ii,j}\sigma_{0,\perp} \\ \sigma_{0,ii,\perp,j} &= g_{0,ii,j}\sigma_{0,\perp}.\end{aligned}\tag{2.136}$$

Note that c , e , and f were skipped as placeholder constants since they already represent other quantities. In equation 2.136, $d_{0,j}$ and $g_{0,j}$ are given by

$$\begin{aligned}d_{0,j} &= \begin{pmatrix} 0 & 0 & 0 \\ 0 & 0 & 0 \\ 0 & 0 & \frac{(1-2\nu_j)(1+\nu_j)}{(1-\nu_j)E_j} \end{pmatrix} \\ g_{0,j} &= \begin{pmatrix} \frac{\nu_j}{1-\nu_j} & 0 & 0 \\ 0 & \frac{\nu_j}{1-\nu_j} & 0 \\ 0 & 0 & 1 \end{pmatrix}.\end{aligned}\tag{2.137}$$

Now the elastic energy stored per unit area can be found again, this time for the perpendicular regime,

$$\begin{aligned}E_{\text{stored},\perp,j} &= \frac{1}{2}\sigma\epsilon \times l \\ &= \frac{1}{2}\sigma_{0,\perp,j}^2 l \sum g_{0,j}d_{0,j} \\ &= \frac{1}{2}\sigma_{0,\perp,j}^2 l \times \frac{(1-2\nu_j)(1+\nu_j)}{E_j(1-\nu_j)}.\end{aligned}\tag{2.138}$$

With an expression for stored energy and the form of our stress and strain fields assumed, it will be possible to determine the loss due to the interface once the energy dissipated per cycle is known. The rate of energy dissipation per unit volume in the deformed film is defined by

$$p_{\text{diss},f} = \frac{1}{2} \frac{\sigma \partial \epsilon}{\partial t} = \omega \sum \text{Im}[\sigma_{1,ii}\epsilon_{0,ii} + \sigma_{0,ii}\epsilon_{1,ii}].\tag{2.139}$$

The energy dissipated per unit area is given by

$$E_{\text{diss},f} = \tau \int_0^l p_{\text{diss},f} dz\tag{2.140}$$

where $\tau = 2\pi/\omega$. With equations 2.139 and 2.140 and knowledge of the thermal and applied fields, expressions for the dissipated energy can be found,

$$\begin{aligned}
E_{\text{diss,total},\parallel} &= 2\pi\sigma_0 \times \text{Im} \left[(2\nu_f - 2)\alpha_f\theta_{1,f}\gamma_f^{-1}\sinh(\gamma_f l) \right. \\
&\quad \left. + (4 - 2\nu_f)\alpha_s\theta_{1,s}\cosh(\gamma_s(h-l)) \times l \right. \\
&\quad \left. - 2\alpha_s\theta_{1,s}\gamma_s^{-1}\sinh(\gamma_s(h-l)) \right] \\
E_{\text{diss,total},\perp} &= 2\pi\sigma_0 \times \text{Im} \left[\alpha_f\theta_{1,f}\gamma_f^{-1}\sinh(\gamma_f l) \right. \\
&\quad \left. + \frac{2\nu_f}{1-\nu_f}\alpha_s\theta_{1,s}\cosh(\gamma_s(h-l)) \times l \right. \\
&\quad \left. - \frac{1+\nu_s}{1-\nu_s}\alpha_s\theta_{1,s}\gamma_s^{-1}\sinh(\gamma_s(h-l)) \right].
\end{aligned} \tag{2.141}$$

Using equations 2.134 and 2.138, it is possible to quantify the amount of total stored energy in the coating-substrate system,

$$\begin{aligned}
E_{\text{stored,total},\parallel} &= \frac{1}{2}\sigma_0^2 l \times \frac{2(1-\nu_f)}{E_f} + \frac{1}{2}\sigma_0^2(h-l) \times \frac{2(1-\nu_s)}{E_s} \\
E_{\text{stored,total},\perp} &= \frac{1}{2}\sigma_0^2 l \times \frac{2(1-2\nu_f)(1+\nu_f)}{E_f(1-\nu_f)} + \frac{1}{2}\sigma_0^2(h-l) \times \frac{2(1-2\nu_s)(1+\nu_s)}{E_s(1-\nu_s)}.
\end{aligned} \tag{2.142}$$

Notice in the above equations for $E_{\text{stored,total},j}$ that the first terms represent the energy stored in the film, while the second terms are the energy stored in the substrate.

Finally, the thermoelastic loss can be calculated,

$$\begin{aligned}
\phi_{\parallel,\text{coating,TE}} &= \frac{|E_{\text{diss,total},\parallel}|}{2\pi \times E_{\text{stored,total},\parallel}} \\
\phi_{\perp,\text{coating,TE}} &= \frac{|E_{\text{diss,total},\perp}|}{2\pi \times E_{\text{stored,total},\perp}} \\
\phi_{\text{total,coating}} &= D_{\parallel,\text{TE}}\phi_{\parallel,\text{coating,TE}} + D_{\perp,\text{TE}}\phi_{\perp,\text{coating,TE}}.
\end{aligned} \tag{2.143}$$

The subscripts of ϕ in this final equation are written as such as to make it easier for the reader to distinguish what type of loss is being characterized at a glance. The quantities $D_{k,TE}$ are the dilution factors, and they weight the losses by the relative

amounts of energy in them,

$$D_{k,\text{TE}} = \frac{E_{\text{stored,total},k}}{E_{\text{stored,total},\parallel} + E_{\text{stored,total},\perp}}. \quad (2.144)$$

The reader should be aware that all previous quantities and equations of this section are all related solely to thermoelastic loss, though not all of them are specifically designated as such.

Total Thermoelastic Loss of an AlGaAs-coated Silicon Resonator

Due to the fact that the substrate thickness, $h - l$, is in practice much larger than the film thickness l , equation 2.142 makes it clear that the vast majority of energy is stored in the substrate. Therefore, total energy can be increased by raising the thickness of the substrate. Conversely, the equations of 2.141 demonstrate a smaller increase in dissipated energy due to an increasing substrate [20]. Therefore, with the denominator of equations 2.143 getting larger with substrate thickness, the loss due to thermoelastic dissipation will decrease. This was proven by the work of Somiya and Yamamoto, who found that ϕ decreases with substrate thickness to a point, then plateaus [101].

Using Zhou's coating thermoelastic loss model (equation 2.143) [20] supplemented by Cagnoli's model (equation 2.121) [19] for substrate thermoelastic loss, it is possible to calculate the total thermoelastic loss of the AlGaAs-coated silicon resonator. Loss angles of different mechanisms within a system add linearly, so the total TED is a simple addition of the substrate and coating thermoelastic losses. Values of the various physical parameters needed to calculate coating thermoelastic loss are listed in table 2; continuous curves were created by interpolating between these values.

Although the thermoelastic loss described by equation 2.143 is derived for a single layer coating, it was decided to use this model over the multilayer model described later in Zhou's work. Justification for this decision lies in the behavior of the thermal properties of an AlGaAs-GaAs multilayer stack, especially the thermal conductivity. The thermal conductivity, one of the constants that determine at which frequency the thermoelastic loss peak occurs [100], has been demonstrated to be significantly lower for an AlGaAs-GaAs multilayer stack than for single layer GaAs and AlGaAs [103, 104]. Additionally, the specific heat and thermal expansion properties cited

Table 2 : A table detailing all the constants used for the AlGaAs-GaAs multilayer coating at a given temperature for the TE loss analysis. The value of Young's Modulus E and Poisson ratio σ were held fixed at 83.6 GPa and 0.40 respectively [12]. For the heat capacity, additional data at 30 K and 40 K were included to increase the accuracy of the interpolation. The same was done at 150 K, 175 K, and 250 K for the thermal conductivity.

Thermal Constant	Temperature						
	12 K	20 K	50 K	100 K	122 K	200 K	300 K
$\alpha[\text{K}^{-1}]$ [102]	-1e-9	-1e-8	-1.3e-7	8.0e-7	1.4e-6	3.7e-6	5.0e-6
$\kappa[\text{W/m/K}]$ [103]	350	250	75	25	20	15	10.
$c_V[\text{J/kg/K}]$ [103]	27	51	120	210	250	390	570

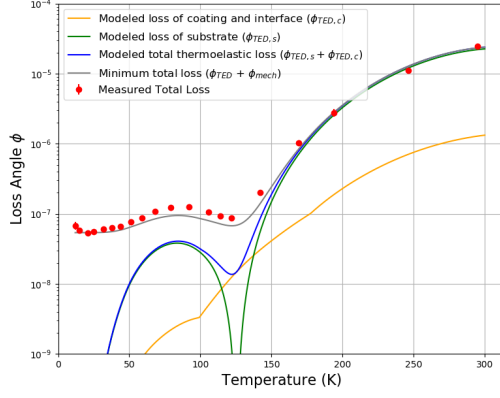
from literature in Table 2 were measured on a multilayer coating. Furthermore, finite element analyses used to model a multilayer coated system also use a single layer approximation due to computational restrictions of simulating a multilayer.

Figure 15 shows the results of this modeling compared to the measured loss for eight different modes. See Chapters 3 and 5 for information on how the loss of the AlGaAs-coated silicon resonator was measured. Although the curves are solely showing loss due to TED, the measured total loss is also influenced by mechanical loss of the AlGaAs coating.

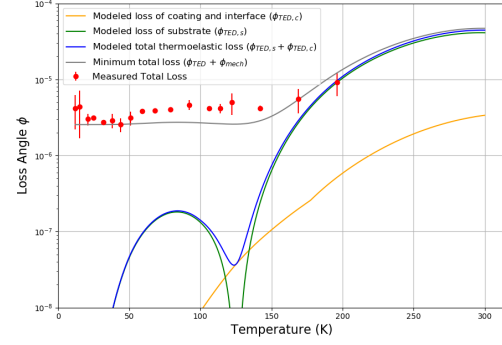
Mechanical loss is the ϕ of equation 2.76, the sources of which are explored in the beginning of this chapter. Mechanical loss of the coatings is the dominate source of thermal noise in gravitational wave detector test masses, due to the ability to push TED down by optimizing test mass geometry, temperature, and material properties [105].

Figure 15 shows that for all modes TED is not a significant source of noise below 40 K; for some modes TED doesn't become relevant until above 140 K. Interestingly, the thermoelastic loss of the substrate dominates as the source of TED at almost all temperatures, except just below 125 K where the coefficient of thermal expansion of silicon crosses a zero point and for high frequency modes near room temperature.

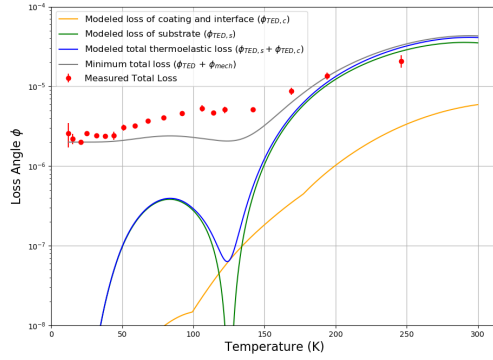
Using Figure 15 as a guide, it is possible to determine for each mode at what temperatures the measured loss is not solely influenced by thermoelastic dissipation. This is critical, since TED can be mitigated in gravitational wave detectors. At the temperatures where TED is the predominant source of all loss, mechanical loss of the coating cannot be accurately determined. However, at temperatures and frequencies where the total loss is determined equally or more by coating mechanical loss, the



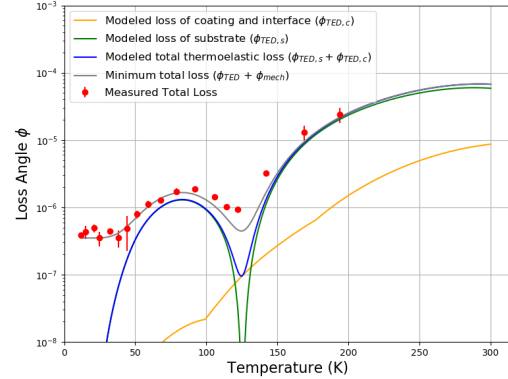
(a) Mode 1: 390 Hz



(b) Mode 3: 994 Hz

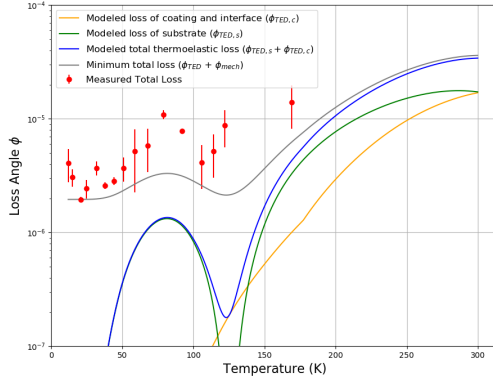


(c) Mode 5: 1736 Hz

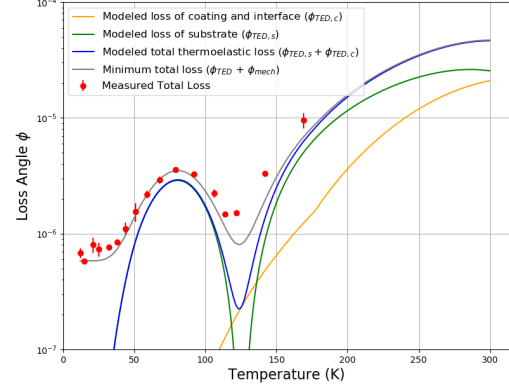


(d) Mode 7: 2554 Hz

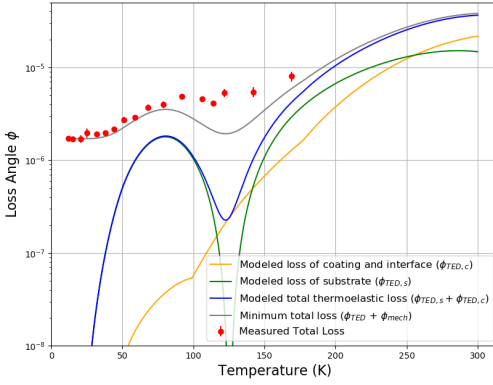
Figure 15 : Modeled thermoelastic loss from 12 K to 300 K for the first four modes. Overlaid in red is experimentally determined data for the total loss of the AlGaAs-coated silicon resonators. The red points were measured in the Cryogenic Gentle Nodal Suspension by the author, see chapters 3, 4, and 5 for details on the experiment and coated sample measurement process. The green curve is the same curve from Figure 12. The yellow curve is the modeled TED of the coating due to the coating-substrate interface from Zhou [20] via the equations of 2.143. The blue curve is the total loss from the substrate (green curve) and coating (yellow curve). The grey curve is the total thermoelastic dissipation (blue curve) plus the lowest mechanical loss measured for that mode. Therefore, the grey curve can be considered a loose minimum.



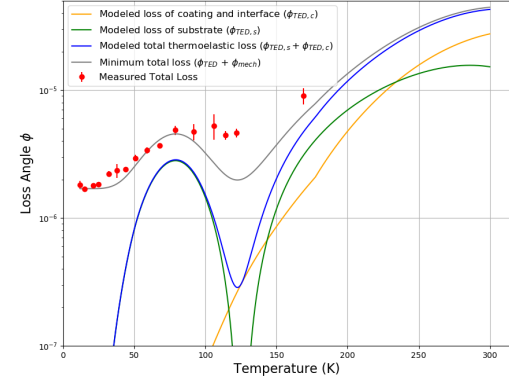
(e) Mode 12: 4993 Hz



(f) Mode 14: 6159 Hz



(g) Mode 15: 6400 Hz



(h) Mode 20: 8100 Hz

Figure 15 : Modeled thermoelastic loss from 12 K to 300 K for the last four modes. Overlaid in red is experimentally determined data for the total loss of the AlGaAs-coated silicon resonators. The red points were measured in the Cryogenic Gentle Nodal Suspension by the author, see chapters 3, 4, and 5 for details on the experiment and coated sample measurement process. The green curve is the same curve from Figure 12. The yellow curve is the modeled TED of the coating due to the coating-substrate interface from Zhou [20] via the equations of 2.143. The blue curve is the total loss from the substrate (green curve) and coating (yellow curve). The grey curve is the total thermoelastic dissipation (blue curve) plus the lowest mechanical loss measured for that mode. Therefore, the grey curve can be considered a loose minimum.

TED will not prohibit accurate measurement of coating mechanical loss. Evidence to support this statement is presented in section 3.3.

2.1.4 Thermo-Refractive Noise

Statistical fluctuations in the temperature of the HR stack couple to the index of refraction of the coatings. Since the coatings operate as Bragg reflectors, the optical path and phase of the incident light determines the phase of the reflected light. Therefore, these fluctuations in temperature, however small, will couple into the phase of the light reflected. This effect is referred to as thermo-refractive noise.

This phenomenon can be quantized through a material's thermo-optic coefficient, given by

$$\beta = \frac{dn}{dT}. \quad (2.145)$$

Braginsky [106], who's work the remainder of this section shall follow, calculates the phase shift produced from temperature fluctuations in a HR coating stack,

$$\delta\phi = 4\pi\beta_{\text{eff}}\bar{u}. \quad (2.146)$$

The average temperature fluctuation is given by \bar{u} , while β_{eff} is an effective thermo-optic coefficient of the alternating coating layers,

$$\beta_{\text{eff}} = \frac{n_{\text{L}}^2\beta_{\text{H}} + n_{\text{H}}^2\beta_{\text{L}}}{4(n_{\text{H}}^2 - n_{\text{L}}^2)}. \quad (2.147)$$

The subscripts, H and L, represent material properties of the high and low index layers respectively.

The phase noise caused by this effect can be expressed as a power spectral density, such that it can be compared to other noise sources. The spectral density of thermo-refractive noise is

$$S_x(\omega) = \frac{\sqrt{2}\beta_{\text{eff}}^2\lambda^2\kappa T^2}{\pi r_0^2\sqrt{\omega\rho C\lambda^*}} \quad (2.148)$$

where λ is the wavelength of the incident light, κ is the thermal conductivity, T is the temperature, r_0 is the radius of the beam spot of the laser, ω is the angular frequency, ρ is the density, C is the specific heat capacity, and λ^* is the effective wavelength of the light inside the coating layers.

2.1.5 Thermo-Optic Noise

Thermoelastic dissipation and thermo-refractive noise are linked, as temperature fluctuations in the coating are responsible for both sources of noise. These temperature fluctuations drive both the expansion/contraction of the coatings, while also altering their indices of refraction. Evans *et al* [105] developed a formalism for handling both noise sources at once, herein referred to as thermo-optic noise.

Using the same formalism developed by Zener [91], they found the power spectral density of a Gaussian beam incident on the HR coating stack to be

$$S_{TO}^{\Delta T}(f) = \frac{2\sqrt{2}k_B T^2}{\pi r_0^2 \sqrt{\kappa C \omega}}. \quad (2.149)$$

The quantities here are the same as in equation 2.148, with the addition of Boltzmann's constant, k_B . From this point, Evans *et al* move on to derive the power spectral density along the direction the incident light is moving, z ,

$$S_{TO}^{\Delta z}(f) \simeq S_{TO}^{\Delta T}(f) \left(\bar{\alpha}_c d - \beta_{\text{eff}} \lambda - \bar{\alpha}_s d \frac{C_c}{C_s} \right)^2. \quad (2.150)$$

There are a number of new quantities in equation 2.150. Starting with the simple ones, d is the thickness of the total coating, while the subscripts s and c represent material properties of the substrate and coating respectively. Evans *et al* took from the work of Fejer *et al* [100] to define the quantities that follow. C_c is a simple volume average of the heat capacities of each layer, similar to β_{eff} given by equation 2.147. $\bar{\alpha}_c$ expresses an effective coefficient of thermal expansion for the coating stack, given by

$$\bar{\alpha}_c = \sum_{k=1}^N \bar{\alpha}_k \frac{d_k}{d} \quad (2.151)$$

where d_k is the thickness of the k th coating layer. Moving one step deeper, $\bar{\alpha}_k$ is an effective coefficient of thermal expansion for the k th coating layer,

$$\bar{\alpha}_k = \alpha_k \frac{1 + \sigma_s}{1 - \sigma_k} \left[\frac{1 + \sigma_k}{1 + \sigma_s} + (1 - 2\sigma_s) \frac{E_k}{E_s} \right]. \quad (2.152)$$

Knowing equation 2.150 encodes both TED and thermo-refractive noise, it might be surprising to see the effects of thermo-refractive noise are negative with respect

to TED. It is therefore possible to select materials such that the thermoelastic and thermo-refractive partially cancel out, producing an overall effect that is smaller.

2.2 Coating the Test Masses

This chapter has focused heavily on deriving coating thermal noise sources, mechanical loss and thermoelastic dissipation (TED), from first principles, but has yet to discuss in detail why it is relevant to gravitational wave detectors.

There is no single material that can feasibly meet all the optical requirements and provide low thermal noise. Specifically, the test mass substrate, fused silica, meets all the requirements of absorption and scatter, but it is not practical to create a multilayer coating out of just fused silica that can provide the reflectivity necessary to sustain the high finesse Fabry-Pérot cavity. Therefore, the test mass substrate is made from fused-silica, a very low noise material that fulfills the requirements for thermal noise. The required reflection and transmission properties of the input and end test masses are handled by coating the fused silica substrate in alternating high and low index of refraction materials. Since fused silica is such a low loss material with high optical performance, it comprises the low index of refraction layers of the coating, while the high index layer is titania-doped tantala [56, 107].

2.2.1 Optical Demands on the Test Masses

The test masses of the detectors are under strict requirements of reflectivity, $R > 99.999\%$, and absorption, 0.5 ppm, in order to maintain the finesse required of such an optical cavity. In order to achieve the reflectivity needed to reach these high levels of finesse for the 4 km Fabry-Pérot cavity, the test masses are currently coated in alternating layers of amorphous silica and titania-doped tantala ($\text{TiO}_2\text{:Ta}_2\text{O}_5$). The titania doping of the high loss tantala pentoxide was a procedure done to lower thermal noise of the HR stack, developed by Harry *et al* and then optimized by the LMA [108–110].

These layers serve as Bragg reflectors, and thus the layer thickness, d_k from section 2.1.5, is chosen to be $\lambda/4$, or 266 nm. The loss of this stack is dominated by the high index tantala layers, despite the great improvement when doped with titania. The silica layers have $\phi \lesssim 5 \times 10^{-5}$, while the tantala layers are roughly ten times higher

at $\phi \approx 4 \times 10^{-4}$ [88, 111]. To create the Bragg reflecting layers, the layers of titania doped tantala and silica are stacked alternating layer-by-layer. The tantala, with an index of refraction of $n_{high} = 2.12$, fulfills the role of the high index material, while the silica, with an index of $n_{low} = 1.44$, serves as the low index material.

In order to improve upon the current detector levels of coating thermal noise, any future coating would need to alter one of two properties, mechanical (thermal) or optical. A coating that has the same optical properties as $\text{TiO}_2:\text{Ta}_2\text{O}_5$ but lower thermal noise would of course lower the overall noise of the entire HR stack. Alternatively, a new coating that has the same or even slightly worse thermal noise but higher index of refraction would reduce the number of total layers necessary to achieve the desired reflectivity. Fewer thermally noisy higher index layers could work just as well as a greater number of less noisy lower index layers. Ideally, a future coating would improve both the mechanical and optical properties, leading to a much larger improvement in thermal noise levels.

2.2.2 Strain Sensitivities of Present Detectors and Coating Noise

As of the end of 2022, there are five operating gravitational wave interferometers with another planned to be built in India. Two are located in the United States, the twin 4 km aLIGO detectors of Hanford, Washington and Livingston, Louisiana. Two more are located in Europe; 600 m GEO600 in Sarstedt, Germany and 3 km AdVIRGO operating from Santo Stefano a Macerata, Italy. Lastly, there is the cryogenic interferometer KAGRA, with the test masses held at 20 K [8], located in the Gifu prefecture of Japan.

The twin Advanced LIGO detectors are so called due to their goal of joint noise reduction. Each is designed such that their components are shared between both detectors. The design laser power circulating in the arms is 750 kW, but only a third of that power has been realized due to point absorbers on the faces of the test masses [112]. The purple lines, dashed and solid, of Figure 16 show the strain sensitivity of these detectors. The dashed line represents the goals for the A+ upgrade, which is the set of improvements made for the next observing runs, O4 and O5. The majority of the upgrade is slated for the O5 observing run, assuming new coatings are installed for that run. The test masses of the twin detectors are currently coated in an HR stack of alternating layers of titania doped tantala and silica, as discussed in section

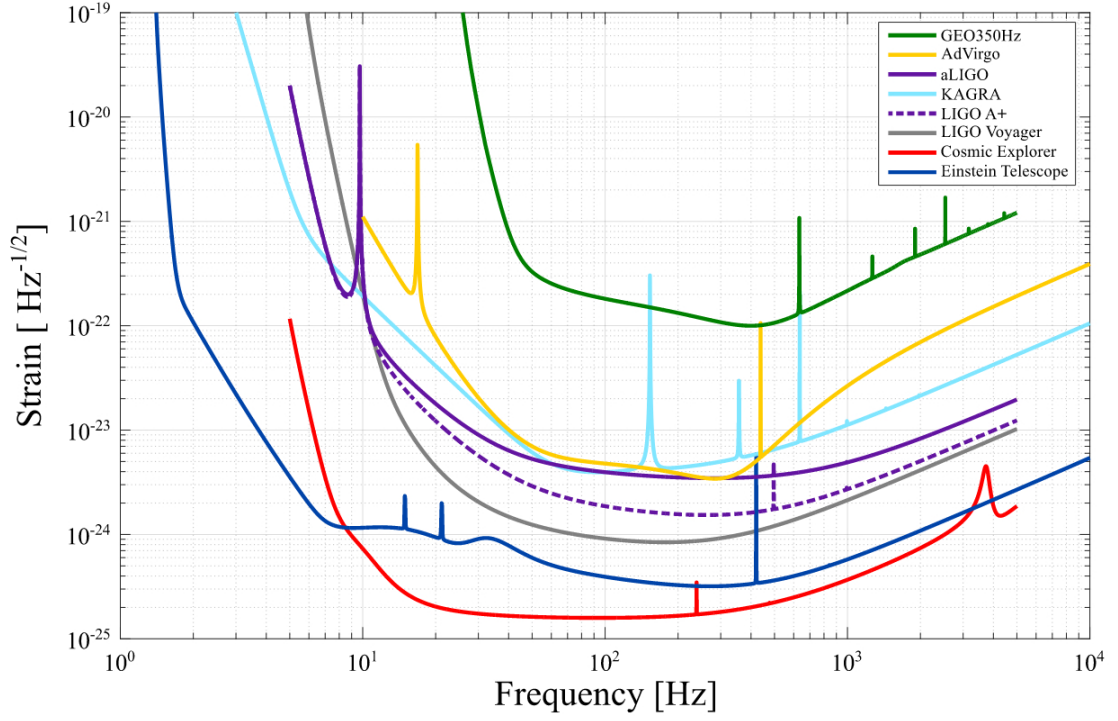


Figure 16 : Strain sensitivities of present (GEO, VIRGO, aLIGO, LIGO A+, KAGRA) and next generation detectors (LIGO Voyager, Cosmic Explorer, Einstein Telescope). Note that all curves except GEO600, AdVirgo, and aLIGO are all theoretical desired goals of these detectors. Image credit to Robie [21].

2.2.1.

Although they have yet to meet their design sensitivities, the aLIGO detector was more than 10 times as sensitive as initial LIGO. In a recent observing run O3a, the detectors were operational for over 150 days. LIGO Hanford was observing for 71.2% of the run, called its duty cycle, with an average inspiral detection range of 113 Mpc, while LIGO Livingston had a duty cycle of 75.8% with a range of 134 Mpc. Over 40 candidate gravitational wave events were detected in this time [113]. The most recent observing run, O3b, had the detectors operating for almost 150 days, from 1 November 2019 to 27 March 2020. Hanford and Livingston were both observing for 79% of this time, while their respective inspiral detection ranges were 115 Mpc and 133 Mpc. Over the second half of O3, 35 candidate gravitational wave events were detected [114].

GEO600 is a joint operation between the Max Planck Institute for Astrophysics of Garching, Germany and the Institute for Gravitational Research of Glasgow, Scotland. Although it is not competitive today with other gravitational wave detectors due to its shorter arm length, it has served as a critical testing ground and proof-of-concept since its completion in 2001. No gravitational wave events have been observed by GEO600.

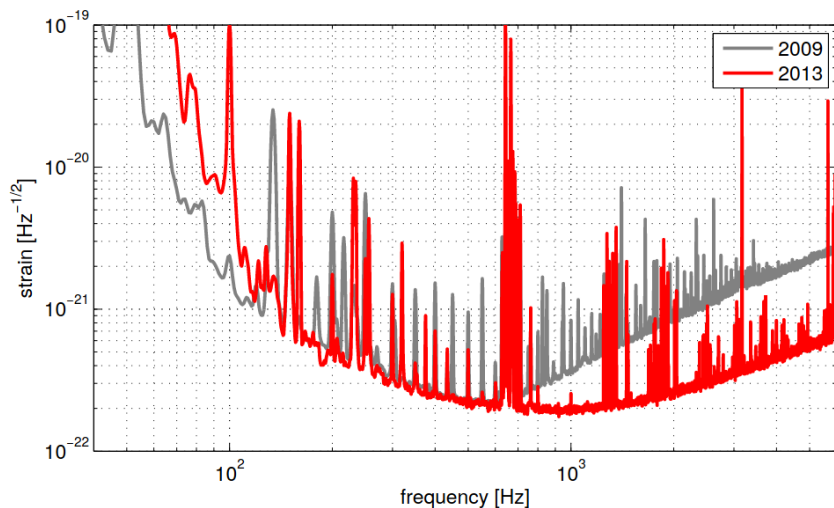


Figure 17 : Strain sensitivity evolution of GEO600 from 2009 to 2013. Notice the large improvement at frequencies above 500 Hz, where implementation of quantum squeezing of light has pushed down quantum shot noise. Plot credit to Dooley [22].

Many of the upgrades and improved technologies used in detectors that have measured gravitational wave events, LIGO and AdVirgo, were prototyped and tested first within GEO600. The monolithic silica fibre suspension systems of the test masses that are now used in the American and European detectors were first implemented in GEO600. Additionally, GEO600 was the first gravitational wave detector to inject squeezed states of light into the interferometer [115]. For more information on quantum squeezing, see the previous reference and this paper by the LIGO Scientific Collaboration [116].

The most recent upgrades to GEO600 have focused on improving its high frequency sensitivity above 500 Hz. At these frequencies, quantum shot noise is the dominant noise source limiting sensitivity. By injecting squeezed states of light, this noise can be pushed down by sacrificing sensitivity at lower frequencies where radiation pressure dominates [22, 117].

Advanced Virgo (AdVirgo) is the third version of the 3 km gravitational wave detector in Italy. It is operated in collaboration by institutions across Europe, and has gone through many upgrades since its initial construction. AdVirgo has been contributing to detecting gravitational wave events since it joined the twin LIGO detectors in the second observing run O2. The detector is pictured in Figure 18.

Although not depicted in Figure 16, at low frequencies AdVirgo has higher sensitivity than the twin LIGO detectors [60]. This is due to AdVirgo's unique seismic isolation system, known as the Virgo Superattenuator. It is composed of multiple stages of passive isolation, suppressing seismic noise down to 4 Hz [118].

During the O2 observing run, AdVirgo maintained a remarkable observation percentage of 86% [119]. The detector was key in triangulating the position of GW170817, which was the first detection of merging neutron stars and the first astronomical event measured by neutrino detectors, gravitational wave observatories, and traditional telescopes [120]. During the most recent observing run O3, AdVirgo had the highest duty cycle and contributed to more than 70% of the gravitational wave events detected [59, 121].

The last of the currently operating gravitational wave detectors is the Kamioka Gravitational Wave Detector, KAGRA. Depicted in Figure 19, KAGRA is a 3 km long detector located in the Gifu prefecture of Japan, built 200 m underground to minimize seismic and gravitational gradient noise impacting low frequency sensitivity.



Figure 18 : An aerial view of AdVirgo, located in Santo Stefano a Macerata, Italy. Image credit to the VIRGO collaboration [23].

KAGRA is unique in that it utilizes sapphire test masses, contrasted with the fused silica of the LIGO and Virgo detectors. This is due to sapphire's lower levels of thermal noise at cryogenic temperatures. KAGRA is the first detector to cool its optics [122].

To minimize thermal noise from the test mass coatings and substrates, KAGRA cools them to roughly 20 K. In order to reach similar levels of strain sensitivity as LIGO and AdVirgo, the suspension fibers and the main optics are all composed of crystalline sapphire, which has lower mechanical loss (thermal noise) than fused silica at temperatures below approximately 150 K.

Figure 16 shows KAGRA's design sensitivity, but to-date it has only reached a percentage of this detection range. During a joint run with GEO600, KAGRA averaged a BNS inspiral detection range of just 660 kpc, with a peak of 1 Mpc [123]. This is less than 1% of the inspiral range of the LIGO and AdVirgo detectors, which the design sensitivity seeks to match. Work is ongoing at the KAGRA detector to push down noise sources, maintain stability, and build power in the arms of the interferometer in order to achieve design sensitivity.

Comparing Figure 8 and Figure 16, one can see where coating thermal noise is limiting detector sensitivity in the LIGO detectors today. In recent years, quantum squeezing techniques have matured and pushed down the quantum sensitivity limit in the critical region around 100 Hz. Once squeezing is fully implemented into the detectors to reduce both shot noise and radiation pressure noise, the detector sensitivity will be limited at frequencies roughly between 30 Hz and 120 Hz by coating thermal noise alone [124].

The performances of the previously discussed detectors are all expected to improve

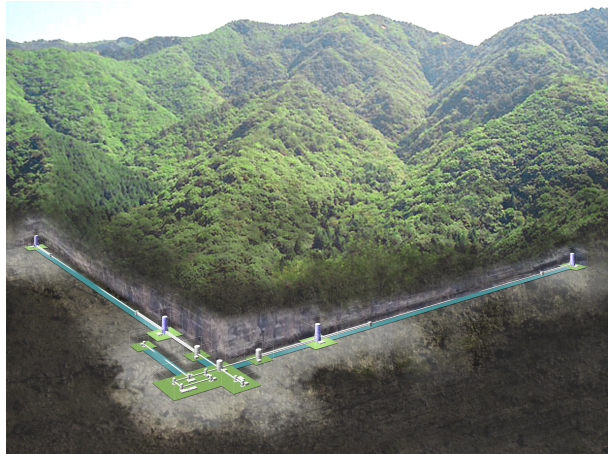


Figure 19 : A picture of the KAGRA detector situated beneath the mountains it sits 200 m beneath. Photo courtesy: KAGRA Observatory, ICRR, The University of Tokyo [24].

for the next observing runs, O4 and O5. As was previously discussed, KAGRA has only reached one percent of its design sensitivity. However, the twin aLIGO and AdVirgo detectors both need significant improvements in order to reach their design sensitivities as well. The strain sensitivity goals for aLIGO and AdVirgo have the overall noise levels in the detection frequency band about 2-4 times lower noise than what was achieved in O3 [25–27].

Figures 20 and 21 demonstrate the problem clearly, especially when considering the nature of the (coating) thermal noise curve of Figure 8. If the design sensitivities for O4 and O5 are to be met, the current coatings need to be improved. See section 2.2.4 for more information on how this is being done.

2.2.3 Strain Sensitivities Required of Third Generation Detectors

In addition to upgrades required to meet design sensitivities of the current detectors, there are plans to build completely new, better performing gravitational wave interferometers. The largest and most sensitive of these will be the Einstein Telescope of Europe and Cosmic Explorer of North America. However, there are also designs for an intermediate detector that will be the initial third generation detector constructed, bridging the gap between the current second generation and third generation. These plans have oscillated in scope and convention; the current most popular plan is a room-temperature upgrade called A[#]. There were prior plans for a detector called

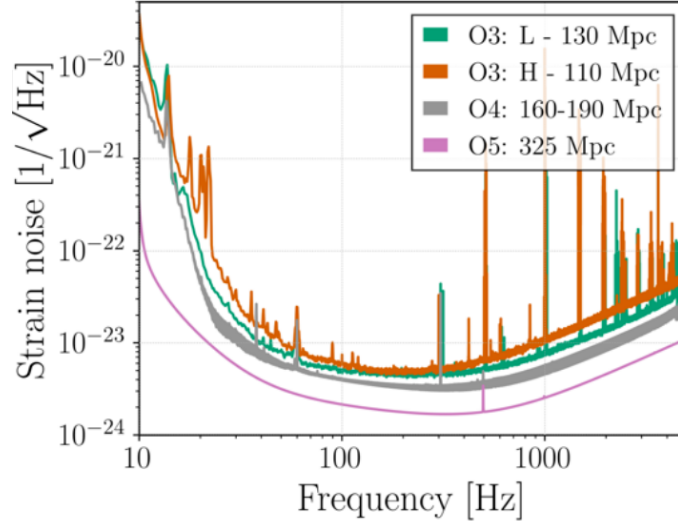


Figure 20 : A+ LIGO strain sensitivity for O3 and design curves for O4 and O5 [25]. The O5 curve is the design sensitivity of A+ [26]. Notice the O5 curve is roughly three times as sensitive as the O3 curve at 100 Hz. Coating thermal noise is the dominate noise source in this frequency regime.

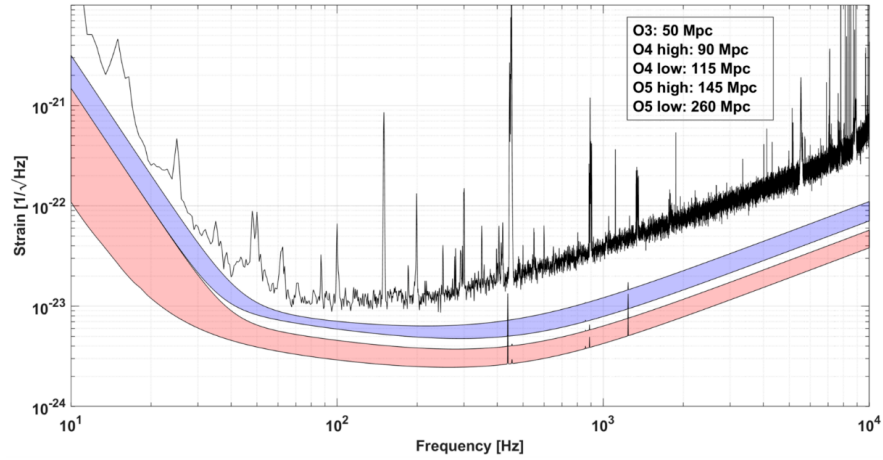


Figure 21 : AdVirgo strain sensitivity for O3 and design curves for O4 and O5. [27]. Notice that the O5 high curve, the least amount of sensitivity acceptable to meet the design goal, is roughly twice as sensitive as the O3 curve at 100 Hz. Coating thermal noise is the dominate noise source in this frequency regime.

LIGO Voyager, but that has fallen out of favor. While A[#] and Voyager are expected to achieve the same sensitivity, A[#] is planned to use room temperature test masses while LIGO Voyager was exploring cryogenic test masses.

This next upgrade, whether LIGO Voyager or A[#], is designed to improve detector sensitivity by a factor of four as compared to current aLIGO sensitivity goals, without any major changes to detector design. It will incorporate work done by GEO600 to inject squeezed light into the interferometer, increasing its sensitivity at high frequencies. Additionally, the test mass is getting a large upgrade and will weigh 200 kg, an improvement over the 40 kg of current test masses [125].

LIGO Voyager was planned to operate at cryogenic temperatures at the first zero crossing point of crystalline silicon's coefficient of thermal expansion, around 123 K. This means the test mass substrate would be made of crystalline silicon instead of the fused silica used in current room temperature detectors or the sapphire used in KAGRA. Although the substrate will be different materials, the techniques and lessons learned from KAGRA would be critical in building LIGO Voyager to design specifications [125]. As of the writing of this thesis, the LIGO Scientific Collaboration has chosen to pursue the A[#] design for its next major upgrade.

Cosmic Explorer is the largest next generation detector, with plans to make the interferometer arms a full 40 km long, possibly complemented by an additional detector with 20 km arms. With a planned sensitivity of ten times that of Advanced LIGO, Cosmic Explorer would be able to observe gravitational wave events from the edge of the observable universe. Thanks to its advanced sensitivity, Cosmic Explorer is expected to see millions of mergers, enabling astronomers and physicists to map the populations of compact objects across nearly all of time since the Big Bang [10].

As can be seen in Figures 16 and 22, Cosmic Explorer will have remarkable sensitivity in lower frequencies between 10 and 300 Hz. This will give it unparalleled ability to see high mass mergers, a difficult to penetrate blind spot in current generation detectors at the lowest frequencies. There will also be additional frequency dependent squeezing, as compared to current detectors. Lastly, Cosmic Explorer is also considering the possibility of operating at cryogenic temperatures, if it is found to sufficiently lower thermal noise [10]. Due to the lessons learned from KAGRA, this seems unlikely to be pursued, but has yet to be ruled out.

Last of the next generation detectors is the Einstein Telescope (ET). It is planned

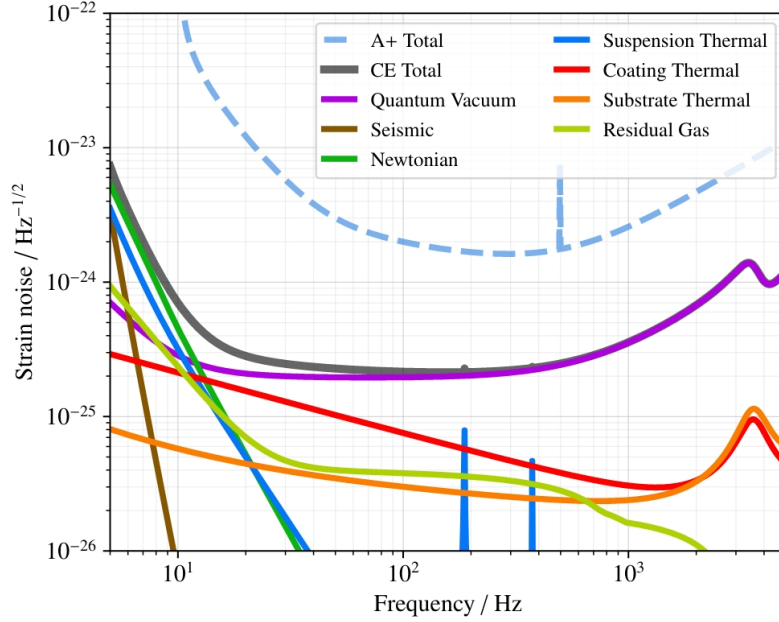


Figure 22 : The noise budget for Cosmic Explorer. Although all noise sources are significantly reduced as compared to their current generation counterparts, notice the order of magnitude drop in coating thermal noise (red line) from the A+ total curve (dashed light blue line). Image credit to Evans *et al* [10].

to be comprised of six independent 10 km detectors arrayed within one another in a triangle pattern. These six detectors will be housed 100-300 meters below ground, and at least some will be operated at cryogenic temperatures at or below 123 K. The detectors will be tuned to a different bandwidth of frequency space, with half being optimized for high frequency and the other half at low frequency. This allows ET to be sensitive in a wide range between 2 Hz and 10 kHz [9].

In order to achieve such high sensitivity, coating thermal noise will need to be reduced by an order of magnitude. This can be seen by comparing Figures 8 and 22. After dividing the plot of thermal noise in Figure 8 by the 4000 meter arm length to make the units agree, it still sits roughly ten times higher than what is required of Cosmic Explorer. A new multilayer coating stack, along with new layer materials, will have to be designed and tested in order to achieve this level of detector sensitivity. Though, if CE is able to be built at its largest possible arm length, it may be possible to achieve the low loss levels using the current coatings [10].

2.2.4 Improving the Coatings

Although the following discussion will focus on amorphous coatings, of which AlGaAs is not, it is prudent to explore the techniques by which the coatings have improved in the last two decades.

In amorphous coatings, as with crystalline coatings, the internal atomic structure determines the coating loss and absorption. However, unlike crystalline coatings, amorphous internal structure is isotropic. The differences in local internal structure of amorphous coatings can be modeled as a system of potential energy states with differing positions and magnitude of stability. Heat treatment via annealing provides additional thermal energy to the system, and can alter the potential energy landscape such that the new bond orientations are, in general, more stable. This creates an amorphous coating that has lower internal mechanical loss [84, 126].

Annealing can be better understood via the application of a Two Level System (TLS) model. These models were first used to explain and characterize the thermal properties and internal friction (mechanical loss) of materials below 1 K [127–129]. Amorphous oxides have had their mechanical losses modeled by an ensemble of TLSs, where each TLS is coupled to the mechanical field. This coupling causes excitations in the TLS and the ensuing relaxation [130]. Once one has the TLS distribution, the coupling to the mechanical field, and the relaxation time, it is possible to replicate experimental low-temperature behavior. The model, which was developed with a focus on mimicking low temperature tunneling, was expanded to explain phenomena at warmer temperatures by incorporating thermal hopping between the TLSs [130, 131]. The cold temperature experiment described in chapter 3 was built in large part to obtain cold temperature data to constrain these TLSs and understand loss mechanisms in possible test mass coatings.

This principle has been applied to the process of building the coating itself. Recent experimental measurements suggest that high temperature deposition can significantly impact mechanical loss, it is believed by lowering the density of TLSs in the system [132–134]. By depositing the coating at elevated temperature, the thermal energy and therefore the mobility of atoms in the coating layer is increased. This leads the molecules to settle into a lower energy quantum state, which means they

are less likely to jump between states given the greater energy gap between lower energy states [126, 132]. Unfortunately for gravitational wave detectors, the annealing process and high temperature deposition increases the risk that the sample will crack or crystallize when heated, leading to unacceptable levels of optical scatter [59].

Where heat treatment has failed or led to crystallization, doping has been used to attempt to fill the void. By doping an amorphous material with metals, such as titania or zirconia, the temperature at which crystallization occurs can be raised and mechanical loss can be lowered. Via higher temperature annealing and lower base mechanical loss, such doping achieved roughly 40% lower loss as compared to the undoped coating. The current gravitational wave test mass high-index coating, titania (TiO_2) doped tantala (Ta_2O_5), was chosen for these reasons. These layers of $\text{Ti}:\text{Ta}_2\text{O}_5$ have loss levels of $\phi_{\text{mech}} \approx 2 \times 10^{-4}$ [90, 109]. Additional dopants that have been explored besides tantala include halfnia, zirconia, niobia, alumina, and germania. These have all been tested in conjunction with different doping percentages, annealing temperatures, and deposition parameters.

Alternative high index of refraction materials are the next logical step beyond annealing and doping. Amorphous silicon and amorphous germanium are both of interest due to their low levels of mechanical loss, but they are inhibited by levels of absorption more than a thousand times worse than required. However, by operating at lower temperatures and with longer wavelength lasers, the absorption of these materials is altered to acceptable levels. As such, these materials are of interest as possible coatings for third generation detectors [125, 135].

Such incremental improvements led to the exploration of AlGaAs-GaAs coatings as a possible solution to the coating noise problem, for both current and future generations of gravitational wave detectors [5, 6, 136–139]. The goal of this thesis is to determine the mechanical loss of such a coating at cryogenic temperatures. This work will help inform the experimental gravitational wave community whether Al-GaAs coatings are suitable for both current and third generation gravitational wave detectors.

Before that question can be answered, another one must be addressed. Data showing measured mechanical loss was presented in earlier sections of this chapter, but an explanation for how that data was collected was absent. Although sections 2.1.1 and 2.1.2 discussed the theory behind Brownian noise, that was all applied in

the context of a beam hitting a test mass. The astute reader may have already asked themselves, how is an abstract quantity such as mechanical loss of a test mass coating measured before it is installed in a gravitational wave detector?

Chapter 3

Multi-Modal Gentle Nodal Suspension

The importance of mitigating loss in the LIGO test masses due to coating thermal noise has been rigorously explored, though the process by which thermal noise is measured has not. This chapter will rectify that problem, discussing briefly the multiple ways in which mechanical loss can be measured. However, the main focus of this chapter will be on the system known as the Gentle Nodal Suspension (GeNS). Its general history in the field of test mass mechanical loss research will be discussed, along with the specific cryogenic system at Syracuse University that forms the bedrock of this thesis.

The reader will first be familiarized with the multiple ways loss was measured in the early years of measurement; at least one of these methods, the welded suspension, is still used today. After that brief lesson, the history and operation of the experiment known as the GeNS, a form of which was used to collect all the experimental data presented in this thesis, will be explored. The process of extracting coating loss from a total coating-substrate loss will be analyzed, and the reader will be left with the knowledge of how to measure coating mechanical loss. Lastly, the specifics of the Cryogenic GeNS system (Cryo-GeNS) at Syracuse University will be presented to prepare the reader for the subsequent chapters detailing the loss results obtained from the Cryo-GeNS.

3.1 Measuring Thermal Noise

Some of the first measurements of internal mechanical loss within the gravitational wave community were carried out not on coating materials, but that of the substrate. Although fused silica was widely known as a good candidate to comprise the test mass bulk in the late 1990s, thermal noise from the bulk was still expected to have a large influence on the noise budget of the as yet constructed gravitational wave detectors [140].

One of the ways this open question about fused silica internal loss was being explored was through a direct measurement of the anelastic aftereffect observed via the photoelastic effect when a stress is suddenly applied or removed from a fused silica sample. By shining a laser directly through a succession of components, a linear polarizer, a photoelastic modulator, the fused silica sample, and then another 90° rotated linear polarizer, birefringence is measured. The sample, under applied stress, will create stress induced birefringence. However, this method lacked the sensitivity to measure the very low loss in high purity fused silica [140, 141]. It never yielded confident measurements of internal loss.

In addition to the anelastic measurements, an early form of a nodal suspension was used on large fused silica substrates by Numata *et al* [142]. In this system, the vibrational modes of the cylinder are excited via PZT and the loss is measured by observing the ringdown of these modes, contained within the amplitude of the displacement readout. The details of such a ringdown displacement measurement will be explored later in this section. Numata’s system was different from the current generation GeNS because their cylindrical fused silica sample was clamped at both faces by ruby balls, a level of constraint not present in a GeNS apparatus. When the loss is measured via resonant mode ringdowns, sometimes the samples are referred to as “resonators.” This work uses these terms interchangeably unless otherwise noted.

Although these methods produced loss measurements, successfully for Numata, the community shifted for the next decade to predominantly measure loss by suspending lower thickness silica samples from welded wires with diameters on the order of 100s of micrometers [88, 97, 143–145]. The clamped method of Numata introduced additional losses due to the clamp, while the welded fused silica suspensions, when properly engineered, did not introduce additional loss from the suspension. Although

less popular, loss was also measured by welding cantilever blades to a clamping block of the same material [146].

Welded suspension experiments all operate roughly the same way. The sample to be measured, whether simple fused silica or a coating on a silica substrate, would be welded to fine suspension fibers and suspended in vacuum. The weld would be attached at the top of the sample. A comb exciter is placed as close to the sample as possible. When an oscillating high voltage is passed through the exciter, the vibrational modes of the sample are excited. The amplitude of the modes over time can then be tracked via either a shadow sensor for suspension measurements, or birefringence sensors for coating experiments [88, 143–145].

3.1.1 Vibrational Mode Ringdowns and Coating Thermal Noise

Many of the above methods as well as the GeNS system used in this work all employ the technique of observing vibrational mode ringdowns to determine the loss of a desired system. However, it is not obvious how the ringdown of a vibrational mode relates to the loss angle derived in chapter 2.

Recall from equation 2.69 that loss angle, the same loss angle used to characterize anelasticity and internal friction of a material, is directly related to the energy lost per cycle of dissipative process. For a more intuitive understanding of what kind of information the loss angle encodes, imagine a single damped harmonic oscillator. Whether the damping is from one source or multiple, the loss angle is defined as the energy dissipated per cycle [59],

$$\phi = \frac{E_{\text{diss}}}{2\pi E_{\text{stored}}}. \quad (3.153)$$

For a system that is oscillating back and forth according to its resonant modes, the amplitude of the oscillation is a direct measurement of the amount of energy in that mode. Therefore, if one knows the frequency of the oscillation, it becomes possible to directly measure the loss angle of the n th mode [88],

$$\phi_n(f_n) \equiv \frac{1}{Q_n} = \frac{1}{\pi f_n \tau_n}. \quad (3.154)$$

Equation 3.154 allows one to measure loss without having to know the energy in

the system or how much energy is lost. τ represents the characteristic time of decay, or how long it takes the amplitude of the oscillation to fall by a factor of e . Q_n is the quality factor of the n th mode, a quantity that scales directly with decay time and mode frequency.

For further intuition, this can be derived from first principles. Consider a transfer function for a mechanical oscillator with damping [42],

$$G(f) = \frac{k}{k - m(2\pi f)^2 + i2\pi f b}. \quad (3.155)$$

This can be rearranged to make its dimensionality, or lack thereof, more obvious and the last term of the denominator can be replaced with a generic function of frequency $g_d(f)$,

$$G(f) = \frac{f_0^2}{f_0^2 - f^2 + i g_d(f)}. \quad (3.156)$$

Q can be defined as the ratio of the maximum amplitude at the resonance peak in the transfer function to the value of the transfer function well below the resonance,

$$Q = \frac{f_0^2}{g_d(f_0)}. \quad (3.157)$$

Since damping is proportional to velocity, this implies

$$Q = \frac{2\pi f_0 m}{b}. \quad (3.158)$$

The time domain definition of Q can also be illuminating. The oscillator has an impulse response of

$$g(\tau) = e^{-\tau/\tau_0} \frac{f_0^2}{f_d} \sin(2\pi/f_d \tau). \quad (3.159)$$

In this case, Q is the number of radians of oscillation it takes for the amplitude of the oscillation to fall by $1/\sqrt{e}$,

$$Q = \pi f_0 \tau_0. \quad (3.160)$$

By exciting the vibrational modes of the system and observing the decay in the sample's oscillation amplitude, one can measure the time of decay τ_n . Furthermore, by Fourier transforming the time-series measurement of position, the mode frequency is also obtained. With this information, using equation 3.154, one has all the tools

necessary to determine the loss of the mode. Using the loss of many modes, one can attempt to rigorously characterize the expected thermal noise of the material were it to be used as a test mass coating; more details of this process are discussed in sections 2.1.2 and 5.3.

3.2 Gentle Nodal Suspension

All of the previously discussed methods of measuring mechanical loss have their own drawbacks. The method of Numata, where two ruby balls are pressed into the center nodes of each face, requires a strict clamp of the sample, which can cause loss due to friction. If the sample is coated, this unavoidably damages the coating. For the welded suspended samples, the user must take great care to avoid damaging the sample during the welding process.

When a cantilever blade is welded to a thick clamp, energy is invariably lost to the clamp even though the size difference between clamp and blade is selected to minimize this energy transfer. This decouples the motion of the blade from the relatively huge clamp [147]. In other similar weld solutions, sample geometry must be chosen to create vibrating modes as independent from the clamp as possible [148].

In these cantilever blade experiments, it could be difficult, sometimes impossible, to determine what portion of the measured loss is due to excess damping of the system holding the resonator. This problem is especially difficult for very low loss materials, when ϕ is on the order of 10^{-6} or lower. Each parameter of the experiment must be altered one by one, and loss measured again and again, in order to characterize the impact of the experiment on the loss. Additionally, each mode must be measured one-by-one. Altogether, this was a time-consuming process.

A Gentle Nodal Suspension (GeNS) gets around this issue by minimizing the damping experienced by the resonator. A thin disk resonator, generally on the order of 1 mm thick, is balanced in equilibrium on top of a spherical surface. This surface is selected to be an ultra low loss material such as fused silica, sapphire, or silicon. This sample suspension technique to determine its mechanical loss was pioneered by Cesarini *et al* [4]. A picture of the suspension in action is provided in Figure 23.

Once the resonator is balanced, the GeNS works exactly the same way a welded suspension or a clamped suspension does. First, the vibrational modes of the balanced

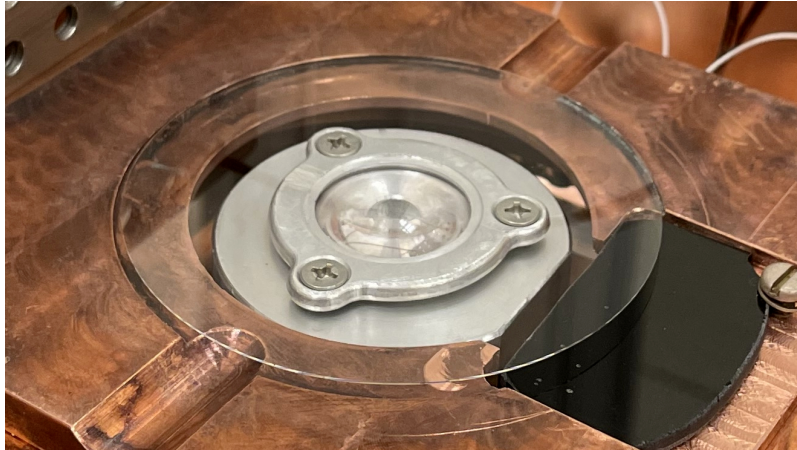


Figure 23 : The Syracuse University Cryo-GeNS nodal support. Pictured is a 3 inch fused silica test sample balanced on a 25mm diameter \times 30mm focal length silicon plano-convex lens, provided by Edmund Optics. The black glass is used to dump any light that transmits fully through the sample. For bare silicon and AlGaAs-coated silicon samples, essentially zero light is transmitted, so the black glass is only necessary when testing the fused silica samples.

sample are excited via a comb exciter. The subsequent ringdown of these modes are measured over time by an OpLev. The laser of this OpLev is reflected off a spot on the sample close to the edge, and is then directed onto a Quadrant Photodiode (QPD). The time series position of the laser on the QPD can be Fourier transformed, revealing the resonant mode peaks in frequency, where the ringdown can be observed. A diagram of this process is depicted in Figure 24. One downside of using a GeNS is that any modes with movement at the nodal support are strongly damped by friction with the support, and are unable to be measured [4, 149]. Additionally, GeNS measurements often record higher loss than welded suspensions, but are an attractive option due to their repeatability and minimal risk of damaging the sample.

At Syracuse, the Cryo-GeNS has one additional instrument before the OpLev to increase the sensitivity. Prior to making contact with the excited sample, the laser is passed through two lenses that act as a telescope, enabling minimization of the beam width at the QPD. This increases the sensitivity of the GeNS, since a perturbation to a beam of smaller width will manifest as a comparatively greater change in power on the QPD quadrants as compared to the same perturbation on a large beam width [149].

The stability of a thin disk balanced on a sphere can be determined analytically.

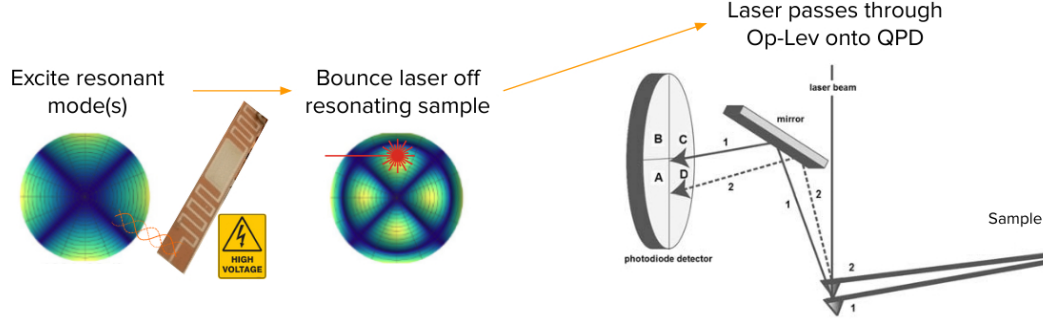


Figure 24 : A diagram depicting the sample excitement and observation using an optical lever. First, a comb exciter rings up the resonant modes of sample. Next, a laser is reflected off the surface of the resonating sample. Lastly, the laser is passed through an optical lever into a QPD, where the Fourier Transform of the laser position will show the mode amplitudes decaying over time.

Assuming the coefficient of static friction is strong enough to prevent slipping, that supporting sphere diameter (D) is larger than disk thickness (t), and defining θ as the angular position of the disk with respect to the horizontal plane, the expression for potential energy is given by

$$V(\theta) = Mg \left[\frac{D}{2} \cos\theta + \frac{D\theta}{2} \sin\theta + \frac{t}{2} \cos\theta \right] \quad (3.161)$$

where M is the mass of the disk and g is the local gravitational field of Earth. The range of stability for θ in such a potential is

$$\theta \approx \pm \sqrt{3 \frac{D-t}{t}}. \quad (3.162)$$

This light contact at a single point, combined with a complete lack of restraints holding the sample in place, is where the “gentle” part of Gentle Nodal Suspension (GeNS) gets its name from. The spherical structure, generally a lens, supporting the sample at its central node explains the rest of the name. In Cesarini’s GeNS, the sample is placed onto the support by hand; the region of stability is large enough for this to be done without much trouble [4].

The surface roughness of the only support point can be investigated beyond just by eye or microscope. When the support is damaged, it was found that the rolling mode of the sample does not oscillate with the same frequency on the measured orthogonal axes and the laser spot creates open Lissajous’ figures. No such behavior

was observed on the easily procured highly polished optical sapphire hemispheres [4].

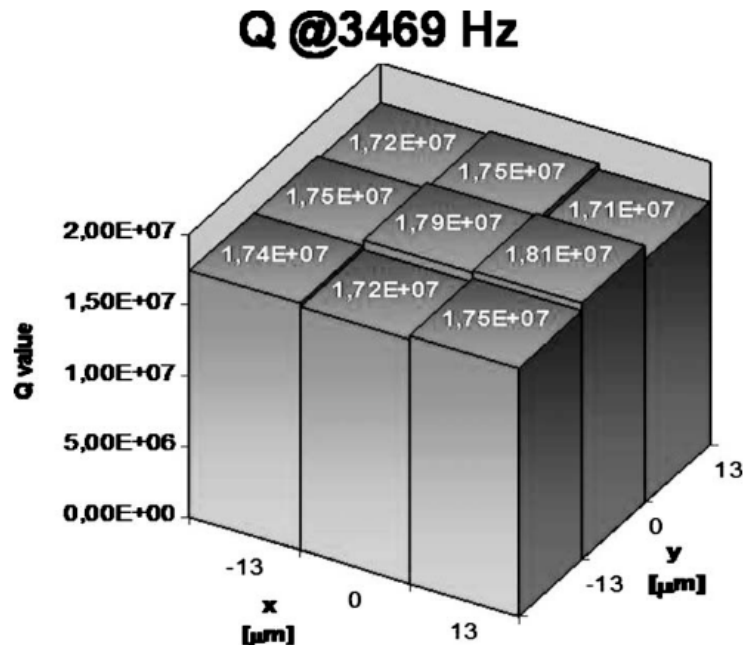


Figure 25 : Differences in measured Q for the first butterfly mode of their fused silica sample. Each bar represents a different centering point of the sample on the nodal support. The x and y axes are in units of μm , while the z axis is the unitless Q . Image credit Cesarini *et al* [4].

It was found through a combination of finite element analysis and through tests of samples with known low ϕ (high Q) that the resonance of the support structure and differences in centering of the sample on the support did not impact the measured loss. A fused silica disk, 3 mm thick and 75 mm in diameter, was annealed in a way that mirrored the anneal process on another fused silica rod, previously annealed and loss measured by Penn [150]. Cesarini's GeNS produced loss results that agreed with Penn's findings, and that the measured loss was not dependent on the centering of the disk, as is shown in Figure 25 [4].

Since Cesarini *et al*'s ingenious invention of the GeNS, many other labs within the LVK collaboration have used the system to measure loss of various materials [59, 82, 149, 151]. Today, the GeNS is known to be one of the best methods to reliably measure loss while minimizing damping due to the environment.

3.3 Extracting Coating Mechanical Loss From Substrate-Coating System Loss

Although previous discussion on the origin of the GeNS discussed measurements on uncoated fused silica disks, the focus of both this thesis and the physicists working on improving the test masses recently have been on the test mass coatings [59, 82, 149, 151]. Specifically, the high index of refraction coating has been the most important subject of recent work due to it being the most significant source of thermal noise in the detector today [16].

This begs the question, how is the loss of the coating disentangled from the loss of the coating-substrate system? Readers might additionally recall the derivation of bulk and shear loss that led to equation 2.116, the power spectrum of the thermal noise in a coated substrate. How are these two loss angles measured via an experiment that can only measure a single total loss?

3.3.1 The Dilution Factor

Earlier in this chapter, there was a discussion on the relationship between the loss angle ϕ and the energy dissipated in a single cycle of an oscillatory process. That section concluded by stating that to find the loss of a system it was unnecessary to know the total energy of the system or the energy lost provided the amplitude of the oscillation could be measured over time. The ratio of energy lost to total energy was all that was necessary, their total values were irrelevant.

A very similar trick can be used to extract coating and substrate loss from the total measured loss. Since loss mechanisms add linearly weighted by the energy contained within that mechanism, the total loss can be written as

$$\phi_{\text{total},n} = D_{s,n}\phi_{s,n} + D_{c,n}\phi_{c,n} \quad (3.163)$$

where the $D_{i,n}$ are known as the dilution factors of the n th mode of the substrate and coating, subscripts s and c respectively. These dilution factors are defined as simply the ratio between coating/substrate elastic energy and total system elastic energy [152], and are dependent on the mode-shape [153], hence the subscript n to denote a

specific mode,

$$D_{i,n} \equiv \frac{E_{i,n}}{E_{\text{total},n}} \quad (3.164)$$

$$D_{s,n} + D_{c,n} = 1.$$

These dilution factors can be determined analytically via elasticity theory or through finite element (FE) analysis. Li [154] found an interesting relationship between the dilution factor of the coating and the frequency shifts of the resonant modes after a sample is coated on both sides,

$$D_{c,n} = 1 - \left(\frac{f_{s,n}}{f_{\text{total},n}} \right)^2 \frac{m_s}{m_{\text{total}}}. \quad (3.165)$$

Due to the fact that the samples analyzed in this work are only coated on one side, the FE model was employed to calculate the dilution factors. Using COMSOL [13], the strain energies inside the coating and substrate are calculated. Since COMSOL is an expensive software tool that also requires training to use effectively, the FE modeling was carried out by collaborators, Simon Tait of the University of Glasgow and Steve Penn of Hobart and William Smith Colleges. By equation 3.164, this yields the dilution factors of equation 3.163.

This leaves just two unknowns in equation 3.163, the substrate loss and the desired coating loss. By measuring the silicon samples prior to coating, substrate loss can be determined [82, 144], enabling coating loss to be determined. Rearranging equation 3.163 makes this abundantly clear,

$$\phi_{c,n} = \frac{\phi_{\text{total},n} - (1 - D_{c,n})\phi_{s,n}}{D_{c,n}}. \quad (3.166)$$

Armed with the numerically simulated value of $D_{c,n}$ and the measured losses of $\phi_{\text{total},n}$ and $\phi_{s,n}$, one can determine the loss of a coating material independent of the substrate or system it is bonded to.

3.4 Building the Cryogenic Gentle Nodal Suspension

Before any data could be measured, the Cryo-GeNS had to be built. It was the author's responsibility to turn a new, completely empty lab into a productive one, which included a laundry list of various tasks, construction, and purchasing. In order

to illustrate the rigor that was taken to ensure the high data quality of the Cryo-GeNS, it is relevant to highlight the step-by-step process taken to build such a system.

Although the ultimate goal of this project is to measure loss over a wide range of temperatures below 300 K, the work to do so can broadly be classified into two categories: room temperature and cold temperature. As will be explored in the coming sections, installing a room temperature GeNS system is not trivial. Keeping the functionality of the GeNS at 12 K is an added challenge that can only be addressed once one has a working room temperature GeNS system.

3.4.1 Before Cryostat Delivery

Prior to any operation, cryogenic or not, there was a large amount of infrastructure that needed to be installed. Additionally, in the lead up to the cryogenic vacuum chamber delivery in the summer of 2021, a number of problems were identified when it came to migrating a room temperature GeNS to a cold temperature environment. But before anything else could be done, there needed to be a table to put the chamber on.

The first order of business was to procure a floating optical table and a wall mount for the Cryo-GeNS system. The chamber holding the sample and the nodal support would sit on the table, while the coldhead, where compressed helium would be cycled in and out of the system for cooling, would sit directly next to the table on a wall mount. This is pictured in Figure 26. Critically, the bellows connecting the coldhead and the sample chamber cannot be disconnected and had to be installed simultaneously. Therefore, even though the liquid helium cooling system was not necessary for room temperature operation, the wall mount holding it needed to be installed before the vacuum chamber holding the GeNS could be delivered.

Once the table was installed and hooked up to building air for seismic isolation, a steel frame ISO 6 cleanroom was installed around the optical table, with an air filter and light installed in the ceiling of the enclosure. The legs of this frame are the large vertical bars at the corners of the table in Figure 26. Additionally, a floating platform was placed inside the cleanroom to hold the laser power and other optics, resonators, and cleaning supplies above the optical table.

Once the table and wall mount were in place, the ambient ground noise traveling through them was measured by placing a seismometer on the table and mount. The

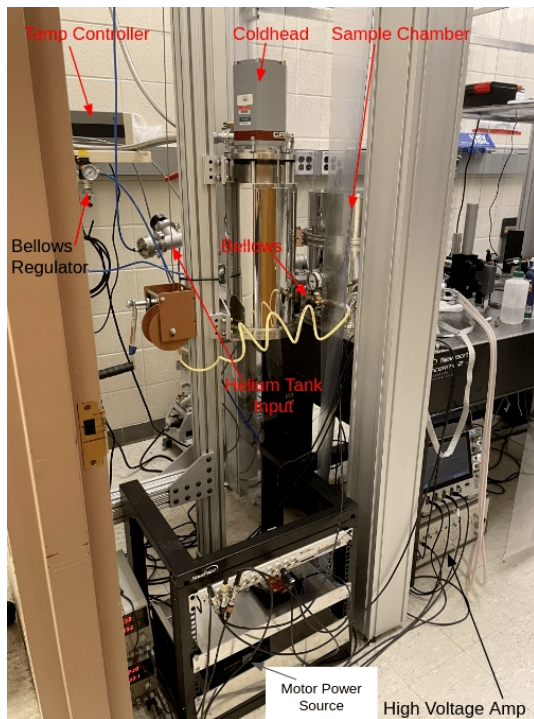
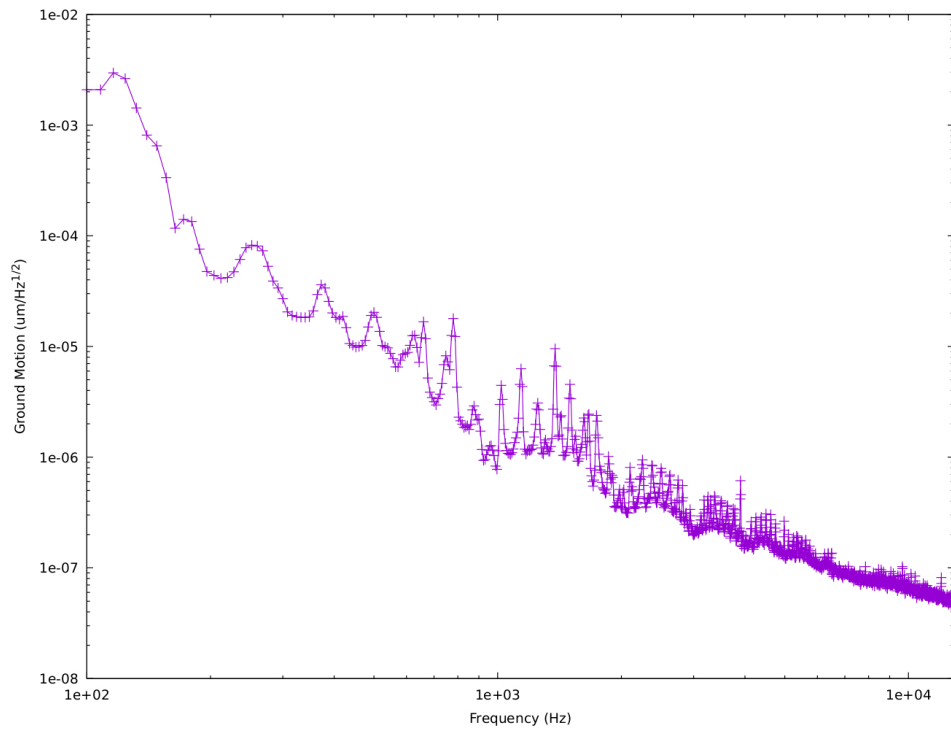


Figure 26 : A view of the Cryo-GeNS from the lab entrance. Central to the picture is the coldhead, where compressed helium is pumped in and cycled through the system. Other important equipment is also labeled.

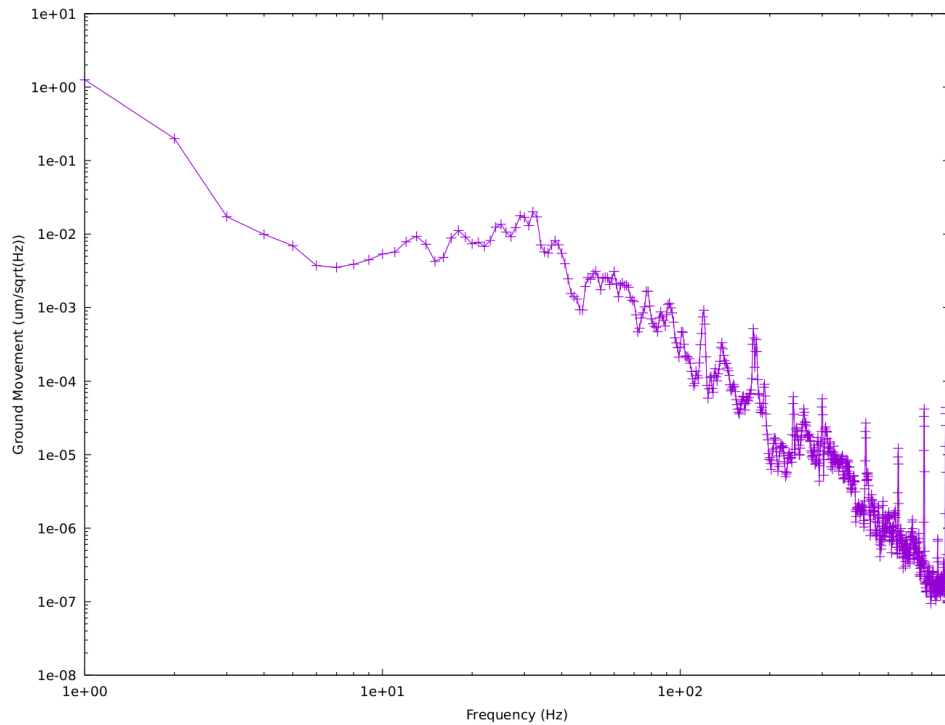
noise of the floor itself was also measured, and compared with previous data from 2010 taken on the same seismometer, to ensure that the results of seismometer calibration and data analysis were reasonable. The amplitude spectral densities are shown in Figures 27 and 28. See section 1.3 for an explanation on the units of the y-axis.

A shrewd reader might notice the similar magnitude of ambient noise from seismic motion between the optical table and the wall mount; there are two reasons for this. First, the optical table itself is designed to mitigate noise at the lower frequencies where seismic motion is more significant. Second, it was determined after installation and testing that the mechanism used by the table to maintain a level float was not properly judging the table's position. This was fixed before loss data was recorded.

Importantly, even when operating in a faulty manner, the noise of the optical table and wall mount is completely insignificant at relevant frequencies. These frequencies would span the range of resonant frequencies of the samples to be measured. The frequency range we wish to be sensitive to is between 390 Hz and 30 kHz. As can be seen in Figures 27 and 28, the seismic motion at these frequencies peaks at roughly



(a) Optical Table Seismic Data



(b) Wall Mount Seismic Data

Figure 27 : Ambient ground motion of the top of the optics table (a) and the wall mount (b). Although they differ little in magnitude, this is unsurprising since the table is designed to mitigate noise at lower frequencies. Additionally, when the seismic noise of the table was measured, the table was not configured for optimal mitigation. This error was fixed before loss data was recorded.

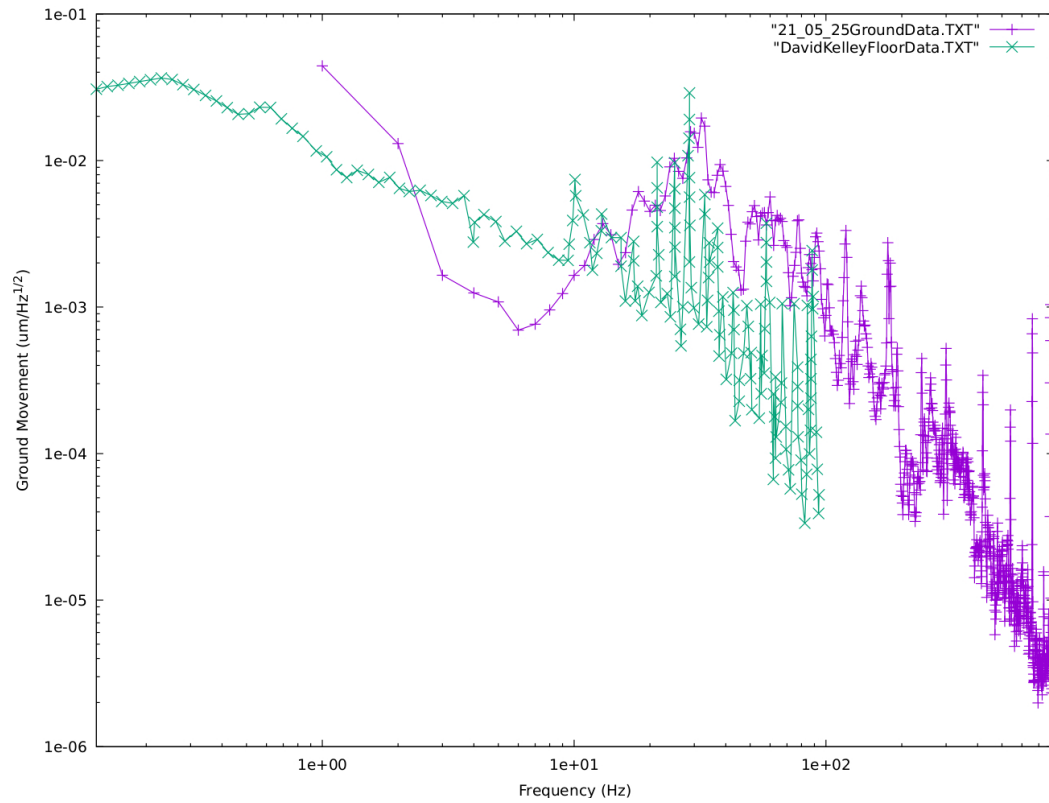


Figure 28 : Comparison of seismic noise of the lab floor. The green line was taken by David Kelley in 2010, while the purple was recorded by the author in 2021. Discrepancies can be explained by the fact that these were taken in two separate labs a decade apart, though they do share a wall and are on the same floor (sub-basement) of the physics building.

$5 \times 10^{-5} \mu\text{m}/\sqrt{\text{Hz}}$. This peak occurs at the lowest frequencies of concern, and as frequency increases, the level of seismic noise drops precipitously. At the highest frequency resonant modes, the seismic motion is lower than $1 \times 10^{-7} \mu\text{m}/\sqrt{\text{Hz}}$.

Since the loss is measured via ringdown by a laser beam, perhaps the most relevant experimental parameter to compare to the seismic motion would be the beam spot size. Ground motion is much too small to impart noise directly into the resonator or alter the OpLev behavior, which is dependent on the angle of the resonator where the beam hits it and is not nearly as sensitive to length changes due to vertical ground motion. The beam spot size on the QPD was tailored to be as small as possible to maximize accuracy of the OpLev; two lenses were installed in the path of the input beam to ensure a beam width of $300 - 400 \mu\text{m}$ at contact with the QPD.

The next installation project was the Data Acquisition (DAQ) system. A PCIe-6363 X Series DAQ was procured from NI, along with a desktop to run LabVIEW [155], the software that sends and receives signals through the DAQ. The 6363 DAQ has a sampling rate of 2 MS/s (mega samples per second), sufficient sampling to characterize the highest resonant frequencies of the sample.

Simultaneously, a 2 mW power linearly polarized HeNe laser from ThorLABS was bought, along with the optics needed to get the 632.8 nm wavelength light from the laser to the sample and out to the QPD. Additionally, the noise coming from the QPD and the corresponding electronics boards needed to be measured. There are two circuit boards necessary to operate the QPD; one to house the QPD itself and another to carry out the necessary math on the four outputs of the QPD to return an X and Y position. This was done using an SR-785 to obtain a transfer function for the QPD boards. Using the transfer function, the voltage change of the powered QPD boards were measured across a relevant frequency range, both with the QPD installed and without. When the QPD was installed, the board was sealed in darkness such that the QPD was in a zero signal state.

With the voltage noise in hand, the trans impedance function of the board was used to convert voltage coming out of the board to current coming out of the QPD

$$I_{\text{QPD}} = \frac{V_{\text{out}}}{(43\text{k}\Omega)T_m} \quad (3.167)$$

where T_m is the magnitude of the transfer function. Lastly, the spectral response of

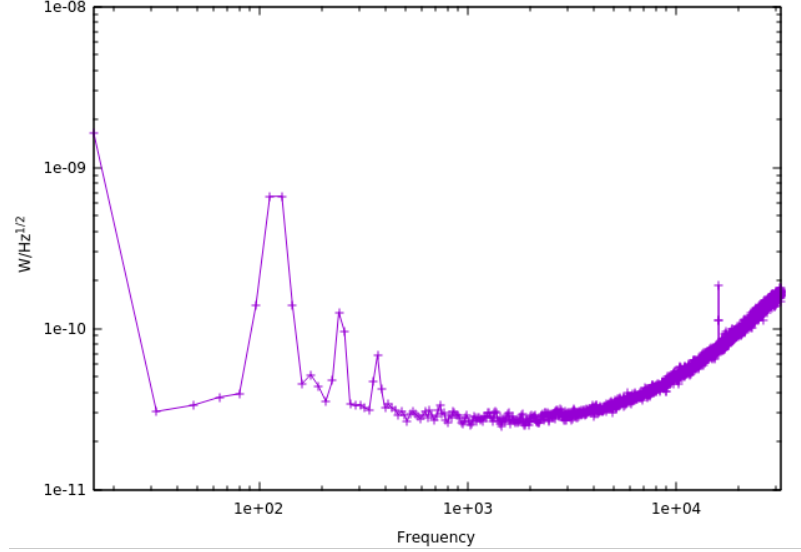


Figure 29 : QPD noise depicted as an equivalent power fluctuation on the diode. The voltage noise measurement discussed has been converted to an equivalent power change on the QPD using equations 3.167 and 3.167, hence the y-axis units of $W/\sqrt{\text{Hz}}$.

the QPD at 632 nm enabled us to convert the current noise coming out of the QPD to an equivalent power change by a laser on the face of the QPD. The spectral response of the Hamamatsu QPD used is 0.45 A/W at 632 nm. With this knowledge, the conversion to equivalent power change from the laser on the QPD face is trivial,

$$P_{\text{noise}} = \frac{I_{\text{QPD}}}{0.45 \text{ W/A}}. \quad (3.168)$$

The results of this test are shown in Figure 29 and they match the noise levels achieved by prior GeNS experiments [149]. At first glance, this plot depicting an equivalent power change on the QPD from the electronics noise of nano-Watts or lower feels guaranteed to be low enough to measure the length changes of the laser on the QPD from the OpLev. Although this could not be tested definitively until samples were installed, it is prudent to calculate how much disk angular motion this level of noise corresponds to.

One can assess the equivalent radial motion of the disk that the electronics noise of Figure 29 will mimic, and therefore mask. To determine the power change on the QPD caused by an angular shift, one must calculate linear distance r traversed by the center of the laser on the QPD. Due to the small angle involved, this is given by

the simple formula $r = d_{\text{OpLev}}\theta$, where $d_{\text{OpLev}} = 2$ meters is the distance of the optical lever and θ is the angular change due to disk surface motion.

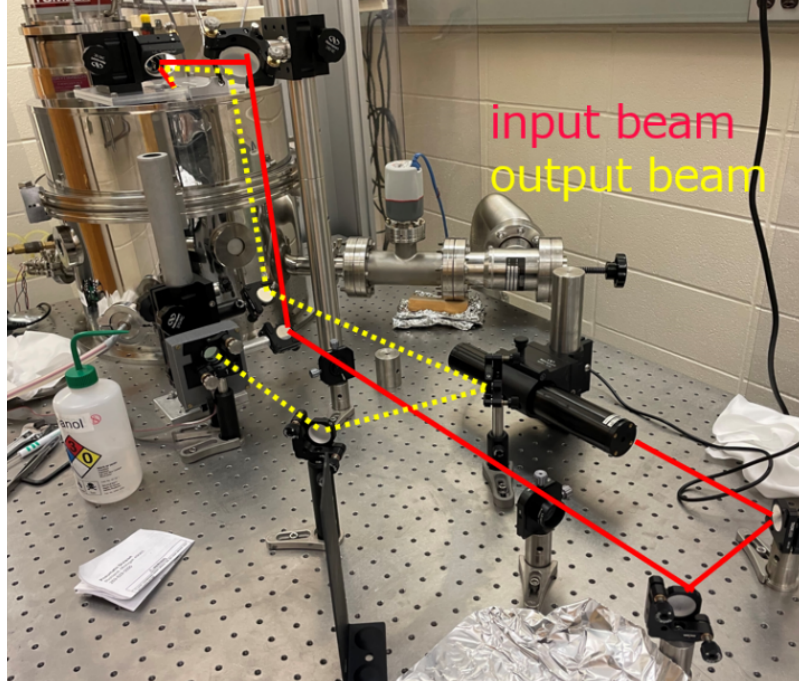


Figure 30 : The optical lever of the Cryo-GeNS. The telescope is composed of the two lenses on the table between the laser and the QPD, and is used to minimize beam width on the QPD.

Armed with the knowledge of how much the laser position shifts based on the angular change and an assumption of the direction of the shift, one can calculate roughly how much position change such a level of power noise will simulate in an individual photodiode of the QPD. For this calculation, it is assumed that the distance traversed by the center of the laser is directly away from the photodiode of interest, towards the center of the diode diagonally opposite. Additionally, the beam width of the laser is taken as $w_0 = 300 \mu\text{m}$, the low end of the laser spot size in the experiment. The beam power is also taken from the parameters of the experiment; the amount of power hitting the QPD is roughly $100 \mu\text{W}$.

With these assumptions and parameters, the power change can be reasonably estimated by calculating the laser power on the QPD before and after the position shift. Assuming a circular Gaussian beam and perfect centering, the power on the QPD before the shift is simply a quarter of the total power on the QPD, $25 \mu\text{W}$.

After the laser position shift, the calculation becomes a little more involved. However, a lower limit on the power change can be found by solving a simple Gaussian integral. The expression for power at a radial point from the center of a Gaussian beam is given by

$$I(r) = I_0 e^{-2r^2/w_0^2}, \quad (3.169)$$

where I_0 is the intensity at the beam center and w_0 is the beam width. By integrating the above equation over r from 0 to infinity and dividing by four, one recovers the 25 μW power on the singular quadrant of the QPD prior to the shift.

Such an expression can be used as a lower limit to estimate the minimum laser position shift from the noise by simply altering the limits of integration to be from $r = d_{\text{OpLev}}\theta$ to infinity. This simplification is a lower limit because it neglects the narrow bands of laser power on the boundaries between the photodiode of interest and the two neighbors it shares a border with that are completely lost when the laser changes position. Therefore, the exact angular change simulated by the noise will be lower in magnitude than this calculation.

However, if this upper bound of laser position shift due to power fluctuations is found to be below the anticipated laser position shift needed to resolve a low amplitude mode, then it is possible to progress without knowing exactly how the power will evolve as the laser position is altered. The knowledge that the anticipated laser position change sits above that simulated by the noise is sufficient to instill confidence in the electronics.

Carrying out the integral for the centered laser yields $P_c = \frac{\sqrt{\pi}}{16} I_0 w_0$ where P_c is the power when the laser beam is centered. For the off-center integral, one finds the following result for off-center power P_{oc} ,

$$P_{oc} = \int_{d_{\text{OpLev}}\theta}^{\infty} I(r) dr = P_c \left(1 - w_0 \text{erf} \left(\frac{\sqrt{2}(d_{\text{OpLev}}\theta)}{w_0} \right) \right). \quad (3.170)$$

Note that erf is the error function. Since the error function is intractable with variables, one can plug-in a minimum angular change detectable from prior GeNS experiments [156], $\theta \approx 10^{-7} \text{rad}/\sqrt{\text{Hz}}$. In this case, we have the following for the value of P_{oc} ,

$$P_{oc} = P_c(1 - 0.127w_0) = 24.9990 \mu\text{W}. \quad (3.171)$$

The difference between P_c and P_{oc} , 1×10^{-9} W, is the power change that must be resolved. At 8 kHz, where this lowest limit on the lowest amplitude mode is calculated, this power change sits about ten times above the noise of the electronics. Therefore, the sensitivity of the QPD is sufficient to sense the power change from the smallest expected angular motion of the disk; indeed this was found to be true once the Cryo-GeNS was operational.

With the optical table, wall mount, optics, and electronics all ready, the coldhead and sample chamber were ready for delivery. This is relevant to a room temperature operation of the Cryo-GeNS since even operation at room temperature was to be conducted inside the sample chamber using the same apparatus that would eventually be cooled down. Before delivery could be completed, there was more work to be done in conjunction with Cryomech [157], the designer and manufacturer of the helium compressor system and the sample chamber, pertaining to the vertical stage that captures and balances the sample.

Although there were a number of minor modifications as compared to a room temperature GeNS, the largest and most complex was that pertaining to the raising and lowering of the sample. Having the ability to capture and replace the sample without breaking vacuum has a couple benefits, but for the Cryo-GeNS the most benefit comes from the ability to rapidly achieve thermal equilibrium in the sample when changing temperature.

Room temperature GeNS operation at Syracuse was previously conducted with a DC motor driving a vertical stage [156], however such a motor would not operate below roughly 250 K. Therefore, a new method of raising and lowering the sample had to be found. It was decided that the only solution that could provide the range of motion necessary was a stepper motor through Empire Magnetics [158], a company that has designed motors for satellites and rovers. The sample chamber, when fully cooled, is a similar environment to the freezing vacuum of space, leading to the conclusion that Empire's stepper motor would suffice.

However, the only available motors were rotary stepper motors, meaning the angular motion of the motor would have to be converted to linear vertical motion of the stage, and the steps of the motor would have to be translated to minimal linear motion per step. To accomplish this, a number of designs were proposed. Ultimately, it was decided to go with a rotary chain design proposed by Brent Zerkle of Cryomech

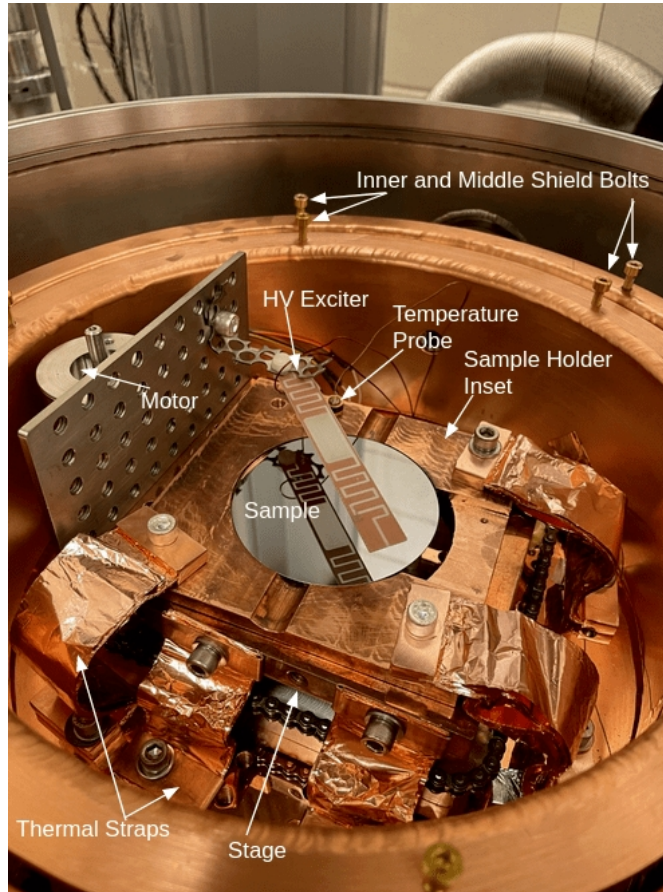


Figure 31 : The inside of the sample chamber. Various important components are labeled. The chain that is driven by the motor can be seen underneath the thermal straps and stage on the bottom and right side of the apparatus. The stage, sample holder insets, and thermal straps are all composed of 101 oxygen free copper. These pieces were also baked at 480° C in a vacuum furnace to increase their thermal conductivity.

[157]. The stage along with the motor is pictured in Figure 31.

In order to minimize the noise from the discrete steps of the motor, the stage was designed to move as little as possible per step, providing smooth placement of the sample onto the nodal support. It takes the motor 200 steps to rotate through a full 2π rotation, meaning each step is $\pi/100$ radians or 1.8° . In one rotation, the stage was designed and found through testing to move 0.9 mm, corresponding to a step size of just $4.535 \mu\text{m}$. This was deemed sufficiently small to damp whatever noise might arise from the discontinuous movement of the motor. Later testing would show that the sample is placed in a relaxed state, and noise from the motor is completely eliminated by cutting off power to it.

3.4.2 Achieving Room Temperature Operation of the Cryo-GeNS

With the stage built, the motor installed, and everything tested at Cryomech, the coldhead and sample chamber were finally delivered and installed. It was deemed prudent to first assess the performance of the Cryo-GeNS at room temperature, where any noise from the helium compression system attached to the sample chamber would be absent.

Before such room temperature assessment could be done, a number of additional components of the GeNS experiment needed to be built. Chief among them was the vacuum system. In order to minimize the effect of gas damping on the lowest loss modes, it is necessary to reduce the atmosphere inside the chamber well below 10^{-4} torr [4, 149]. This process took some months of work, and initially had a more complex design with multiple pneumatic valves, but was finally completed. At room temperature, the chamber vacuum reaches levels of roughly 2×10^{-5} torr.

While the vacuum work was ongoing, two important components of the nodal suspension were being designed and constructed. First, sample holder insets, pictured in Figures 31 and 32, were built to accommodate the roughly half a millimeter or less difference in diameter that can arise from imprecise construction of the substrates. With these mounted on the stage, a slight decrease in sample diameter would not stop the sample from being consistently placed onto the nodal support, while a slight increase of diameter would not restrict a sample from fitting on the stage whatsoever.

The second important component of the suspension system was the nodal support itself. An uncoated, silicon plano-convex lens was procured from Edmund Optics [159], to be mounted on a pedestal below the sample. The lowest and highest vertical positions of the stage with the sample holder inset were calibrated, and a pedestal for the nodal support was built centered between the two vertical positions. A clamp was constructed for the lens at the top of the pedestal, and the pedestal itself was mounted below the center of the sample holder inset.

Upon testing, it was found that the motor reliably placed and captured the sample. Each capture and replacement is consistent enough that the laser, after bouncing off the edge of the sample and propagating through the 2 meter optical lever, usually needs to be adjusted very slightly to reestablish centering on the QPD.

In order to excite the resonant modes of the sample, a comb exciter had to be

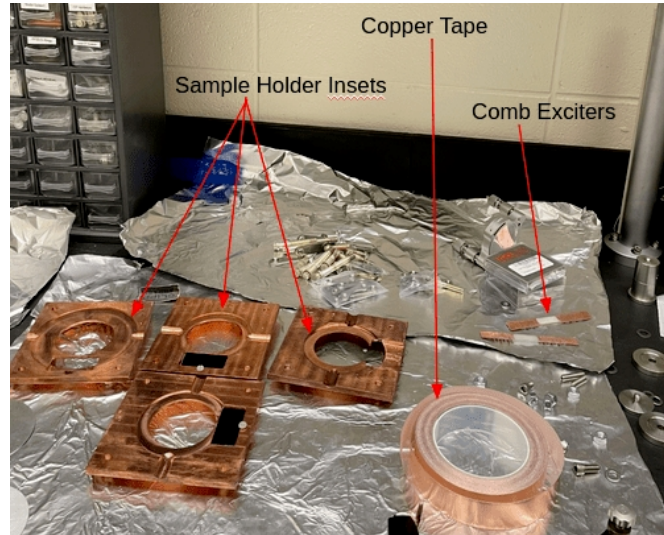


Figure 32 : Four of the sample holder insets along with other Cryo-GeNS equipment. Three insets were made for each sample target diameter of 3 inches and 4 inches, totaling six sample holder insets. One inset had a diameter 30 thousandths of an inch larger than the sample target diameter, another had 30 thousandths of an inch smaller, while the last was exactly the sample target diameter.

machined and connected to a high voltage (HV) source. The comb exciter is pictured in Figure 31 above the sample. The exciter operates by passing a HV white noise spectrum through one side of the exciter, while holding the other at ground. The induced dipoles in the sample interact with the electromagnetic field created by the rapidly oscillating voltage. This effectively imparts a stress onto the sample across the whole white noise frequency spectrum, the energy of which gets pushed into the resonant modes of the sample.

While this work was going on, a complete overhaul of the data analysis software was being performed by Elenna Capote. Additionally, the data collection LabVIEW software written by Steve Penn, called MultiQ, had to be converted to a Windows environment from a Unix one. Using the converted MultiQ, the signals from the QPD are sampled at 22 kHz. The obtained data are then analyzed by a time-domain analysis method which applies a digital lock-in amplifier and filtering to isolate each excitation peak. A finite element analysis (FEA) simulation provides a list of modes and frequencies based on the geometry of the sample. Each measured mode is identified by matching it to the FEA. Due to the symmetry of the disk around the suspension point, each mode is quasi-degenerate. To clearly capture each mode in the lock-in analysis, the degenerate peak is removed via notch filtering. After removing

the secondary peaks, the digital lock-in method applies a 2 Hz bandpass filter and heterodyne method to each mode. This analysis method yields the quality factor of each resonant mode ($1/\phi_n$) [160].

The finite element analysis for the fused silica and silicon substrates, and later the AlGaAs coated systems, were first created in ANSYS [161] by the author and Satoshi Tanioka. This gave relatively accurate frequencies for the resonant modes, and allowed identification of modes for data analysis yielding the loss of the substrate and the coated system. Later, more accurate COMSOL [13] models were created by Simon Tait and Steve Penn to calculate the dilution factors, which were used to disentangle the loss of the coating from the loss of the coated system via equation 3.166.

Finally, with the nodal suspension, HV comb exciter, stage, QPD, DAQ, vacuum system, and data analysis software suite all operational, room temperature operation of the Cryo-GeNS could commence. The results of these initial tests are demonstrated in Chapter 4, but it is sufficient here to state that room temperature loss measurements on fused silica were consistent with that of previous measurements in literature and at Syracuse [4, 88, 145].

3.4.3 Achieving Cold Temperature Operation of the Cryo-GeNS

With room temperature operation successful, focus was then shifted onto cold temperature operation. Much of the work needed to get the helium compression system from Cryomech [157] up and running was being done in conjunction with the projects to achieve room temperature operation, beginning with infrastructure for the helium compressor.

The helium compressor, which drives the cooling process, requires both a high voltage source and plumbing for water cooling. Additionally, high and low pressure hoses had to be connected to the coldhead, its motor, the compressor, and the buffer tank, which holds excess helium in case of leaks. Furthermore, the compressor was located in another room due to the huge amount of noise, scientific and actual, created by it. Therefore, the high and low pressure lines had to be ran through the walls and over a distance of roughly 50 meters.

Once that was completed, a CTC 100 temperature controller [162] was integrated into the system by connecting to three temperature probes and two heaters. The

CTC displays and records the temperatures of the pulse tube, where the compressed 4 K helium meets the copper plate that runs into the sample chamber, the sample chamber floor, and the sample holder inset on top of the stage. Additionally, it operates two 5 W heaters located on the pulse tube and on the sample chamber floor.

With the cryostat and CTC now operational, testing of the cooling levels could commence. Prior tests had been carried out at Cryomech, finding that the chamber floor reached a temperature of 6.39 K. Our tests found that it did not get quite so low in the chamber, and further improvements were made to bring down the temperature. These include replacing the fused silica windows into the chamber with better heat conducting sapphire ones, covering the windows with copper tape, and adding additional thermal straps connected directly to the sample holder insets (pictured in Figure 31).

An initial test was conducted to determine the temperature of a fused silica sample on the sample holder inset. The sample chamber floor temperature probe was stuck to the center of the fused silica disk via an adhesive indium foil, and the system was turned on. Due to the low thermal conduction of the fused silica and the lack of thermal conduction to the sample holder inset, the fused silica sample only reached a minimum temperature of roughly 60 K. It was also determined that the thick copper wires carrying the high voltage signal for the comb exciter into the sample chamber were conducting too much heat, and these were replaced with much smaller and less conducting manganin wire.

The high temperature of the fused silica sample was assumed to be due solely to its thermal properties, so a subsequent test was conducted when the crystalline silicon substrates arrived. Disappointingly, it was discovered that the silicon samples only reached a minimum temperature of 30 K.

This is when the previously discussed improvements to the sample chamber were made. The critical addition was the incorporation of the thermal straps onto the top of the sample holder inset. Prior to this upgrade, the sample holder inset had minimal thermal contact with the stage, and subsequently the sample chamber floor. With this fixed, the silicon samples nearly perfectly mirrored the temperature of the chamber floor until the coolest temperatures. At the lowest temperature achieved, the floor sat around 11.3 K, while the sample was 12.1 K. By 20 K, the sample and chamber returned to within tens of mK of one another.

Furthermore, testing of motor operation of the stage at these coldest temperatures were successful. The samples were placed onto the nodal support and recaptured reliably. Centering of the laser onto the QPD after reflecting off the sample was also reproduced consistently after each placement onto the nodal support. It was in these tests at temperatures below 20 K that it was discovered that the motor dumps a noticeable amount of heat into the system, though this is quickly dissipated by cutting power to the motor.

With the knowledge that the samples were reaching the desired minimum temperature, that the motor could drive the stage at the coldest temperatures, and that the Cryo-GeNS could reproduce room temperature loss measurements, data collection on the crystalline silicon substrates and the AlGaAs coatings could commence.

Chapter 4

Cryogenic Multi-Modal GeNS: Data Replication

As a definitive test of the cryogenic gentle nodal suspension's (Cryo-GeNS) efficacy, it was deemed prudent to replicate previous loss measurements across the whole temperature range. Data was initially taken at room temperature on fused silica substrates, a material that has had its loss extensively studied by the coatings research group at Syracuse and in the wider community [4, 141, 145, 163, 164]. Data from the Cryo-GeNS on this substrate could be easily compared, to both Syracuse room temperature GeNS results and that of other loss experiments. Once accuracy at room temperature was verified, the same test of fused silica could be done at cold temperatures. This chapter begins by detailing the results of these successful tests of the Cryo-GeNS.

Following these assessments, the next step was to measure the crystalline silicon substrate that would hold the AlGaAs-GaAs multilayer coating. By measuring the silicon substrate across the whole temperature range, one simultaneously verifies the cold temperature performance of the Cryo-GeNS by comparing to previous data [82] while also recording data necessary to decouple the coating loss from that of the coating-substrate system via equation 3.166. Once substrate data is recorded, analyzed, and found to agree with literature, loss measurements of AlGaAs at cold temperature can commence. This chapter closes with a presentation of the crystalline silicon substrate loss data.

4.1 Room Temperature Replication: Fused Silica

As was discussed in Chapter 3, the Cryo-GeNS performance was first tested at room temperature. Fused silica was deemed the best material for this initial examination, as it was readily available and had been measured extensively both at Syracuse and by the wider community [4, 141, 145, 163, 164]. The planned substrate for the coating, crystalline silicon, is known to have extremely high levels of loss at room temperature due to thermoelastic loss, and so was not selected for testing at this time. Thermoelastic loss, in general and as pertains to the crystalline silicon substrate, is explored in detail in section 2.1.3.

The room temperature test was a resounding success, producing loss measurements with quality factors in the tens of millions, as expected from previous work. The most striking comparison can be made with the room temperature GeNS at Syracuse. Figure 33 shows a direct comparison between ringdowns made in the two systems. As a reminder, loss angle and quality factor are very simply related, $\phi = 1/Q$.

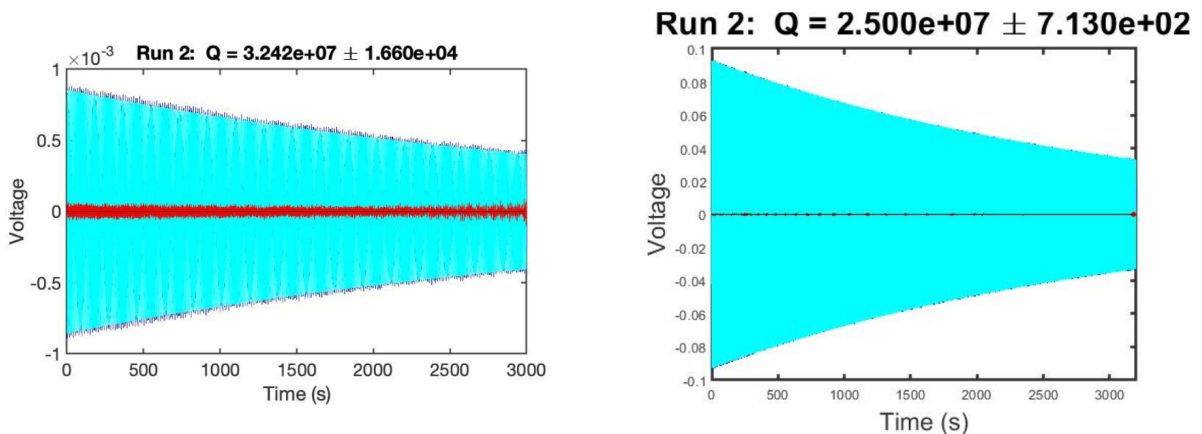


Figure 33 : A comparison of a ringdown of mode 3 ($m = 0, n = 3$) measured in the room temperature GeNS (left) and the Cryo-GeNS (right). Surprisingly, the residuals (red lines) between the fit and recorded ringdown appear significantly lower in the Cryo-GeNS, suggesting this mode has a cleaner ringdown in the Cryo-GeNS. This is probably due to a higher amplitude of oscillation by the mode in the Cryo-GeNS.

Although the loss measurements, $Q = 32$ million in the room temperature GeNS and $Q = 25$ million in the Cryo-GeNS, aren't in perfect agreement, this type of spread is consistent between individual measurements. These findings reflect those of all the other measured modes for this test; the Cryo-GeNS and room temperature GeNS

measured quality factors were always close to each other.

Unexpectedly, the residuals in the Cryo-GeNS appear to be lower than that of the room temperature GeNS, implying a more perfect ringdown unaffected by noise imparted from the environment. This can be seen in Figure 33 by comparing the magnitude of the residual, plotted as the red line, between the room temperature and Cryo-GeNS. The most likely explanation is that the excited amplitude of oscillation by the resonant mode is higher in the Cryo-GeNS, and so a similar level of noise would show up as a relatively lower residual on a plot, when in reality the absolute value of the residuals are the same. This hypothesis is supported by comparing the scale of the y-axes of the two plots; the Cryo-GeNS reaches much larger voltages, implying greater oscillation amplitude.

These loss measurements match the level of loss and its variability observed in the first test of fused silica in a GeNS experiment, carried out by Cesarini *et al* [4]. With the comparison to a second GeNS measurement and agreement with cantilever and welded suspension experiments [141, 145, 163, 164], the room temperature operation of the Cryo-GeNS was considered to be accurate. Testing at cold temperature could now commence.

4.2 Replication of Cold Temperature Data: Fused Silica and Silicon

Cold temperature measurements in the Cryo-GeNS were first taken on fused silica thin disks, similar to the room temperature measurements. There are two reasons for this. First, they were on hand while the crystalline silicon substrates had yet to be delivered. Second, there was also literature at cold temperature for fused silica that could provide a direct comparison [164].

In these early tests, there were two restrictions on how low a temperature that measurable data could be found. First, the sample chamber was not yet upgraded to the form as pictured in Figure 31. Most significantly, the thermal straps connected to the sample holder inset had not yet been installed. This meant that the silica sample could not be cooled below 60 K.

However, this was inconsequential due to the second restriction, an inability of the Cryo-GeNS to measure extremely high loss ringdowns. Indeed, this is reflected

in the data of Figure 34, where below 110 K it is impossible to record the ringdowns, they damp out too quickly. As such, there is no data below this temperature.

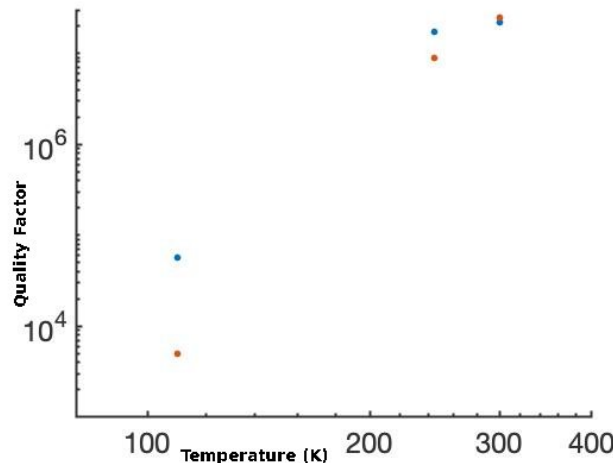


Figure 34 : Two measurements of the quality factor Q of fused silica from 110 K to 300 K for the first mode. The larger relative spread in the data at low Q , or high mechanical loss ϕ , reflects the greater uncertainty that comes with measuring short ringdowns.

Comparing this result to the more complete data set published by Schroeter *et al* [164], one finds that they are in a reasonable level of agreement. Most importantly, the data recorded at 110 K matches that found by Schroeter.

With this rough verification of cold temperature operation, the 3 inch diameter, 1 mm thick fused silica substrate was replaced by a 4 inch diameter, 500 μm thick, double side polished, high-purity silicon wafer procured through Ultrasil LLC [165]. These wafers would become the sample substrates for the coating we wished to measure the cold temperature mechanical loss of. The crystal orientation of the samples are $\langle 100 \rangle$, and their resistivity is more than 10 k Ω cm. One of these silicon samples is pictured in Figure 31 being held by the sample holder inset. Crystalline silicon was chosen as a substrate material for its very low loss at cold temperatures between 12 K and 140 K.

When recording ringdown observations, multiple modes were followed through the temperature range, and two silicon substrates were measured. No significant difference was found in the loss between modes, though their resonant frequencies did differ by approximately 2-3%. This is most likely due to slight differences in their diameters and the exact size and location of the flat cut in them by which the crystal

axes are oriented. The combined losses of the two samples are reported in Figure 35. Since they were relevant for determining the accuracy of the thermoelastic loss models, this data is reported mode-by-mode in Figure 12 of Chapter 2, where it is directly compared to a modeled thermoelastic loss curve.

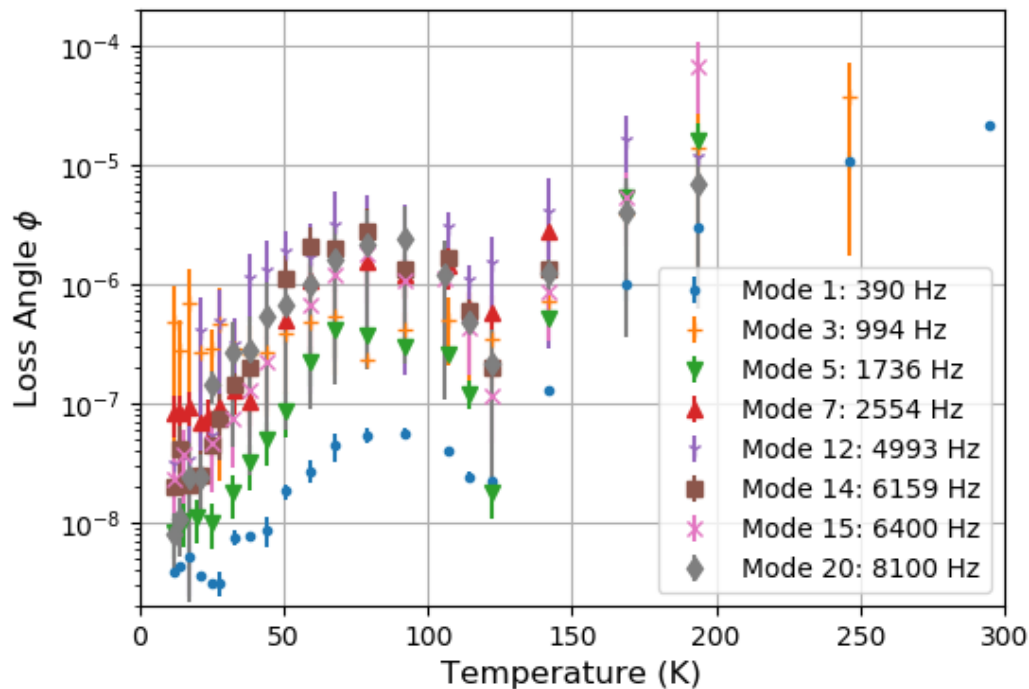


Figure 35 : Loss angle over temperature for eight different resonant modes of a bare, 4 inch diameter, 500 μm thick, crystalline silicon substrate. The shape of each mode is given in table 3.

The results of this full temperature range measurement of loss on the silicon substrates were compared to the same observations made in another cold temperature GeNS by Granata *et al* [82]. This data was in stark agreement, even though our sample was an inch larger in diameter and was about 10% thicker than Granata's 460 μm thick silicon samples. Thankfully, the slight differences in geometry did not significantly alter the levels of thermoelastic loss in the samples, allowing for direct comparison. See section 2.1.3 for more detail about thermoelastic loss.

Further lending confidence to the data is the level of agreement between the measured loss and the modeled thermoelastic loss, as can be seen for all the modes in Figure 12. The most relevant parts of these plots for this argument are the areas

where the thermoelastic loss is the dominant noise source, such as the TE loss peak around 80 K and at all temperatures above 150 K. Although there are some outliers, the vast majority of the points follow the thermoelastic loss trends closely.

The astute reader may ask why the loss of the substrate seems to plateau below roughly 30 K. If thermoelastic loss is the only dominate loss source, loss should continue to fall as temperature does. Similar behavior has been observed before in silicon at cold temperature, and is attributed to surface losses due to impurities, either in the crystal structure or through materials that have fallen onto the sample and been frozen on [97–99]. Due to the reasonably similar levels of loss observed, it can be stated with moderate confidence that surface losses on the substrates are responsible for the plateau in loss below 30 K.

After comparing the loss measured in the Cryo-GeNS to those found by Granata *et al* [82], confidence in the accuracy of the data being extracted by the Cryo-GeNS was high enough to send out the substrates for coating. Specifically, the substrates were to be coated with a material that has shown great promise for the gravitational wave community in addressing coating thermal noise, AlGaAs. The performance of this material at cold temperatures is an open question; understanding it the driving goal of this thesis. Answering this question is of critical importance for achieving the low coating thermal noise demands of current (KAGRA) and next-generation detectors. Furthermore, as was discussed in section 2.2.4, one requires cold temperature data to understand the loss mechanisms of these materials, substrate or coating.

Chapter 5

Cryogenic Multi-Modal GeNS: AlGaAs

With the completion of loss measurements on the bare silicon substrates across the temperature range from 12 K to room temperature, it was time to send them out for coating by Garrett Cole and Thorlabs Crystalline Solutions [166]. As will be discussed in the beginning of this chapter, AlGaAs is a relatively novel material in the gravitational wave community. As such, demand for large area AlGaAs coatings has not existed for longer than a decade. Not only is this work expanding the breadth of available data on AlGaAs mechanical loss at cold temperature, but it also is the first test of 4 inch (10 cm) diameter optical coatings. These are the largest area AlGaAs coatings yet produced [167]. Such assessments of size are critical, as the gravitational wave detectors (GWDs) will require coatings with diameters between 34 cm and a meter [9, 56, 168].

Although the coating has previously been referred to as AlGaAs, this is a slight misnomer. In reality, the coating is composed of multiple layers of alternating gallium arsenide (GaAs) and aluminum-alloyed gallium arsenide ($\text{Al}_x\text{Ga}_{1-x}\text{As}$). The x in the subscript of the AlGaAs nano-layers denotes the doping percentage of Al; for this work $x = 0.92$. For the rest of this thesis, unless otherwise noted, whenever AlGaAs is mentioned it is referring to this specific doping percentage of the material. Additionally, it should be noted that the loss of the coating is the loss of this multilayer stack of GaAs and AlGaAs; neither material is being measured independently. The AlGaAs coatings measured in this experiment were $6.78\text{ }\mu\text{m}$ thick, with 26 alternating

layers of GaAs and AlGaAs comprising the total coating thickness.

The presence of GaAs layers is a necessity, as AlGaAs exposed to open air will corrode, but not an unwelcome one. The GaAs layers have a high index of refraction, approximately 3.38 at 1530 nm [169], while the AlGaAs layers have a lower index of refraction of 2.93 at 1530 nm [169]. This means that AlGaAs could potentially make up both the high and low index of refraction components of an HR stack on a test mass.

This chapter will begin by outlining the brief history of AlGaAs coatings as pertains to the GWD community. Although it will start with work done by those within the LIGO-VIRGO-KAGRA (LVK) collaboration, there is also relevant research that has been done by the precision metrology community in an effort to build maximally precise atomic clocks. Once the backstory is established, the loss of the AlGaAs coating as measured in the Cryo-GeNS will be reported. There will also be some discussion about the implications of the results to close the chapter.

Lastly, a note about terminology moving forward. There are three loss terms that are discussed. The first is the measured loss of the substrate which is dominated by thermoelastic loss, referred to as substrate loss. The second is the measured loss of the coated sample, which is referred to as coated sample loss or coated system loss. The last and most important is the loss of the coating itself, calculated from 3.166 using the two measured losses of the substrate and the coated system. This is called coating loss, and is referred to as such in the proceeding sections.

5.1 GaAs-AlGaAs Multilayer Coating: A Brief History

Monocrystalline multilayers, consisting of alternating GaAs and AlGaAs layers, began being explored as one of the coating candidates for future GWDs about a decade ago [5]. Interest has only grown since then, inspiring further research [6, 136, 137, 139]. AlGaAs coatings have been found to have remarkably low mechanical loss at room temperature, sitting at around $\phi_c \lesssim 2.5 \times 10^{-5}$, one order of magnitude smaller than state-of-the-art amorphous coatings used in GWDs [5, 170]. Due to their extremely low levels of loss, AlGaAs coatings can improve the performance of GWDs by reducing the level of coating thermal noise. By lowering both the loss of the coating and the temperature of the test masses, one reduces the values of T and ϕ in equation

2.117, improving the sensitivity of GWDs. In reality, as of the publication of this thesis, it is most likely that next generation detectors will not cool their test masses, though the option has not been totally dismissed. Improved sensitivity of the GWDs yields a higher detection rate of gravitational-wave events, providing more data to the astronomers and physicists that rely on it to test and constrain their theories.

In addition to its room temperature investigation by the gravitational wave community, AlGaAs coatings have also been researched by precision metrology physicists at temperatures as low as 4 K [138, 171]. Low thermal noise, as is demonstrated by AlGaAs coatings, is just as important in the operation of atomic clocks as it is in GWDs. These experiments offer a rare opportunity to measure the thermal noise of AlGaAs coatings directly. Whereas in the Cryo-GeNS the thermal noise is measured indirectly by measuring the loss angle of the modes, these direct measurements are conducted within ultra-stable centimeter scale silicon Fabry-Pérot cavities.

Recent measurements of fixed cavities with AlGaAs mirrors saw excess birefringent noise above the expected Brownian thermal noise. By simultaneously probing the two polarization eigenmodes with two independent lasers, Yu *et al* [138] effectively subtracted the birefringent noise. This was done by polarization averaging; the noise in the two lasers is anticorrelated, so polarization averaging sufficiently suppresses the birefringent noise. The excess noise could not be reduced, but it was determined to have spatial correlation lengths larger than the sizes of the HG_{00} and HG_{01} modes of the locked beam. This is why it is referred to as “global” excess noise in the literature. It is possible that Yu *et al* have made a direct measurement of a new non-local noise source [138]. This is the first time a measurement like this has been made in this frequency regime, and it is possible the expectations of birefringent noise and thermal noise does not match the reality of the system.

Although they are very valuable measurements, these direct measurements were only conducted at specific temperatures, 4 K, 16 K, and 124 K. Additionally, these measurements were impeded by the unknown excess global noise, which masked the thermal noise contribution except within a narrow frequency band at 124 K. Furthermore, these direct measurements are taken at frequencies roughly 1000 times lower than the frequency band that is relevant to GWDs. However, those direct measurements that could be made did agree with the room temperature loss as measured previously, $\phi \lesssim 2.5 \times 10^{-5}$ [5, 138].

In order to better understand the cold temperature behavior, especially at the exact temperatures anticipated to be the operating temperatures of detectors such as KAGRA and ET [8, 9], it is necessary to fill in the gap below 124 K previously measured in centimeter scale Fabry-Pérot cavities but masked by an unknown noise source, or sources. As was discussed in chapter 3 and demonstrated in chapter 4, this is exactly what the Cryo-GeNS was built to do.

5.2 AlGaAs Cold Temperature Mechanical Loss: Results

Once the substrates were returned from the Molecular Beam Epitaxy (MBE) coating process at Thorlabs [5, 166], the coated samples were placed into the Cryo-GeNS for comprehensive ringdown measurements. One of the coated samples is pictured in Figure 36. Data was collected as follows; the first sample was placed and ringdowns were recorded at each temperature twice. It was then removed, and the same process was followed for the second sample. Lastly, the initial sample was placed back into the Cryo-GeNS and data was recorded once more at all temperatures and two additional times at the important temperatures of 12 K and 122 K. The temperatures chosen reflect previous measurements on the substrate, which were chosen to evenly fill out a log scale of temperature from 12 K to 300 K. The uncertainties of the measured losses, such as in Figures 35 and 37, are taken from the standard deviation of the measurements. This uncertainty is carried through when the coating loss was calculated using equation 3.166.

The results of these measurements on the coated samples were already reported for each mode in Figure 15. One can see all the modes overlaid on top of one another in Figure 37. The magnitude of the loss peak around 80 K scales upwards with frequency and is influenced by mode shape, as it was for the substrate. The obvious conclusion is that substrate thermoelastic dissipation (TED) is still a significant source of loss at certain temperatures for certain modes, such as 80 K for mode 7. However, the total mechanical loss of the coated sample is increased due to the presence of the coating, such that the level of impact the substrate thermoelastic loss has on the coated sample loss varies mode by mode.

The importance of understanding the nature of the thermoelastic dissipation from the substrate cannot be understated. In the parameter space of mode frequency and

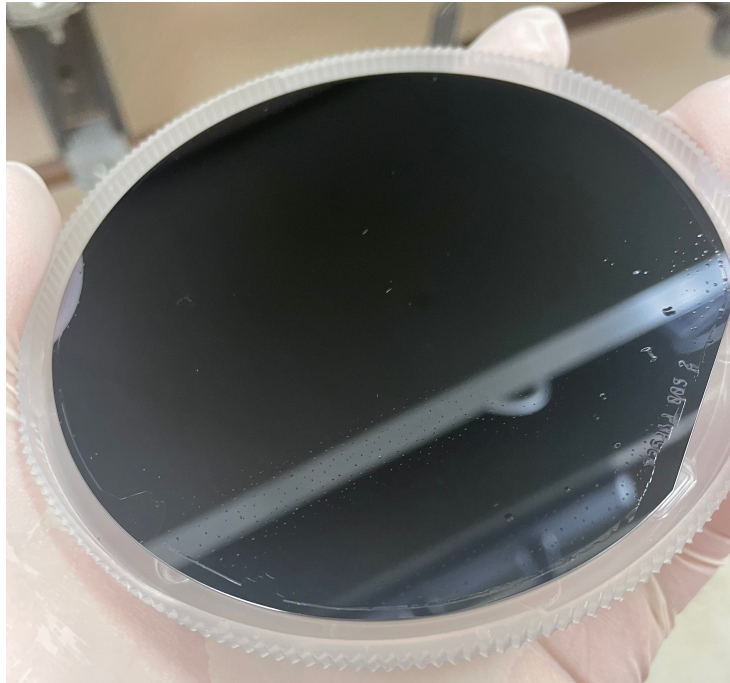


Figure 36 : One of the AlGaAs coated silicon samples. The white bar across the sample is an artifact of the picture, and is a reflection of the wall behind the coating. The slight bumps on the face of the sample are defects from impurities on the silicon substrate surface, and do not have a measurable impact on coating mechanical loss measurements [6].

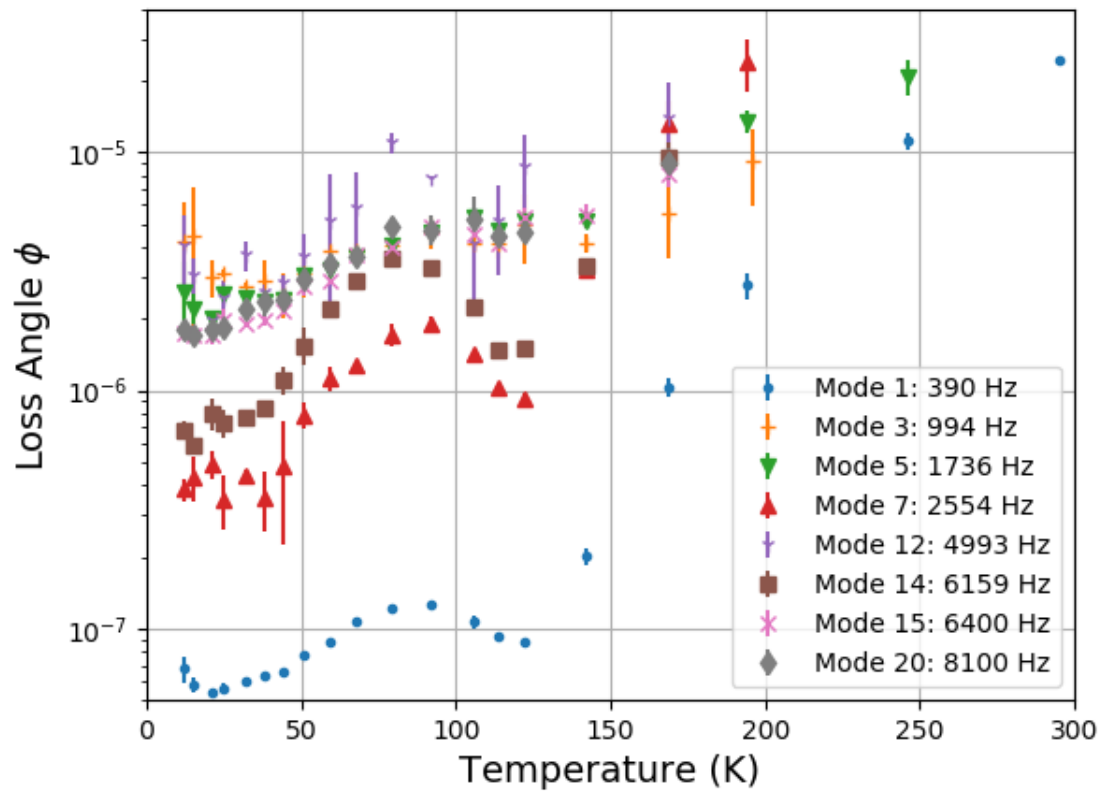


Figure 37 : Loss angle of the coated sample over the temperature range from 12 K to 295 K for all the modes. The presence of a loss peak around 80 K signals influence from substrate thermoelastic dissipation; the magnitude of the peak indicates the how severe this influence is.

temperature where substrate TED dominates the loss of the coated system, such as at 80 K of modes 7 or 14, the additional loss from the coating is insignificant compared to the thermoelastic dissipation due to the substrate. In this scenario, the variance of the individual ringdown loss measurements on the substrate is as large or larger than the loss from the coating itself. This means that when equation 3.166 is used in an attempt to decouple the coating loss from that of the coated system, the resulting coating loss has very high uncertainty. As a result, only measurements where substrate loss is not more than roughly 33% of the measured coated sample loss are considered viable for calculating coating loss. For this reason, Figure 15 is invaluable when understanding at a glance where the coating loss of the AlGaAs multilayer can be trusted.

From Figures 15 and 37, it is apparent that substrate loss becomes problematic at certain temperatures. Due to the large amount of substrate TED, all data above 142 K cannot reliably have the coating loss disentangled from them. However, the substrate thermoelastic loss is insignificant at the coldest temperatures and at 122 K across all modes. At the coldest temperatures, from 12 K to 30 K, the loss of the coated sample is overwhelmingly determined by the coating mechanical loss for all modes. This happens again at 122 K due to a zero crossing point in crystalline silicon's coefficient of thermal expansion that occurs near this temperature, minimizing TE loss. Additionally, at these colder temperatures the TE loss of the coating and coating-substrate interface is found to be insignificant, as can be seen by the low value of the orange curves of Figure 15 at these lower temperatures.

With these important restrictions on coating loss in mind, equation 3.166 was used to calculate the mechanical loss due to solely the AlGaAs coating. Recall from sections 2.1.1 and 2.1.2, specifically equations 2.64 and 2.117, that it is this coating loss that is the most significant component in the test masses of gravitational wave detectors, since the material properties and geometries of the bulk of the test masses lower their losses orders of magnitude below that of the coating. The results of the analysis that extracted coating loss from the coated system loss are presented in Figure 38.

Before discussing the results, it is important to discuss how the dilution factors of equation 3.166 were obtained. As was discussed in section 3.3.1, these dilution factors can be found via finite element analysis (FEA). Two such analyses were carried out

in COMSOL [13] by Steve Penn and Simon Tait [59]. Although both analyses had similar values for the dilution factors, those determined by Tait's FEA were reported here since the simulated modes of his analysis more closely match the measured modes observed in the Cryo-GeNS.

Another important fact about the results to consider is the interplay between substrate and coating loss. Although Figure 37 incorporates loss from both coating and substrate, the loss of the substrate factors more heavily due to the fact that it contains much more energy. This can be seen in equation 3.163, where $D_{s,n}$, representing the percentage of energy in the substrate, will be four to twenty times larger than $D_{c,n}$. Therefore, it is expected that the loss of the coating will be significantly higher than the coated system loss of Figure 37.

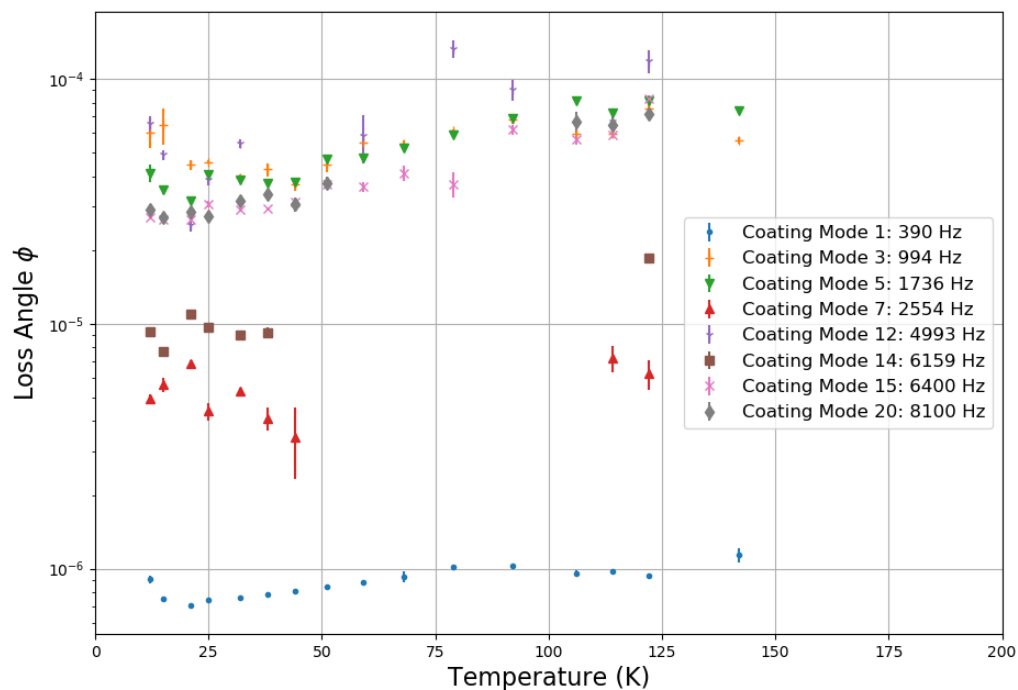


Figure 38 : Mechanical loss of the AlGaAs coating over the temperature range from 12 K to 142 K for all the modes. The points where measured substrate loss approaches the measured loss of the coated system have been removed, as the coating loss cannot be reliably calculated when the coated sample loss is not at least twice as large as the substrate loss. Perhaps the most noticeable trait of this data is the large spread in loss between the modes, with about a factor of 50 difference between the lowest and highest loss modes.

The first thing one tends to notice in Figure 38 is the large gap in data exhibited by modes 7 and 14 above 50 K. Accurate measurements of the coating loss for these modes above 50 K is impossible due to the coated system loss being dominated by the substrate at these temperatures. This can be seen in the plots for these modes in Figure 15.

Additionally, mode 12 shows a relatively large variation in loss over the temperature range as compared to the other modes. The evolution of this mode data over temperature does appear to be following a slight upward trend along with the rest of the modes. However, the relatively large spread in the data for mode 12 is a behavior also shown by the inaccurate data of modes 7 and 14 at temperatures where substrate thermoelastic loss was too large to confidently measure coating loss. However, unlike modes 7 and 14, mode 12 did not have the theoretical TE dissipation or the measured substrate loss pass the 33% of measured coated sample loss threshold for all temperatures around the 80 K substrate loss peak, so its data has been included. The reason for this behavior unique to mode 12 has not been determined.

The inaccuracy in the measured loss above 122 K becomes intolerable for all modes with the exceptions of modes 1, 3, and 5; these exceptions lose all accuracy above 142 K. For that reason, no coating loss data above this temperature has been reported.

To a trained eye, the large difference in loss between the highest loss modes (3, 5, 12, 15, and 20) and the lowest loss mode (1) is striking. Some level of difference between the loss of the modes was expected [6], but never has a difference greater than a factor of 10 been observed. Another crystalline multilayer material, gallium phosphide (GaP) and aluminum gallium phosphide (AlGaP), exhibited only a factor of 3 difference between the modes [172]. However, the loss exhibited by the highest loss modes is still lower than what would be expected of them at room temperature [6], even with the large variation in loss between modes.

Table 3 displays the mode shapes, frequencies, and dilution factors for each of the reported mode numbers. The mode numbers were chosen from a COMSOL model, where the mode number signifies the order of the modes by frequency. The listed dilution factors were those used in equation 3.166.

The mode shapes were determined from a combination of COMSOL modeling and fitting the substrate data to the thermoelastic loss model. As is shown in equation 2.121, the TE loss model is influenced by a geometric factor \mathcal{D} [19], which in turn

Table 3 : A table mapping the mode numbers onto frequencies and mode shapes, where the mode shapes are described as (m, n) . The mode shape number m denotes the amount of radial nodes or circles, while the number n denotes the amount of angular nodes or lines. The associated dilution factors, determined from FEA in COMSOL [13] are also listed. Note that mode number is just an easy way to keep track of which mode is being referenced, instead of stating a shape or frequency. The mode number is chosen by simply numbering all non-degenerate modes by increasing frequency.

Mode Number	Mode Frequency [Hz]	Mode Shape	Dilution Factor (D_c)
1	390	(0, 2)	0.0712
3	994	(0, 3)	0.0620
5	1736	(0, 4)	0.0627
7	2554	(1, 2)	0.0727
12	4993	(0, 7)	0.0622
14	6159	(2, 2)	0.0713
15	6400	(0, 8)	0.0626
20	8100	(1, 7)	0.0618

is determined by the mode shape. When two different mode shapes are very close in frequency, whichever mode shape geometric factor better fits the TE loss model to the substrate data was determined to be the correct shape. This was the case for mode 7, which was either the (1, 2) or (0, 5) mode shapes. (1, 2) was determined to be the correct shape for the observed mode.

Upon comparison of the mode shape to a mode's coating loss behavior, one can notice that the 3 lowest loss modes, 1, 7, and 14, all have just two angular nodal lines. Another way of saying this is that they have a mode shape of $(m, n = 2)$. This behavior has not been observed before by GeNS experiments, for crystalline or amorphous coatings.

It is hypothesized that the mode dependent loss could be caused by the comparative orientations of the mode shapes and the crystal axes. If these low loss modes, relative to the other modes, apply their stresses more along the direction of the lowest loss crystal axis, this could explain the wide range of coating loss values observed. However, this is just considered a hypothesis and cannot be stated with confidence, as there is as yet no explanation why the loss associated with one crystal axis loss would evolve significantly differently than the other two as the temperature of the AlGaAs coating is lowered.

Another hypothesis is that interactions with the the flat of the sample, that was

cut into the substrate to indicate orientation of the crystal axes, is causing this mode-dependent loss. Although the split in mode-dependent losses is not as large for the substrate, it is still substantial. This could be evidence in favor of this explanation. Measuring loss data on samples without a flat would definitively affirm or reject this hypothesis.

5.3 AlGaAs Cold Temperature Mechanical Loss: Thermal Noise in Gravitational Wave Detectors

Recall from section 2.1.2 that the loss angle of an amorphous coating can be decomposed into bulk and shear components. This yields a better prediction of the power spectral density of the coating thermal noise for the coating in a gravitational wave detector [17]. Until now, the loss angles that have been reported have all been attached to individual modes. The bulk and shear decomposition seeks to explain the coating loss of all modes by just two unchanging loss angles, ϕ_c^{Bulk} and ϕ_c^{Shear} . After discussing such a decomposition of the data presented in section 5.2, the possible performance of an AlGaAs coating in a gravitational wave detector, such as those referenced in sections 2.2.2 and 2.2.3 will be considered.

5.3.1 Search for Bulk and Shear Loss Angles

A bulk and shear analysis can be attempted on the AlGaAs coating, even though it is neither amorphous nor isotropic. The three crystal axes of the AlGaAs-GaAs multilayer means that there exists three loss angles, ϕ_{11} , ϕ_{12} , and ϕ_{44} [173]. However, a bulk/shear decomposition has been successfully carried out previously [6]; it is believed to work due to the similar values and energy distributions of the 11 and 12 principle directions.

In order to carry out such a decomposition, one must determine the relative amounts of energy associated with the bulk and shear strains [6, 90]. One can see this in the equation that is fit in order to find the bulk and shear loss angles,

$$\phi_{c,n} = D_{c,n}^{\text{Bulk}} \phi_c^{\text{Bulk}} + D_{c,n}^{\text{Shear}} \phi_c^{\text{Shear}}. \quad (5.172)$$

By finding data at many modes, one effectively has a system of equations, $n = 8$ in

this case for the eight modes measured, that can be fit for values of ϕ_c^{Bulk} and ϕ_c^{Shear} . The new dilution factors, D_c^{Bulk} and D_c^{Shear} , are the ratios of the energies due to bulk and shear strains as compared to the total energy in the coating,

$$\begin{aligned} D_{c,n}^{\text{Bulk}} &= \frac{E_{c,n}^{\text{Bulk}}}{E_{c,n}} \\ D_{c,n}^{\text{Shear}} &= \frac{E_{c,n}^{\text{Shear}}}{E_{c,n}}. \end{aligned} \quad (5.173)$$

As was the case with the dilution factors that enabled disentanglement of coating loss from the coated sample loss, these dilution factors were found through FEA. Such an analysis was carried out by Simon Tait in COMSOL at the request of the author.

This process was conducted at each temperature, however only the data at 21 K is presented in Figure 39. Presenting more data would be redundant, as the behavior of the fit did not change with temperature. Specifically, the fit was found to be non-physical, either in its ascribed values to the shear loss angle or its failure to properly fit the data, or both.

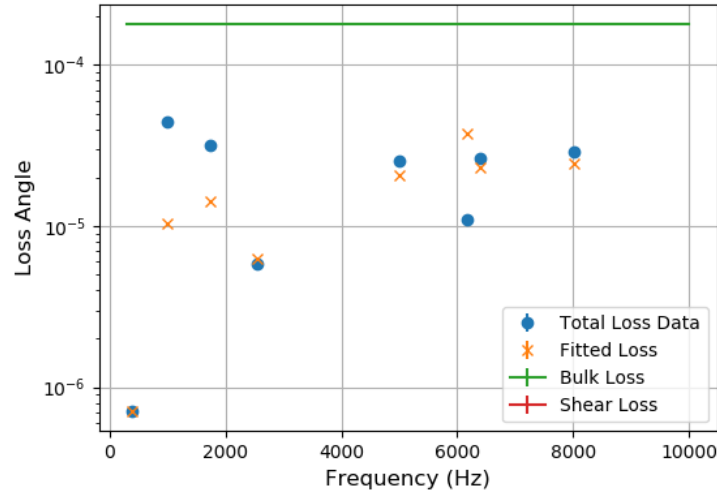


Figure 39 : A fit of bulk and shear loss angles of the AlGaAs coating loss at 21 K. Since it is given a negative value by the fit, shear loss is not pictured. The shape and inaccuracy of the fit is found across all temperatures and if bulk loss is allowed to vary linearly with frequency. The fit becomes intolerably inaccurate when shear loss is restricted to positive values. When the shear fit is forced to be positive, it is found to be a very low value $\phi_c^{\text{Shear}} < 1 \times 10^{-7}$.

Although the levels of bulk and shear loss roughly match what is expected based on

room temperature bulk and shear decomposition of AlGaAs coatings [6], the resulting coating loss as calculated by fitting equation 5.172 does not match the measured coating loss. Additionally, although the shear loss was expected to be vanishingly small, it cannot be negative. When shear loss was forced to be positive, the resulting fit got significantly worse. With such massive residuals between the measured loss and the fit and a negative shear loss, the calculated bulk and shear loss angles cannot be considered a proper reflection of the material loss.

This inability to fit a bulk and shear approximation might be further evidence of a divergence in behavior between the crystal axes when cooled, as discussed at the end of section 5.2. If two of the axes had similar associated losses at room temperature but not at cold temperature, that could explain the inability to properly fit a bulk and shear model to cold temperature data when it previously worked for room temperature data. Therefore, a new model must be used in order to properly characterize the mechanical loss as rigorously as prior experiments.

The crystalline model needs to be a modified version of the bulk/shear model, one that includes three loss angles and dilution factors, one for each of the crystal axes. The process to decompose these three loss angles from the measured mode losses would be carried out similarly to the bulk and shear decomposition. At room temperature, it has proven difficult to disentangle two of the loss angles, ϕ_{11} and ϕ_{12} , for the same reason that the bulk and shear simplification worked. The two dilution factors display very similar behavior as the modes change, which makes finding their associated loss angles challenging [6]. It was hoped that a model at cold temperature would not encounter this problem if the ϕ_{11} and ϕ_{12} loss angles diverged in their behavior.

Such a model was created by Simon Tait and a decomposition by crystal axes was attempted. Although it fit the data relatively well, it unfortunately also yielded non-physical negative loss angles as well as negative energies along certain axes. Such a result cannot be considered accurate whatsoever. Therefore, it is up to future research by the coating optics community to properly decompose the coating loss angles of cold temperature AlGaAs. The models used in this work have proven insufficient.

5.3.2 AlGaAs and Gravitational Wave Detectors

Although it would have been better to have a bulk and shear or crystal axis decomposition of the mode loss angles, one can still make predictions about the coating thermal noise levels of an AlGaAs coating in a gravitational wave detector without them [83, 174]. This can be done by direct comparison to the measured loss angle of the current coatings or a direct calculation of the power spectral density via the following equation [6, 88]

$$S_x(f) = 2k_B T \frac{(1 - \sigma^2)}{\pi^{3/2} w Y f} \phi_{\text{eff}} \quad (5.174)$$

where ϕ_{eff} is defined by

$$\phi_{\text{eff}} = \phi_s + \phi_c \frac{2d - 4d\sigma}{\sqrt{\pi} w (1 - \sigma)}. \quad (5.175)$$

In the above equations, d is the coating thickness and w is the beam width.

Since the AlGaAs coating loss data was masked at warmer temperatures, the most direct application of the results can be made to cryogenic GWDs. Currently, KAGRA (see section 2.2.2) is the only such operating detector. KAGRA uses sapphire mirrors cooled to 20 K in order to reduce thermal noise [8]. Currently, KAGRA's test masses use titania doped tantala as the high index material of the HR coating stack. This material has a mechanical loss of $\phi_c^{\text{KAGRA}} \approx 5 \times 10^{-4}$, and the resulting coating thermal noise could be a limitation on KAGRA's sensitivity [8, 174].

As was reported in section 5.2, the AlGaAs coating mechanical loss measured using the Cryo-GeNS had a large spread in the loss angle between the modes. However, even the highest loss mode outperforms the current KAGRA coating mechanical loss, with the highest loss mode displaying a loss angle of $\sim 5 \times 10^{-5}$ at 20 K. With such a result, it would be reasonable to state that AlGaAs coatings could potentially reduce KAGRA's coating thermal noise by a factor of three in amplitude spectral density ($[\text{m}/\sqrt{\text{Hz}}]$).

The optical properties of an AlGaAs coating have also been explored. The scattering and absorption of AlGaAs coatings are low [175, 176], which increases sensitivity via reduction in optical losses. Unfortunately, AlGaAs is not transparent at 532 nm, meaning the green laser used for lock acquisition would need to be replaced and a new lock acquisition scheme formulated [177]. A possible new lock acquisition approach

has been proposed by the community of AlGaAs researchers [167].

In addition to the current KAGRA detector, there are also possible future GWDs that have been considering cooling their test masses. These include LIGO Voyager, Einstein Telescope (ET), and Cosmic Explorer (CE) [10, 125, 178]. LIGO Voyager and ET have discussed operation at 123 K and 10 K, respectively [125, 178]. If it is assumed that the highest measured loss at 12 K reflects the behavior of an AlGaAs coating at 10 K, the estimated ASD of coating thermal noise at 10 Hz is $\approx 2.5 \times 10^{-21}$ m/ $\sqrt{\text{Hz}}$. The coating thermal noise goal of ET, 3.6×10^{-21} m/ $\sqrt{\text{Hz}}$ at 10 Hz, sits roughly 50% higher than the approximate level of coating thermal noise of the AlGaAs coating under the assumption that the thermal noise is reflected by the highest loss mode measured.

The desired magnitude of coating mechanical loss in a theoretical LIGO Voyager is about five times lower than that presently found in current generation detectors $\phi_c^{\text{Voyager}} \approx 5.5 \times 10^{-5}$ [125]. From Figure 38, one can see that some mode loss angles at 123 K exceed the Voyager loss goals, while other mode loss angles sit below it. Mode 1 is especially notable, with $\phi_c \sim 1 \times 10^{-6}$, having loss levels 50 times lower than the mechanical loss goal of LIGO Voyager. Whether or not an AlGaAs coating would meet the desired loss value cannot be determined without a direct measurement or a model that quantifies the relationship between the mechanical loss of each mode and the coating thermal noise of a test mass.

Cosmic Explorer, which has a coating thermal noise goal about equal to ET at 10 Hz but about five times lower at 20 Hz, see Figure 16, has referenced AlGaAs as a possible coating for its test masses [10]. Like LIGO Voyager, it is impossible to say without further work whether or not a test mass with an AlGaAs coating, at any temperature, will provide such low coating thermal noise levels. However, it can be mentioned that there are measured loss angles, especially mode 1, that would suggest an AlGaAs coated test mass would be satisfactory assuming the loss mimics that of the desired low loss mode.

As has been emphasized for LIGO Voyager and CE, further research is necessary in order to have sufficient confidence in the successful implementation of AlGaAs coatings in cryogenic GWDs, even with the promising results displayed in Figure 38. There are also other problems besides coating thermal noise that must be rectified, such as the ability to realize the necessary coating diameter of the AlGaAs coating.

As of publication of this thesis, the largest manufactured AlGaAs coating diameter has been 10 cm; this is much smaller than the 34 cm to one meter range required by current and future generation GWDs [9, 56, 168]. All of these challenges and open questions as pertaining to an AlGaAs coated test mass are currently being tackled by the wider community of physicists who require greater precision in their laser measurements [167].

Chapter 6

Conclusion

Gravitational wave detectors (GWDs) are entering an era that will be defined by how well the critical noise sources can be mitigated. Quantum squeezing is leading to levels of quantum noise previously considered unattainable. With these improvements to the quantum noise sources, the thermal noise of the high-reflectivity coatings will be the dominant noise source through much of the frequency band considered most important for observation of merging compact binaries. A cryogenic GeNS that can cool a coating sample as low as 12 K was constructed to assess the mechanical loss of AlGaAs coatings across a wide temperature range, with further application of the experiment to any coating that can be bonded to a 3 inch or 4 inch substrate. AlGaAs coatings, at cold temperature and at room temperature, have the possibility to push down coating noise and provide a significant improvement to the sensitivity of the detectors. It has been shown that the loss of AlGaAs coatings at cold temperatures yields remarkable results, both in its magnitude of loss and the behavioral difference between the modes. Although this mode-dependent loss could not be fully explained, even in a worst case scenario where the highest loss modes are most indicative of AlGaAs thermal noise on a GWD, the anticipated coating thermal noise reaches levels that nearly attain or do attain those desired for next generation detectors. Not to mention the significant improvement they would provide current generation detectors. The research and development that needs to be conducted in addition to what was done in this work is summarized below:

- Mode-dependent Loss

- Further research should be conducted on AlGaAs coatings across the temperature range from 10 K to room temperature with an emphasis on tracking mode-dependent losses. At some temperature the loss between the modes must come to resemble that found at room temperature [6], however that was not found in this work due to an inability to measure coating loss above 142 K.
 - There is speculation that the mode orientation to the crystal axes is responsible for this behavior, but that cannot be stated with any certainty without more data taken to address this specific hypothesis.
 - Another hypothesis states that interactions with the flat of the sample causes these mode dependent losses. A follow up measurement on samples without a flat would corroborate or invalidate this possible explanation.
- Crystal Axis Decomposition
 - There was an attempt to decompose the mode loss angles into bulk and shear loss angles as well as crystal axis loss angles. Both analyses yielded non-physical results.
 - Decomposition along the crystal axes has been proposed and attempted by the wider community, but there is as yet no standard model for finding it in the way that currently exists for bulk and shear decomposition.
 - * Perhaps this is because finding the dilution factors associated with the crystal axes through finite element analysis is more difficult than the bulk and shear dilution factors.
 - * Another explanation is the one proposed by Penn *et al* [6] as to why their bulk and shear decomposition worked for room temperature crystalline AlGaAs. If two of the crystal axes' loss angles and dilution factors behave similarly, then modeling the two axes separately becomes extremely difficult.
 - Relationship between Mode Loss Angles and Coating Thermal Noise of a Test Mass

- There is a physical connection between the loss angles of the modes measured in any experiment that tracks ringdowns, such as a GeNS, and the coating thermal noise arising in such a coating on a GWD test mass. It is known that understanding the bulk and shear loss angles of amorphous coatings yields an acceptably accurate quantitative model for coating thermal noise [17], however there is not yet such a model for crystalline coatings, or their three loss angles.
- Perhaps there is a universal relationship that can constrain the possible thermal noise range if one is restricted to only knowing the loss angles of the individual modes rather than the three loss angles of the principle crystal axes. A direct measurement in a centimeter scale cavity that is not limited by global excess noise [138] would go a long way in answering this question.
- Other Materials Measurable in the Cryo-GeNS
 - Although this work has focused on AlGaAs coatings, there are a multitude of coating candidates being considered by the Optics Working Group of the LIGO-VIRGO-KAGRA collaboration. The Cryo-GeNS stands ready to collect information on any substrate-coating material combination that could be of interest.
 - Operation at warmer temperatures for substrates such as fused silica is possible, and perhaps this would be a way to fully cover the temperature range up to room temperature for a single coating. If a coating was deposited on both crystalline silicon and fused silica substrates, the silicon could handle temperatures up to about 140 K, while the fused silica is still acceptably low loss to around 200 K, conservatively.
 - * In reference to AlGaAs, this would serve as an interesting follow-up to this work for two reasons. First, if the mode-dependent loss is due to an interaction between the crystal axes of the silicon and AlGaAs, the greater variance in loss between modes would not appear on a fused silica sample at any temperature. Second, if the large mode-dependent loss does appear when coated on the silica sample, a clue

as to the cause of the loss could be learned by determining at what temperature the room temperature behavior is recovered [6].

Bibliography

- [1] Benjamin P Abbott, Richard Abbott, TD Abbott, MR Abernathy, Fausto Acernese, Kendall Ackley, Carl Adams, Thomas Adams, Paolo Addesso, RX Adhikari, et al. Observation of gravitational waves from a binary black hole merger. *Physical review letters*, 116(6):061102, 2016. i, 13
- [2] Philip S Cowperthwaite, Edo Berger, VA Villar, BD Metzger, M Nicholl, R Chornock, PK Blanchard, W f Fong, R Margutti, M Soares-Santos, et al. The electromagnetic counterpart of the binary neutron star merger ligo/virgo gw170817. ii. uv, optical, and near-infrared light curves and comparison to kilonova models. *The Astrophysical Journal Letters*, 848(2):L17, 2017. i
- [3] Benjamin P Abbott, Rich Abbott, TDea Abbott, Fausto Acernese, Kendall Ackley, Carl Adams, Thomas Adams, Paolo Addesso, RX Adhikari, Vaishali B Adya, et al. Gw170817: observation of gravitational waves from a binary neutron star inspiral. *Physical review letters*, 119(16):161101, 2017. i
- [4] E. Cesarini, M. Lorenzini, E. Campagna, F. Martelli, F. Piergiovanni, F. Vetrano, G. Losurdo, and G. Cagnoli. A “gentle” nodal suspension for measurements of the acoustic attenuation in materials. *Review of Scientific Instruments*, 80(5):053904, 2009. i, xv, 79, 80, 81, 82, 95, 97, 100, 101, 102
- [5] Garrett D Cole, Wei Zhang, Michael J Martin, Jun Ye, and Markus Aspelmeyer. Tenfold reduction of brownian noise in high-reflectivity optical coatings. *Nature Photonics*, 7(8):644–650, 2013. i, 73, 107, 108, 109
- [6] Steven D Penn, Maya M Kinley-Hanlon, Ian AO MacMillan, Paula Heu, David Follman, Christoph Deutsch, Garrett D Cole, and Gregory M Harry. Mechanical ringdown studies of large-area substrate-transferred gaas/algaas crystalline

- coatings. *JOSA B*, 36(4):C15–C21, 2019. i, xvii, 73, 107, 110, 114, 116, 118, 119, 123, 125
- [7] I Martin, H Armandula, C Comtet, MM Fejer, A Gretarsson, G Harry, J Hough, JM M Mackowski, I MacLaren, Christine Michel, et al. Measurements of a low-temperature mechanical dissipation peak in a single layer of ta2o5 doped with tio2. *Classical and Quantum gravity*, 25(5):055005, 2008. i
- [8] T Akutsu, M Ando, K Arai, Y Arai, S Araki, A Araya, N Aritomi, Y Aso, S-W Bae, Y-B Bae, et al. Radiative cooling of the thermally isolated system in kagra gravitational wave telescope. In *Journal of Physics: Conference Series*, volume 1857, page 012002. IOP Publishing, 2021. i, 63, 109, 119
- [9] Michele Maggiore, Chris Van Den Broeck, Nicola Bartolo, Enis Belgacem, Daniele Bertacca, Marie Anne Bizouard, Marica Branchesi, Sebastien Clesse, Stefano Foffa, Juan García-Bellido, Stefan Grimm, Jan Harms, Tanja Hinderer, Sabino Matarrese, Cristiano Palomba, Marco Peloso, Angelo Ricciardone, and Mairi Sakellariadou. Science case for the einstein telescope. *Journal of Cosmology and Astroparticle Physics*, 2020(03):050–050, mar 2020. 22, 71, 106, 109, 121
- [10] Matthew Evans, Rana X Adhikari, Chaitanya Afle, Stefan W Ballmer, Sylvia Biscoveanu, Ssohrab Borhanian, Duncan A Brown, Yanbei Chen, Robert Eisenstein, Alexandra Gruson, et al. A horizon study for cosmic explorer: Science, observatories, and community. *arXiv preprint arXiv:2109.09882*, 2021. i, xv, 22, 70, 71, 120
- [11] Zunping Liu et al. Temperature-dependent elastic constants and young’s modulus of silicon single crystal. *YOUNG*, 4:23, 2021. ix, 45
- [12] Sadao Adachi. Gaas, alas, and al x ga1- x as: Material parameters for use in research and device applications. *Journal of Applied Physics*, 58(3):R1–R29, 1985. ix, 57
- [13] COMSOL. <http://www.comsol.com/>. ix, 84, 97, 113, 115

- [14] An aerial view of ligo hanford. https://www.nsf.gov/news/mmg/mmg_disp.jsp?med_id=65531&from=. x, 10
- [15] An aerial view of ligo livingston. <https://www.ligo.caltech.edu/image/ligo20150731c>. x, 10
- [16] A. Buikema, C. Cahillane, G. L. Mansell, C. D. Blair, et al. Sensitivity and performance of the advanced ligo detectors in the third observing run. *Phys. Rev. D*, 102:062003, Sep 2020. xi, 18, 83
- [17] Ting Hong, Huan Yang, Eric K Gustafson, Rana X Adhikari, and Yanbei Chen. Brownian thermal noise in multilayer coated mirrors. *Physical Review D*, 87(8):082001, 2013. xi, 32, 33, 38, 41, 116, 124
- [18] Rob N Candler, Amy Duwel, Mathew Varghese, Saurabh A Chandorkar, Matthew A Hopcroft, Woo-Tae Park, Bongsang Kim, Gary Yama, Aaron Partridge, Markus Lutz, et al. Impact of geometry on thermoelastic dissipation in micromechanical resonant beams. *Journal of Microelectromechanical Systems*, 15(4):927–934, 2006. xii, 43
- [19] G. Cagnoli, M. Lorenzini, E. Cesarini, F. Piergiovanni, M. Granata, D. Heinert, F. Martelli, R. Nawrodt, A. Amato, Q. Cassar, J. Dickmann, S. Kroker, D. Lumaca, C. Malhaire, and C.B. Rojas Hurtado. Mode-dependent mechanical losses in disc resonators. *Physics Letters A*, 382(33):2165–2173, 2018. Special Issue in memory of Professor V.B. Braginsky. xii, 41, 43, 45, 46, 49, 56, 114
- [20] Ruinan Zhou, Manel Molina-Ruiz, and Frances Hellman. Strategies to reduce the thermoelastic loss of multimaterial coated finite substrates. *arXiv preprint arXiv:2204.09808*, 2022. xiii, xiv, 50, 56, 58, 59
- [21] Raymond Robie. *Characterisation of the mechanical properties of thin-film mirror coating materials for use in future interferometric gravitational wave detectors*. PhD thesis. xiv, 64
- [22] Katherine L Dooley, LIGO Scientific Collaboration, et al. Status of geo 600. In *Journal of Physics: Conference Series*, volume 610, page 012015. IOP Publishing, 2015. xiv, 65, 66

- [23] An aerial view of the advanced virgo detector. <https://www.ligo.caltech.edu/news/ligo20170927>. xiv, 67
- [24] Diagram of the kagra detector. <https://gwcenter.icrr.u-tokyo.ac.jp/wp-content/uploads/2019/11/Nikken-KAGRA.jpg>. xiv, 68
- [25] Peter Fritschel, Francois Schiettekatte, Gabriele Vajente, Lee McCuller, Daniel Brown, Volker Quetschke, Jessica Steinlechner, and Bram Slagmolen. Ligo document t2200384: The lsc instrument science white paper (2022-2023 edition). 2022. xiv, 68, 69
- [26] Lisa Barsotti, Lee McCuller, Matthew Evans, and Peter Fritschel. Ligo document t1800042: The a+ design curve. 2018. xiv, 69
- [27] R. Flaminio. Virgo document 0206a. 2020. xv, 68, 69
- [28] Albert Einstein. Zur Elektrodynamik bewegter Körper. (German) [On the electrodynamics of moving bodies]. *Annalen der Physik*, 322(10):891–921, 1905. 1
- [29] A. Einstein. Ist die trägheit eines körpers von seinem energieinhalt abhängig? *Annalen der Physik*, 18(13):639–643, 1905. 1
- [30] Paul Adrien Maurice Dirac. The quantum theory of the electron. *Proceedings of the Royal Society of London. Series A, Containing Papers of a Mathematical and Physical Character*, 117(778):610–624, 1928. 1
- [31] A. Einstein. Die grundlage der allgemeinen relativitätstheorie. *Annalen der Physik*, 354(7):769–822, 1905. 1
- [32] F. Dyson, A. Eddington, and C. Davidson. Ix. a determination of the deflection of light by the sun’s gravitational field, from observations made at the total eclipse of may 29, 1919. *Philosophical Transactions of the Royal Society of London A: Mathematical, Physical and Engineering Sciences*, 220(571-581):291–333, 1920. 1
- [33] R. F. C. Vessot, M. W. Levine, E. M. Mattison, E. L. Blomberg, T. E. Hoffman, G. U. Nystrom, B. F. Farrel, R. Decher, P. B. Eby, C. R. Baugher, J. W. Watts,

- D. L. Teuber, and F. D. Wills. Test of relativistic gravitation with a space-borne hydrogen maser. *Phys. Rev. Lett.*, 45:2081–2084, Dec 1980. 1
- [34] Joel M. Weisberg, Joseph H. Taylor, and Lee A. Fowler. Gravitational waves from an orbiting pulsar. *Scientific American*, 245(4):74–83, 1981. 1
- [35] K Schwarzschild. Über das gravitationsfeld eines massenpunktes nach der einsteinschen theorie. *Sitzungsberichte der Königlich Preussischen Akademie der Wissenschaften*, (7):189–196, 1916. 2
- [36] J. R. Oppenheimer and G. M. Volkoff. On massive neutron cores. *Physical Review*, 55(4):374–381, 1939. 2
- [37] Bernard Schutz. *A First Course in General Relativity*. Cambridge University Press, 2009. 2, 3
- [38] Dan Bernardi. <https://news.syr.edu/blog/2020/10/15/remembering-joshua-goldberg-professor-emeritus-of-physics-in-the-college-of-art-and-science/> 3
- [39] Peter G. Bergmann. Summary of the chapel hill conference. *Rev. Mod. Phys.*, 29:352–354, Jul 1957. 4
- [40] Felix A. E. Pirani. Republication of: On the physical significance of the riemann tensor. *General Relativity and Gravitation*, 41(5):1215–1232, May 2009. 4
- [41] J. Weber. Evidence for discovery of gravitational radiation. *Phys. Rev. Lett.*, 22:1320–1324, Jun 1969. 4
- [42] Peter Saulson. *Fundamentals of Gravitational Wave Detectors*. World Scientific, 2016. 4, 7, 12, 17, 18, 19, 20, 21, 22, 25, 78
- [43] L. Garwin and J. Weber. Detection of gravity waves challenged. *Physics Today*, 27:9–13, 1974. 4
- [44] R. Weiss. Electronically coupled broadband gravitational antenna. *Quarterly Progress Report, Research Laboratory of Electronics*, 105, 1972. 4

- [45] R. Vogt, F. Raab, R. Drever, K. Thorne, and R. Weiss. Ligo document m890001-v3. 1989. 9
- [46] J. Abadie et al. Sensitivity achieved by the ligo and virgo gravitational wave detectors during ligo’s sixth and virgo’s second and third science runs. *arXiv*. 9
- [47] Thomas Vo. *Adaptive Mode Matching in Advanced LIGO and Beyond*. PhD thesis. 9, 10, 14, 21
- [48] Lee Samuel Finn and David F. Chernoff. Observing binary inspiral in gravitational radiation: One interferometer. *Phys. Rev. D*, 47:2198–2219, Mar 1993. 10, 11
- [49] Duncan Brown. *Searching for Gravitational Radiation from Binary Black Hole MACHOS in the Galactic Halo*. PhD thesis. 10
- [50] D. V. Martynov, E. D. Hall, et al. The sensitivity of the advanced ligo detectors at the beginning of gravitational wave astronomy. *Phys. Rev. D*, 93:112004, Jun 2016. 11
- [51] A. Colombo, O. S. Salafia, F. Gabrielli, G. Ghirlanda, B. Giacomazzo, A. Perego, and M. Colpi. Multi-messenger observations of binary neutron star mergers in the o4 run. *arXiv*, 2022. 11
- [52] L. Schnupp. Talk at european collaboration meeting on interferometric detection of gravitational waves, 1988. 14
- [53] Peter Fritschel, Rolf Bork, Gabriela González, Nergis Mavalvala, Dale Ouimette, Haisheng Rong, Daniel Sigg, and Michael Zucker. Readout and control of a power-recycled interferometric gravitational-wave antenna. *Appl. Opt.*, 40(28):4988–4998, Oct 2001. 15
- [54] S Hild, H Grote, J Degallaix, S Chelkowski, K Danzmann, A Freise, M Hewitson, J Hough, H Lück, M Prijatelj, K A Strain, J R Smith, and B Willke. DC-readout of a signal-recycled gravitational wave detector. *Classical and Quantum Gravity*, 26(5):055012, feb 2009. 16

- [55] AC Green, DD Brown, Miguel Dovale-Álvarez, Chris Collins, Haixing Miao, CM Mow-Lowry, and Andreas Freise. The influence of dual-recycling on parametric instabilities at advanced ligo. *Classical and Quantum Gravity*, 34(20):205004, 2017. 17
- [56] B. P. Abbott et al. Gw150914: The advanced ligo detectors in the era of first discoveries. *Phys. Rev. Lett.*, 116:131103, Mar 2016. 17, 21, 22, 62, 106, 121
- [57] Varun Srivastava. *Detector Improvements and Optimization to Advance Gravitational-Wave Astronomy*. PhD thesis. 19
- [58] SM Aston, MA Barton, AS Bell, N Beveridge, B Bland, AJ Brummitt, G Cagnoli, CA Cantley, L Carbone, AV Cumming, et al. Update on quadruple suspension design for advanced ligo. *Classical and Quantum Gravity*, 29(23):235004, 2012. 19
- [59] Simon Tait. *Studies of mechanical and optical properties of thin film coatings for future gravitational wave detectors*. PhD thesis, 2021. 19, 28, 43, 66, 73, 77, 82, 83, 113
- [60] Fabrice Matichard, B Lantz, Richard Mittleman, Kenneth Mason, J Kissel, B Abbott, S Biscans, J McIver, R Abbott, S Abbott, et al. Seismic isolation of advanced ligo: Review of strategy, instrumentation and performance. *Classical and Quantum Gravity*, 32(18):185003, 2015. 19, 66
- [61] Fabrice Matichard, Brian Lantz, Kenneth Mason, Richard Mittleman, Benjamin Abbott, Samuel Abbott, Eric Allwine, Samuel Barnum, Jeremy Birch, Sebastien Biscans, et al. Advanced ligo two-stage twelve-axis vibration isolation and positioning platform. part 1: Design and production overview. *Precision Engineering*, 40:273–286, 2015.
- [62] Fabrice Matichard, Brian Lantz, Kenneth Mason, Richard Mittleman, Benjamin Abbott, Samuel Abbott, Eric Allwine, Samuel Barnum, Jeremy Birch, Sebastien Biscans, et al. Advanced ligo two-stage twelve-axis vibration isolation and positioning platform. part 2: Experimental investigation and tests results. *Precision engineering*, 40:287–297, 2015. 19

- [63] Jennifer C Driggers, Jan Harms, and Rana X Adhikari. Subtraction of newtonian noise using optimized sensor arrays. *Physical Review D*, 86(10):102001, 2012. 20
- [64] Jan Harms and Stefan Hild. Passive newtonian noise suppression for gravitational-wave observatories based on shaping of the local topography. *Classical and Quantum Gravity*, 31(18):185011, 2014. 20
- [65] Matthew Evans, Peter Fritschel, Rai Weiss, et al. Gas damping monte carlo. *Technical Report LIGO-T0900582*, 2011. 21
- [66] Alessandra Buonanno and Yanbei Chen. Quantum noise in second generation, signal-recycled laser interferometric gravitational-wave detectors. *Phys. Rev. D*, 64:042006, Jul 2001. 22
- [67] Yanbei Chen, Stefan L Danilishin, Farid Ya Khalili, and Helge Müller-Ebhardt. Qnd measurements for future gravitational-wave detectors. *General Relativity and Gravitation*, 43(2):671–694, 2011.
- [68] H. J. Kimble, Yuri Levin, Andrey B. Matsko, Kip S. Thorne, and Sergey P. Vyatchanin. Conversion of conventional gravitational-wave interferometers into quantum nondemolition interferometers by modifying their input and/or output optics. *Phys. Rev. D*, 65:022002, Dec 2001. 22
- [69] Albert Einstein. On the motion of small particles suspended in liquids at rest required by the molecular-kinetic theory of heat. *Annalen der physik*, 17(549-560):208, 1905. 24
- [70] H. Nyquist. Thermal agitation of electric charge in conductors. *Phys. Rev.*, 32:110–113, Jul 1928. 24
- [71] Herbert B Callen and Theodore A Welton. Irreversibility and generalized noise. *Physical Review*, 83(1):34, 1951. 24, 25
- [72] Richard F Greene and Herbert B Callen. On the formalism of thermodynamic fluctuation theory. *Physical Review*, 83(6):1231, 1951.

- [73] Herbert B Callen and Richard F Greene. On a theorem of irreversible thermodynamics. *Physical Review*, 86(5):702, 1952.
- [74] Richard F Greene and Herbert B Callen. On a theorem of irreversible thermodynamics. ii. *Physical Review*, 88(6):1387, 1952. 24, 25
- [75] Peter R. Saulson. Thermal noise in mechanical experiments. *Phys. Rev. D*, 42:2437–2445, Oct 1990. 25
- [76] Yu Levin. Internal thermal noise in the ligo test masses: A direct approach. *Physical Review D*, 57(2):659, 1998. 25, 30
- [77] Aaron Gillespie and Fred Raab. Thermally excited vibrations of the mirrors of laser interferometer gravitational-wave detectors. *Physical Review D*, 52(2):577, 1995. 26
- [78] Robert Hooke. *Lectures de potentia restitutiva, or of spring explaining the power of springing bodies*. Number 6. John Martyn, 2016. 27
- [79] Arthur S Nowick. *Anelastic relaxation in crystalline solids*, volume 1. Elsevier, 2012. 28
- [80] Daniele Mari. The contribution of mechanical spectroscopy to understanding grain boundary sliding. *Materials Research*, 21, 2018. 28
- [81] R. Birney, J. Steinlechner, Z. Tornasi, I. W. Martin, S. Macfoy, D. Vine, A. S. Bell, D. Gibson, J. Hough, S. Rowan, P. Sortais, S. Sproules, S. Tait, and S. Reid. Exploring the fundamental limits of nir absorption in amorphous silicon. 2018. 28
- [82] M Granata, L Balzarini, J Degallaix, V Dolique, R Flaminio, D Forest, D Hoffman, C Michel, R Pedurand, L Pinard, et al. Internal friction and young’s modulus measurements on sio2 and ta2o5 films done with an ultra-high q silicon-wafer suspension. *Archives of Metallurgy and Materials*, 60, 2015. 28, 48, 82, 83, 84, 100, 104, 105
- [83] G Vajente, Ross Birney, A Ananyeva, S Angelova, R Asselin, B Baloukas, R Bassiri, G Billingsley, MM Fejer, D Gibson, et al. Effect of elevated substrate

- temperature deposition on the mechanical losses in tantala thin film coatings. *Classical and Quantum Gravity*, 35(7):075001, 2018. 119
- [84] Giorgio Parisi and Francesco Sciortino. Flying to the bottom. *Nature materials*, 12(2):94–95, 2013. 28, 72
- [85] L D Landau. *Theory of Elasticity*. Pergamon Press, 1986. 29, 39, 51
- [86] Stuart Reid and Iain W Martin. Development of mirror coatings for gravitational wave detectors. *Coatings*, 6(4):61, 2016. 30
- [87] B P Abbott et al. LIGO: the laser interferometer gravitational-wave observatory. *Reports on Progress in Physics*, 72(7):076901, jun 2009. 30
- [88] Gregory M Harry, Andri M Gretarsson, Peter R Saulson, Scott E Kittelberger, Steven D Penn, William J Startin, Sheila Rowan, Martin M Fejer, D R M Crooks, Gianpietro Cagnoli, Jim Hough, and Norio Nakagawa. Thermal noise in interferometric gravitational wave detectors due to dielectric optical coatings. *Classical and Quantum Gravity*, 19(5):897, feb 2002. 31, 40, 63, 76, 77, 97, 119
- [89] William Yam, Slawek Gras, and Matthew Evans. Multimaterial coatings with reduced thermal noise. *Physical Review D*, 91(4), feb 2015. 41
- [90] Gabriele Vajente, Mariana Fazio, Le Yang, Anchal Gupta, Alena Ananyeva, Garilynn Billinsley, and Carmen S Menoni. Method for the experimental measurement of bulk and shear loss angles in amorphous thin films. *Physical Review D*, 101(4):042004, 2020. 41, 73, 116
- [91] Clarence Zener. Internal friction in solids. i. theory of internal friction in reeds. *Physical review*, 52(3):230, 1937. 42, 61
- [92] Janna Rodriguez, Saurabh A Chandorkar, Christopher A Watson, Grant M Glaze, CH Ahn, Eldwin J Ng, Yushi Yang, and Thomas W Kenny. Direct detection of akhiezer damping in a silicon mems resonator. *Scientific reports*, 9(1):1–10, 2019. 43, 45
- [93] Pu Li, Yuming Fang, and Rufu Hu. Thermoelastic damping in rectangular and circular microplate resonators. *Journal of Sound and Vibration*, 331(3):721–733, 2012. 44

- [94] K. G. Lyon, G. L. Salinger, and C. A. Swenson. Linear thermal expansion measurements on silicon from 6 to 340 k. *Journal of Applied Physics*, 48:865–868, 1977. 45, 49
- [95] C Jo Glassbrenner and Glen A Slack. Thermal conductivity of silicon and germanium from 3 k to the melting point. *Physical review*, 134(4A):A1058, 1964. 45
- [96] Koushik Biswas, Charles W Myles, Mahdi Sanati, and George S Nolas. Thermal properties of guest-free si 136 and ge 136 clathrates: A first-principles study. *Journal of Applied Physics*, 104(3):033535, 2008. 45
- [97] Andri M Grefarsson, Gregory M Harry, Steven D Penn, Peter R Saulson, William J Startin, Sheila Rowan, Gianpietro Cagnoli, and Jim Hough. Pendulum mode thermal noise in advanced interferometers: a comparison of fused silica fibers and ribbons in the presence of surface loss. *Physics Letters A*, 270(3-4):108–114, 2000. 48, 76, 105
- [98] Ronny Nawrodt, Anja Zimmer, Torsten Koettig, Christian Schwarz, Daniel Heinert, Matthias Hudl, Ralf Neubert, Matthias Thürk, Sandor Nietzsche, Wolfgang Vodel, et al. High mechanical q-factor measurements on silicon bulk samples. In *Journal of Physics: Conference Series*, volume 122, page 012008. IOP Publishing, 2008. 48
- [99] Ronny Nawrodt, C Schwarz, S Kroker, IW Martin, R Bassiri, F Brückner, L Cunningham, GD Hammond, D Heinert, J Hough, et al. Investigation of mechanical losses of thin silicon flexures at low temperatures. *Classical and Quantum Gravity*, 30(11):115008, 2013. 48, 105
- [100] MM Fejer, S Rowan, G Cagnoli, DRM Crooks, A Grefarsson, GM Harry, J Hough, SD Penn, PH Sneddon, and SP Vyatchanin. Thermoelastic dissipation in inhomogeneous media: loss measurements and displacement noise in coated test masses for interferometric gravitational wave detectors. *Physical Review D*, 70(8):082003, 2004. 52, 56, 61
- [101] Kentaro Somiya and Kazuhiro Yamamoto. Coating thermal noise of a finite-size cylindrical mirror. *Physical Review D*, 79(10):102004, 2009. 56

- [102] SA Loureno, IFL Dias, José Leonil Duarte, Edson Laureto, LC Poças, DO Toginho Filho, and JR Leite. Thermal expansion contribution to the temperature dependence of excitonic transitions in gaas and algaas. *Brazilian journal of physics*, 34:517–525, 2004. 57
- [103] AJ Borak, CC Phillips, and C Sirtori. Temperature transients and thermal properties of gaas/algaas quantum-cascade lasers. *Applied physics letters*, 82(23):4020–4022, 2003. 56, 57
- [104] J Piprek, T Troger, B Schroter, JAKJ Kolodzey, and CS Ih. Thermal conductivity reduction in gaas-alas distributed bragg reflectors. *IEEE Photonics Technology Letters*, 10(1):81–83, 1998. 56
- [105] M. Evans, S. Ballmer, M. Fejer, P. Fritschel, G. Harry, and G. Ogin. Thermo-optic noise in coated mirrors for high-precision optical measurements. *Phys. Rev. D*, 78:102003, Nov 2008. 57, 61
- [106] VB Braginsky, ML Gorodetsky, and SP Vyatchanin. Thermo-refractive noise in gravitational wave antennae. *Physics Letters A*, 271(5-6):303–307, 2000. 60
- [107] Junaid Aasi, BP Abbott, Richard Abbott, Thomas Abbott, MR Abernathy, Kendall Ackley, Carl Adams, Thomas Adams, Paolo Addesso, RX Adhikari, et al. Advanced ligo. *Classical and quantum gravity*, 32(7):074001, 2015. 62
- [108] C. Comtet, D. Forest, P. Ganau, G.M. Harry, J.-M. Mackowski, Christine Michel, J.-L. Montorio, N. Morgado, V. Pierro, L. Pinard, I. Pinto, and A. Remillieux. Reduction of tantala mechanical losses in Ta₂O₅/SiO₂ coatings for the next generation of VIRGO and LIGO interferometric gravitational waves detectors. In *42th Rencontres de Moriond - Gravitational Waves and Experimental Gravity*, La Thuile, Italy, March 2007. 62
- [109] Gregory M Harry, Matthew R Abernathy, Andres E Becerra-Toledo, Helena Armandula, Eric Black, Kate Dooley, Matt Eichenfield, Chinyere Nwabugwu, Akira Villar, D R M Crooks, Gianpietro Cagnoli, Jim Hough, Colin R How, Ian MacLaren, Peter Murray, Stuart Reid, Sheila Rowan, Peter H Sneddon, Martin M Fejer, Roger Route, Steven D Penn, Patrick Ganau, Jean-Marie

- Mackowski, Christophe Michel, Laurent Pinard, and Alban Remillieux. Titania-doped tantala/silica coatings for gravitational-wave detection. *Classical and Quantum Gravity*, 24(2):405, dec 2006. 73
- [110] R Flaminio, J Franc, C Michel, N Morgado, L Pinard, and B Sassolas. A study of coating mechanical and optical losses in view of reducing mirror thermal noise in gravitational wave detectors. *Classical and Quantum Gravity*, 27(8):084030, apr 2010. 62
- [111] Massimo Granata. Coating research and development at lma. 2017 Gravitational-Wave Advanced Detector Workshop, 2017. 63
- [112] Wenxuan Jia, Hiroaki Yamamoto, Kevin Kuns, Anamaria Effler, Matthew Evans, Peter Fritschel, R Abbott, C Adams, RX Adhikari, A Ananyeva, et al. Point absorber limits to future gravitational-wave detectors. *Physical Review Letters*, 127(24):241102, 2021. 63
- [113] R Abbott, TD Abbott, S Abraham, F Acernese, K Ackley, A Adams, C Adams, RX Adhikari, VB Adya, Christoph Affeldt, et al. Gwtc-2: compact binary coalescences observed by ligo and virgo during the first half of the third observing run. *Physical Review X*, 11(2):021053, 2021. 65
- [114] R Abbott, TD Abbott, F Acernese, K Ackley, C Adams, N Adhikari, RX Adhikari, VB Adya, C Affeldt, D Agarwal, et al. Gwtc-3: compact binary coalescences observed by ligo and virgo during the second part of the third observing run. *arXiv preprint arXiv:2111.03606*, 2021. 65
- [115] A gravitational wave observatory operating beyond the quantum shot-noise limit. *Nature Physics*, 7(12):962–965, 2011. 66
- [116] Junaid Aasi, Joan Abadie, BP Abbott, Richard Abbott, TD Abbott, MR Abernathy, Carl Adams, Thomas Adams, Paolo Addesso, RX Adhikari, et al. Enhanced sensitivity of the ligo gravitational wave detector by using squeezed states of light. *Nature Photonics*, 7(8):613–619, 2013. 66
- [117] Hartmut Grote, LIGO Scientific Collaboration, et al. The geo 600 status. *Classical and Quantum Gravity*, 27(8):084003, 2010. 66

- [118] G Losurdo, G Calamai, E Cuoco, L Fabbroni, G Guidi, M Mazzoni, R Stanga, F Vetrano, L Holloway, D Passuello, et al. Inertial control of the mirror suspensions of the virgo interferometer for gravitational wave detection. *Review of Scientific Instruments*, 72(9):3653–3661, 2001. 66
- [119] F Acernese, T Adams, K Agatsuma, L Aiello, A Allocca, A Amato, S Antier, N Arnaud, S Ascenzi, P Astone, et al. Advanced virgo status. In *Journal of Physics: Conference Series*, volume 1342, page 012010. IOP Publishing, 2020. 66
- [120] Benjamin P Abbott. Multi-messenger observations of a binary neutron star merger. 2017. 66
- [121] Fulvio Ricci. Gravitational waves detectors. In *Journal of Physics: Conference Series*, volume 1468, page 012224. IOP Publishing, 2020. 66
- [122] Benjamin P Abbott, R Abbott, TD Abbott, S Abraham, F Acernese, K Ackley, C Adams, VB Adya, C Affeldt, M Agathos, et al. Prospects for observing and localizing gravitational-wave transients with advanced ligo, advanced virgo and kagra. *Living reviews in relativity*, 23(1):1–69, 2020. 67
- [123] Homare Abe, Tomotada Akutsu, Masaki Ando, Akito Araya, Naoki Aritomi, Hideki Asada, Yoichi Aso, Sangwook Bae, Rishabh Bajpai, Kipp Cannon, et al. The current status and future prospects of kagra, the large-scale cryogenic gravitational wave telescope built in the kamioka underground. *Galaxies*, 10(3):63, 2022. 67
- [124] John Miller, Lisa Barsotti, Salvatore Vitale, Peter Fritschel, Matthew Evans, and Daniel Sigg. Prospects for doubling the range of advanced ligo. *Physical Review D*, 91(6):062005, 2015. 67
- [125] Rana X Adhikari, Koji Arai, AF Brooks, C Wipf, O Aguiar, Paul Altin, B Barr, L Barsotti, R Bassiri, A Bell, et al. A cryogenic silicon interferometer for gravitational-wave detection. *Classical and Quantum Gravity*, 37(16):165003, 2020. 70, 73, 120

- [126] Giorgio Parisi and Francesco Zamponi. The ideal glass transition of hard spheres. *The Journal of chemical physics*, 123(14):144501, 2005. 72, 73
- [127] William A Phillips. Tunneling states in amorphous solids. *Journal of low temperature physics*, 7:351–360, 1972. 72
- [128] P W Anderson, Bertrand I Halperin, and C M Varma. Anomalous low-temperature thermal properties of glasses and spin glasses. *Philosophical Magazine*, 25(1):1–9, 1972.
- [129] Josef Jäckle. On the ultrasonic attenuation in glasses at low temperatures. *Zeitschrift für Physik A Hadrons and nuclei*, 257(3):212–223, 1972. 72
- [130] William A Phillips. Two-level states in glasses. *Reports on Progress in Physics*, 50(12):1657, 1987. 72
- [131] KS Gilroy and WA Phillips. An asymmetric double-well potential model for structural relaxation processes in amorphous materials. *Philosophical Magazine B*, 43(5):735–746, 1981. 72
- [132] Xiao Liu, Daniel R Queen, Thomas H Metcalf, Julie E Karel, and Frances Hellman. Hydrogen-free amorphous silicon with no tunneling states. *Physical review letters*, 113(2):025503, 2014. 72, 73
- [133] DR Queen, X Liu, J Karel, TH Metcalf, and F Hellman. Excess specific heat in evaporated amorphous silicon. *Physical review letters*, 110(13):135901, 2013.
- [134] Xiao Liu, BE White Jr, RO Pohl, E Iwanizcko, KM Jones, AH Mahan, BN Nelson, RS Crandall, and S Veprek. Amorphous solid without low energy excitations. *Physical review letters*, 78(23):4418, 1997. 72
- [135] Matt Abernathy, F Acernese, P Ajith, B Allen, P Amaro Seoane, N Andersson, S Aoudia, P Astone, B Krishnan, L Barack, et al. Einstein gravitational wave telescope conceptual design study. 2011. 73
- [136] Tara Chalermongsak, Evan D Hall, Garrett D Cole, David Follman, Frank Seifert, Koji Arai, Eric K Gustafson, Joshua R Smith, Markus Aspelmeyer,

- and Rana X Adhikari. Coherent cancellation of photothermal noise in gaas/al0.92ga0.08as bragg mirrors. *Metrologia*, 53(2):860, 2016. 73, 107
- [137] Manuel Marchiò, Raffaele Flaminio, Laurent Pinard, Danièle Forest, Christoph Deutsch, Paula Heu, David Follman, and Garrett D Cole. Optical performance of large-area crystalline coatings. *Optics express*, 26(5):6114–6125, 2018. 107
- [138] Jialiang Yu, Dhruv Kedar, Sebastian Häfner, Thomas Legero, Fritz Riehle, Sofia Herbers, Daniele Nicolodi, Chun Yu Ma, John M Robinson, Eric Oelker, et al. Excess noise in highly reflective crystalline mirror coatings. *arXiv preprint arXiv:2210.15671*, 2022. 108, 124
- [139] Satoshi Tanioka, Daniel Vander-Hyde, Garrett D Cole, Steven D Penn, and Stefan W Ballmer. Study on electro-optic noise in crystalline coatings toward future gravitational wave detectors. *Physical Review D*, 107(2):022003, 2023. 73, 107
- [140] Mark A Beilby, Peter R Saulson, and Alex Abramovici. Photoelastic measurement of anelasticity and its implications for gravitational wave interferometers. *Review of scientific instruments*, 69(6):2539–2545, 1998. 76
- [141] William J Startin, Mark A Beilby, and Peter R Saulson. Mechanical quality factors of fused silica resonators. *Review of Scientific Instruments*, 69(10):3681–3689, 1998. 76, 100, 101, 102
- [142] Kenji Numata, Shigemi Otsuka, Masaki Ando, and Kimio Tsubono. Intrinsic losses in various kinds of fused silica. *Classical and Quantum Gravity*, 19(7):1697, 2002. 76
- [143] DRM Crooks, P Sneddon, G Cagnoli, J Hough, S Rowan, MM Fejer, E Gustafson, R Route, N Nakagawa, D Coyne, et al. Excess mechanical loss associated with dielectric mirror coatings on test masses in interferometric gravitational wave detectors. *Classical and Quantum Gravity*, 19(5):883, 2002. 76, 77
- [144] Steven D Penn, Peter H Sneddon, Helena Armandula, Joseph C Betzwieser, Gianpietro Cagnoli, Jordan Camp, DRM Crooks, Martin M Fejer, Andri M

- Gretarsson, Gregory M Harry, et al. Mechanical loss in tantala/silica dielectric mirror coatings. *Classical and Quantum Gravity*, 20(13):2917, 2003. 84
- [145] Steven D Penn, Alexander Ageev, Dan Busby, Gregory M Harry, Andri M Gretarsson, Kenji Numata, and Phil Willems. Frequency and surface dependence of the mechanical loss in fused silica. *Physics Letters A*, 352(1-2):3–6, 2006. 76, 77, 97, 100, 101, 102
- [146] Massimo Granata, Emeline Saracco, Nazario Morgado, Alix Cajgfinger, Gianpietro Cagnoli, Jérôme Degallaix, Vincent Dolique, Daniele Forest, Janyce Franc, Christophe Michel, et al. Mechanical loss in state-of-the-art amorphous optical coatings. *Physical Review D*, 93(1):012007, 2016. 77
- [147] S Reid, G Cagnoli, DRM Crooks, J Hough, PI Murray, S Rowan, MM Fejer, R Route, and S Zappe. Mechanical dissipation in silicon flexures. *Physics letters A*, 351(4-5):205–211, 2006. 79
- [148] BE White Jr and RO Pohl. Internal friction of subnanometer a-si o 2 films. *Physical review letters*, 75(24):4437, 1995. 79
- [149] G Vajente, A Ananyeva, G Billingsley, E Gustafson, A Heptonstall, E Sanchez, and C Torrie. A high throughput instrument to measure mechanical losses in thin film coatings. *Review of Scientific Instruments*, 88(7):073901, 2017. 80, 82, 83, 90, 95
- [150] S. Penn. Ligo document g060140-x0. 2006. 82
- [151] Anna Roche, Aaron Markowitz, and Rana Adhikari. Measuring mechanical loss in cryogenic gentle nodal suspension resonator. *LIGO Document T1900391-v1*, 2019. 82, 83
- [152] Massimo Granata, Alex Amato, Laurent Balzarini, Maurizio Canepa, Jérôme Degallaix, Danièle Forest, Vincent Dolique, Lorenzo Mereni, Christophe Michel, Laurent Pinard, et al. Amorphous optical coatings of present gravitational-wave interferometers. *Classical and Quantum Gravity*, 37(9):095004, 2020. 83

- [153] Garfield Walter McMahon. Experimental study of the vibrations of solid, isotropic, elastic cylinders. *The Journal of the Acoustical Society of America*, 36(1):85–92, 1964. 83
- [154] Tianjun Li, Felipe A Aguilar Sandoval, Mickael Geitner, Ludovic Bellon, Gianpietro Cagnoli, Jérôme Degallaix, Vincent Dolique, Raffaele Flaminio, Danièle Forest, Massimo Granata, et al. Measurements of mechanical thermal noise and energy dissipation in optical dielectric coatings. *Physical Review D*, 89(9):092004, 2014. 84
- [155] National Instruments. <https://www.ni.com/en-us/shop/labview.html>. 89
- [156] Elenna Capote et al. Elastic loss in amorphous zirconia-titania coatings. *LIGO Document G2200396*, 2022. 92, 93
- [157] Cryomech. <https://www.cryomech.com>. 93, 94, 97
- [158] Empire Magnetics Inc. <https://www.empiremagnetics.com/>. 93
- [159] Edmund Optics. <https://www.edmundoptics.com/p/25mm-dia-x-30mm-fl-uncoated-si-plano-convex-lens/23955/#>. 95
- [160] Elenna Capote et al. Elastic loss in amorphous zirconia-titania coatings. *LIGO Document G2200396*, 2022. 97
- [161] ANSYS. <https://www.ansys.com/>. 97
- [162] Stanford Research Systems. <https://www.thinksrs.com/products/ctc100.html>. 97
- [163] Joshua R Smith, Gregory M Harry, Joe C Betzwieser, Andri M Gretarsson, David A Guild, Scott E Kittelberger, Michael J Mortonson, Steven D Penn, and Peter R Saulson. Mechanical loss associated with silicate bonding of fused silica. *Classical and Quantum Gravity*, 20(23):5039, 2003. 100, 101, 102
- [164] Anja Schroeter, Ronny Nawrodt, Roman Schnabel, Stuart Reid, Iain Martin, Sheila Rowan, Christian Schwarz, Torsten Koettig, Ralf Neubert, Matthias Thürk, et al. On the mechanical quality factors of cryogenic test masses from

- fused silica and crystalline quartz. *arXiv preprint arXiv:0709.4359*, 2007. 100, 101, 102, 103
- [165] Ultrasil LLC. http://www.ultrasil.com/get_quote_std_products_new.aspx#. 103
- [166] Garrett Cole. https://www.thorlabs.com/newgrouppage9.cfm?objectgroup_id=13322#ad-image-0. 106, 109
- [167] GD Cole, S Ballmer, G Billingsley, SB Cataño-Lopez, M Fejer, P Fritschel, AM Gretarsson, GM Harry, D Kedar, T Legero, et al. Substrate-transferred gaas/algaas crystalline coatings for gravitational-wave detectors: A review of the state of the art. *arXiv preprint arXiv:2301.02687*, 2023. 106, 120, 121
- [168] David Reitze, Rana X Adhikari, Stefan Ballmer, Barry Barish, Lisa Barsotti, GariLynn Billingsley, Duncan A Brown, Yanbei Chen, Dennis Coyne, Robert Eisenstein, et al. Cosmic explorer: the us contribution to gravitational-wave astronomy beyond ligo. *arXiv preprint arXiv:1907.04833*, 2019. 106, 121
- [169] Martin A Afromowitz. Refractive index of gal-xalxas. *Solid State Communications*, 15(1):59–63, 1974. 107
- [170] Slawomir Gras and Matthew Evans. Direct measurement of coating thermal noise in optical resonators. *Physical Review D*, 98(12):122001, 2018. 107
- [171] Dhruv Kedar, Jialiang Yu, Eric Oelker, Alexander Staron, William R Milner, John M Robinson, Thomas Legero, Fritz Riehle, Uwe Sterr, and Jun Ye. Frequency stability of cryogenic silicon cavities with semiconductor crystalline coatings. *arXiv preprint arXiv:2210.14881*, 2022. 108
- [172] AV Cumming, K Craig, IW Martin, R Bassiri, L Cunningham, MM Fejer, JS Harris, K Haughian, D Heinert, B Lantz, et al. Measurement of the mechanical loss of prototype gap/algap crystalline coatings for future gravitational wave detectors. *Classical and Quantum Gravity*, 32(3):035002, 2015. 114
- [173] Ian MacMillan. Brownian thermal noise in algaas and its implications for ligo’s sensitivity. *LIGO Document P1800359*, 2019. 116

- [174] Eiichi Hirose, Kieran Craig, Hideki Ishitsuka, Iain W Martin, Norikatsu Mio, Shigenori Moriwaki, Peter G Murray, Masatake Ohashi, Sheila Rowan, Yusuke Sakakibara, et al. Mechanical loss of a multilayer tantala/silica coating on a sapphire disk at cryogenic temperatures: Toward the kagra gravitational wave detector. *Physical Review D*, 90(10):102004, 2014. 119
- [175] Garrett D Cole, Wei Zhang, Bryce J Bjork, David Follman, Paula Heu, Christoph Deutsch, Lindsay Sonderhouse, John Robinson, Chris Franz, Alexei Alexandrovski, et al. High-performance near-and mid-infrared crystalline coatings. *Optica*, 3(6):647–656, 2016. 119
- [176] Georg Winkler, LW Perner, G-W Truong, Gang Zhao, Dominic Bachmann, Aline Sophie Mayer, Jakob Fellingner, David Follman, Paula Heu, Christoph Deutsch, et al. Mid-infrared interference coatings with excess optical loss below 10 ppm. *Optica*, 8(5):686–696, 2021. 119
- [177] T Akutsu et al. An arm length stabilization system for kagra and future gravitational-wave detectors. *Classical and Quantum Gravity*, 37(3):035004, jan 2020. 119
- [178] Kieran Craig, Jessica Steinlechner, Peter G Murray, Angus S Bell, Ross Birney, Karen Haughian, Jim Hough, Ian MacLaren, Steve Penn, Stuart Reid, et al. Mirror coating solution for the cryogenic einstein telescope. *Physical Review Letters*, 122(23):231102, 2019. 120

Nicholas Didio

235 E 95th St, Apt 17A | New York, NY 10128 | 201-403-1497 | nadidio@syr.edu

SUMMARY

- Experimental physicist with a focus on materials science at a wide-range of temperature
- 3+ years of experience in measuring mechanical and thermoelastic loss in many materials for the LVK (LIGO-VIRGO-KAGRA) Scientific Collaboration
- Designed and built an experiment to measure loss at any temperature between 10 K and 300 K
- Worked with collaborators worldwide to improve optics of gravitational wave detectors

EDUCATION

Syracuse University (Syracuse, NY): *PhD Physics* **May 2023**

- Experimental physics research quantifying mechanical and thermoelastic loss
- Member of LVK Scientific Collaboration
- Vice President, Physics Graduate Student Organization

Syracuse University (Syracuse, NY): *MS Physics* **Dec 2019**

Colgate University (Hamilton, NY): *BA Astronomy-Physics* **May 2016**

RESEARCH EXPERIENCE

Syracuse University **2017 – Present**

- Built a multipurpose lab after inheriting an empty lab space
- Created a vacuum system that can achieve pressure of 10^{-7} torr
- Assembled cryogenic system capable of cooling vacuum chamber to 10 K
- Data Acquisition system assembled and operated via LabVIEW
- Used cryogenic chamber and optical laser system to observe ring-down of normal modes, yielding mechanical and thermoelastic loss properties of novel optical coating materials
- Materials tested include fused silica, silicon, amorphous silicon, amorphous silica, gallium arsenide, and aluminum gallium arsenide

Colgate University Foggy Bottom Observatory **2015 – 2016**

- Operated a near IR telescope to observe varying brightness in quasars and blazars

WORK EXPERIENCE

Syracuse University (Syracuse, NY)

2018 – Present

Graduate Research Fellow

- Assisted various experiments with electrical or optics work
- Built novel experiment to publish thesis of my own on mechanical and thermoelastic loss of possible coating materials for LVK interferometers

Syracuse University (Syracuse, NY)

2017 – 2019

Lead Instructor/Teaching Assistant

- Created and led unique astronomy classes for non-majors over the summers
- Assisted in teaching astronomy and physics classes and labs during the semester

The Gravity Vault (Upper Saddle River, NJ)

2016 – 2017

Rock Climbing Staff

- Worked in a collaborative environment with other staff to introduce novice climbers to rock climbing in a safe and fun environment, with emphasis on team-building

Black Bear Asset Management (New York, NY)

2016

Private Equity Real Estate Analyst

- Crafted operating memoranda highlighting all pertinent information, quantitative and qualitative, of prospective real estate investments for the firm

Colgate University (Hamilton, NY)

2015

Undergraduate Summer Researcher

TECHNICAL SKILLS

Research: Project Design, Data Collection, Analysis, and Visualization, Collaborative Projects, Science Communication

Experimental: Vacuum Hardware, Cold Temperature Hardware, Data Acquisition Systems, Optics, Electronics

Languages: C++, Python

Software: LabVIEW, MATLAB, Mathematica, Microsoft Office Suite, Gnumeric, AbiWord